

ISSN 0377-9416



www.pmai.in

TRANSACTIONS OF POWDER METALLURGY ASSOCIATION OF INDIA

Vol. 41 No.1, June 2015

Chief Editor - P. Ramakrishnan

ISSN 0377-9416



www.pmai.in

**TRANSACTIONS OF
POWDER METALLURGY
ASSOCIATION OF INDIA**

Vol. 41 No.1, June 2015

Chief Editor - P. Ramakrishnan



Powder Metallurgy Association of India

Office Bearers

President

Shri N. Gopinath

Vice President

Shri Deepak Grover

Shri Narendra Dhokey

Shri Rajendra Sethiya

General Secretary

Dr. Deep Prakash

Hon. Treasurer

Dr. Murli Gopal Krishnamoorty

Joint Secretary

Shri Aniket Gore

Shri Rajat Varshney



Chief Editor

Prof. Ramakrishnan P.

Editorial Advisory Board

Dr. Ashok S.

Mr. Chandrachud N.L.

Dr. Rama Mohan T. R.

Editorial Board

Dr. Appa Rao G.

Dr. Bhargava Parag

Dr. Dabhade Vikram

Dr. Deep Prakash

Dr. Dhokey N.B.

Dr. Kumar Y.V.S.

Dr. Malobika Karanjai

Dr. Murli Gopal K.

Dr. Panigrahi B.B.

Dr. Sastry I.S.R.

Dr. Tarasankar Mahata

Published by :

Powder Metallurgy Association of India (PMAI)

1002, B-Wing, Kingston, High Street, Hiranandani Complex, Powai, Mumbai - 400076.

Tel. : +9122 25704588

E-mail : info@pmai.in

Neither the Powder Metallurgy Association of India nor the editor assumes responsibility of opinions expressed by the authors of the papers published in this transaction.

Editorial



The International Conference & Exhibition, PM-15, held at I.I.T., Bombay during Jan.2015, inaugurated by Hon. Manohar Parikar, Defense Minister of India, an I.I.T(B) alumni, Metallurgy class '78 was a great success. For the first time PMAI announced the Grand Prize for the best student paper, an all expenses paid trip to attend the International Conference of Powder Metallurgy & Particulate Materials, during May 17-20, 2015, San Diego, U.S.A. The award was won

by Mr. Shashanka and his unforgettable journey to Powdermet 2015, U.S.A., was reported in PMAI Newsletter, Aug. 2015. Selected papers from the PMAI, PM-15, are included in this volume of the Transaction. First two articles are dealing with the synthesis of nano crystalline Fe-20Cr-3Al alloys and Cr₂AlC powders by high energy ball milling and their characterization. The next paper is on the physicochemical characterization and the effective fixation of Beryllium in the red mud produced during the extraction of Beryllium. This is followed by an article on the study of powder forged gear material at a density of 98 percent.

The Grand prize winning paper deals with the investigation on the effect of Y₂O₃ addition on the non lubricated sliding wear behavior of duplex stainless steel processed by compaction and sintering. Machinability of sinter hardened materials have been improved with the addition of MnS in the initial powder thereby increasing the tool life is dealt with in the following article. Dye sensitized solar cell is a cheaper alternate for the conventional semi conductor solar cells. In this paper CsSnBr_xI_{3-x} is synthesized and characterized for its application as solid state hole transport material for DSSc. This is followed by a paper on the salt assisted synthesis for producing de agglomerated nano Zirconia particles. The next paper is on the failure mode co relation between grain size distribution, nature of grain boundary and phases present in the microstructure on high voltage Zinc oxide varistors with the distribution current, temperature and thermal stresses. The development of Invar-silver composites for microwave integrated circuit for carrier plate for satellites is another award winning paper. The next article deals with an insight into the Laser Additive Manufacturing for different industries, highlighting important techniques, materials along with the relative advantages and limitations and the current research trends. The final paper discuss the optimization of process parameters for chemical synthesis of nano sized Tin oxide particles for energy storage applications like Lithium-ion batteries.

P. Ramakrishnan.

TRANSACTIONS OF
POWDER METALLURGY ASSOCIATION OF INDIA

Vol. 41 No.1, June 2015

CONTENTS

1. Synthesis of Nanocrystalline Fe-20Cr-3Al Alloys by Ball Milling	1-2
Rajiv Kumar, Joydip Joardar, R. K. Singh Raman, V. S. Raja, S. V. Joshi, S. Parida	
2. Mechanically Activated Synthesis of Nanocrystalline Cr₂AlC Powders	3-8
Y. Rajkumar and Bharat B. Panigrahi	
3. Physico-chemical characterization of red mud produced during extraction of beryllium	9-12
B.M. Tripathi, Deep Prakash and P.K. Sinha	
4. Study of powder forged properties of gear material	13-16
J.D.Khatri, V.T.Thavale, N.B.Dhokey	
5. Effect of Y₂O₃ addition on non-lubricated sliding wear behaviour of duplex stainless steel	17-25
Shashanka R, D. Chaira	
6. Machinability of Sinter-hardening PM materials with experimental machining enhancers	26-32
Maryam Moravej, Francois Chagnon ¹ , Philippe Francois	
7. Synthesis and Application of CsSnBr₁₋₃X as a Solid State Hole Transport Material in Dye Sensitized Solar Cells	33-35
Lekha Peedikakkandy, Parag Bhargava	
8. Salt assisted synthesis of nano zirconia	36-42
Divya P, P Bhargava	
9. Correlation of failure modes of zinc oxide varistors with their microstructures	43-48
S.Saravanan, J. Nemade	
10. Development of Invar-Silver Composite for MIC Carrier Plate of Satellites	49-53
D.K.Mishra, T.T. Saravanan, G.P. Khanra, S.C. Sharma & Koshy M. George	
11. Research Trends in Laser Assisted Additive Manufacturing	54-76
Abhishek Singh Chauhan, Ujjwal Dubey, Arvind Kumar	
12. Nano Sized Metal Oxide Powders for Energy Storage Applications	77-86
Raghu C Reddy, R Narasimha Rao and N R Munirathnam	

SYNTHESIS OF NANOCRYSTALLINE Fe-20Cr-3Al ALLOYS BY BALL MILLING

Rajiv Kumar^{1,2,3}, Joydip Joardar⁵, R. K. Singh Raman^{3,4}, V. S. Raja², S. V. Joshi⁵, S. Parida²

¹ IITB Monash Research Academy, IIT Bombay, Powai, Mumbai.

² Department of Metallurgical Engineering and Materials Science, IIT Bombay, Mumbai.

³ Department of Mechanical and Aerospace Engineering, Monash University, Australia.

⁴ Department of Chemical Engineering, Monash University, Australia.

⁵ International Advanced Research Centre for Powder Metallurgy and New Materials, Hyderabad.

Keywords: Nanocrystalline, High Energy Ball Milling

High energy ball milling (HEBM) is widely used as top down process to synthesize nanostructured phases. There are several reports on HEBM of iron [1-4], and iron alloys [5]. These studies have revealed non-monotonic change in the lattice parameter along different crystallographic axes. Such anisotropic behavior restricts the use of conventional Williamson-Hall (WH) plot of x-ray diffraction (XRD) data for the estimation of crystallite size and lattice strain in iron and its alloys processed under severe deformation. So far very little information is available on the effect of alloying element(s) on the anisotropic behavior of ball milled nanocrystalline iron. In the present study, nanocrystalline Fe-20Cr-3Al powder was synthesized using HEBM and the effect of alloying elements on the anisotropy and structural changes of iron during milling was investigated.

Nanocrystalline Fe-20Cr-3Al alloy powder was prepared by ball milling of a blend of iron, chromium, and aluminium powders in appropriate proportion in a high-energy planetary ball mill for 20 h. A small quantity of the milled powder was taken out from the ball mill at a regular interval of 5, 10, 15, and 20 h for characterization. Shape and size of the milled powder was studied by SEM. Most of the ball milled powder particles showed irregular shape with a size of about 3 μm after 20 h of milling. XRD was done using Cu-K α radiation in a Rigaku-Smart Lab system (Rigaku Corp, Japan). The XRD data was analysed using WH

and modified-WH method to ascertain the characteristics of the ball milled Fe-20Cr-3Al powder such as crystallite size, lattice-strain, dislocation density, lattice parameter, and nature of dislocations.

A single phase BCC structure was evident from the XRD profile of Fe-20Cr-3Al powder after 20 h milling. Such observation indicates complete dissolution of aluminium and chromium in iron within 20 h of milling. The XRD peaks of the ball milled Fe-20Cr-3Al powder showed broadening as well as a shift toward low angle diffraction. The peak broadening of Fe-20Cr-3Al powder was analysed by WH method [6,7] which revealed an anisotropic behaviour. The broadening trend was found to be similar to ball milled pure iron till 10 h milling. The peak broadening trend changed after 10 h milling. This possibly indicates a change in the elastic modulus of iron due to the addition of chromium and aluminium in the solid solution. The WH method was found unsuitable for accurate estimation of the crystallite size of milled Fe-20Cr-3Al powder because of the anisotropic behavior. Thus, the crystallite size and micro strain of the ball milled Fe-20Cr-3Al powder was calculated by modified-WH method. The crystallite size showed gradual decrease to about 17 nm after 20 h milling (Fig. 1a) while the lattice parameter during milling showed gradual increase with milling time (Fig. 1a). The formation of nanocrystalline Fe-20Cr-3Al alloy after 20 h milling was also confirmed from transmission electron microscopy (TEM)

studies (Fig. 1b). The selected area electron diffraction (SAED) of 20 h milled powder (inset of Fig. 1b) revealed multi-ring patterns, which also suggests the nanocrystalline nature of the milled powder. The dislocation density was calculated by the model given by Williamson and Smallman[10] and it was found that the dislocation density increases with increase in milling time. The increase in the dislocation density indicates increase in the extent of deformation during HEBM.

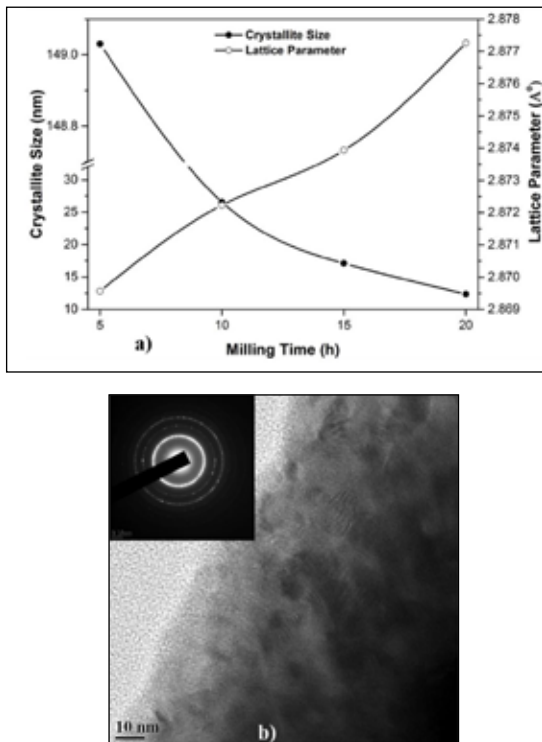


Fig. 1: a) Change in crystallite size and lattice parameter with milling time and b) TEM and SAED image (inset) of 20 h milled Fe-20Cr-3Al powder

Nanocrystalline Fe-20Cr-3Al alloys powder was successfully prepared from the as received powder by ball milling for 20 h. The crystallite size of the milled powder showed gradual decrease up to 17 nm while the dislocation density was found to increase up to $1.40 \times 10^{16} \text{ m}^{-2}$ after 20 h milling. The crystallite size of the ball milled

Fe-20Cr-3Al powder estimated by XRD matched closely with the crystalline size obtained from TEM.

References

1. R. K. Khatirkar and B. S. Murty, "Structural Changes in Iron Powder during Ball Milling," *Mater. Chem. Phys.*, 123, 247-253, (2010).
2. G. K. Rane, U. Welzel, S. R. Meka, and E. J. Mittemeijer, "Non-monotonic Lattice Parameter Variation with Crystallite Size in Nanocrystalline Solids," *Acta Mater.*, 61, 4524-4533, (2013).
3. Y. H. Zhao, H. W. Sheng, and K. Lu, "Microstructure Evolution and Thermal Properties in Nanocrystalline Fe During Mechanical Attrition," *Acta Mater.*, 49, 365-375, (2001).
4. H. H. Tian and M. Atzmon, "Kinetics of Microstructure Evolution in Nanocrystalline Fe Powder during Mechanical Attrition," *Acta Mater.*, 47, 1255-1261, (1999).
5. H. G. Jiang, H. M. Hu, and E. J. Lavernia, "Synthesis of Fe-rich Fe-Al Nanocrystalline Solid Solutions using Ball Milling," *J. Mater. Res.*, 14, 1760-1770, (2011).
6. T. Ungar, A. Revesz, and A. Borbély, "Dislocations and Grain Size in Electrodeposited Nanocrystalline Ni Determined by the Modified Williamson-Hall and Warren-Averbach Procedures," *J. Appl. Crystallogr.*, 31, 554-558, (1998).
7. G. K. Williamson and W. H. Hall, "X-ray Line Broadening From Filed Aluminum and Wolfram," *Acta Met.*, 1, 22-31, (1953).
8. T. Ungár, I. Dragomir, Á. Révész, and A. Borbély, "The Contrast Factors of Dislocations in Cubic Crystals: The Dislocation Model of Strain Anisotropy in Practice," *J. Appl. Crystallogr.*, 32, 992-1002, (1999).
9. A. Revesz, T. Ungár, A. Borbély, and J. Lendvai, "Dislocations and Grain Size in Ball Milled Iron Powder," *Nanostructured Mater.*, 7, 779-788, (1996).
10. G. K. Williamson and R. E. Smallman, "Dislocation Densities in Some Annealed and Cold-Worked Metals from Measurements on the X-ray Debye-Scherrer Spectrum," *Phil. Mag.*, 1, 34-46, (1956).

MECHANICALLY ACTIVATED SYNTHESIS OF NANOCRYSTALLINE Cr_2AlC POWDERS

Y. Rajkumar, P.A. Aakash, S. Bhattacharya and B.B. Panigrahi

Department of Materials Science and Metallurgical Engineering,
Indian Institute of Technology Hyderabad, Kandi, Sangareddy, 502285, Telangana, India

Abstract

Nano-sized Cr_2AlC powders were synthesized at relatively low temperature by the mechanically assisted synthesis method using a high energy planetary ball mill. The formation of Cr_2AlC from chromium carbide (CrC_x) and Al powders was monitored by the XRD analysis with progression of ball milling. Synthesis was carried out at three sequential stages: preparation of CrC_x powders through reaction synthesis, mechanical activation of synthesized CrC_x powder through ball milling for different durations and synthesis of final product by adding Al to the milled CrC_x . The nanostructures of the synthesized powder were realized by the FESEM micrograph and XRD analyses. These analytical observations have revealed that the nanocrystalline Cr_2AlC particles were formed just after Al melting when heated with CrC_x powder milled for about 15hr. Very high purity Cr_2AlC powder with crystallite size smaller than 150 nm and acicular in shape with sharp edges; have been successfully obtained.

Keywords: Mechanical Activation, MAX phase, Mechanically Assisted Synthesis

Introduction

MAX phase materials are relatively new class of ternary carbides, feature a hexagonal crystalline structure and can be represented by a general formula of $\text{M}_{n+1}\text{AX}_n$ (MAX), where $n = 1, 2, \text{ or } 3$, M is an early transition metal, A is an A-group element, and X is carbon or nitrogen. Strong M-X bonds and weaker M-A bonds associated with nano-layered structure endow these solids with a unique combination of metallic and ceramic properties. For example, like metals, they are readily machinable, relatively soft (1-5GPa), damage tolerant, thermally and electrically conductive, resistant to thermal shock and plastically deformable at elevated temperature [1,2]. Moreover, these materials show autonomous crack healing at high temperatures in an oxidizing environment [3]. Ti_3SiC_2 , Ti_3AlC_2 and Ti_2AlC are most studied compounds among MAX phases. Cr_2AlC is one of the MAX phase

compounds, has better oxidation and corrosion resistance than Ti_3SiC_2 and Ti_3AlC_2 in MAX family at high temperatures [4, 5]. Theoretical studies revealed that Cr_2AlC has about 11% larger bulk modulus than Ti_3SiC_2 and exhibits relatively higher hardness (3.5-6.4GPa) and better compressive strength (1159GPa) [6, 7, 8]. So, Cr_2AlC is expected to be a more promising candidate for high temperature applications. In addition, the thermal expansion of Cr_2AlC is $12\text{-}13 \times 10^{-6}/\text{K}$, close to the super alloys. Hence Cr_2AlC has potential applications in protective coatings on the super alloys [5]. The possibility of depositing large area Cr_2AlC coatings on steel substrates was already demonstrated [9]. There are several methods including hot pressing, mechanically activated hot pressing, hot isostatic pressing and pulse discharge sintering to produce Cr_2AlC bulk ceramics from $\text{Cr}/\text{Al}/\text{C}$, $\text{Cr}/\text{Al}_4\text{C}_3/\text{C}$, AlCr_2/C or $\text{CrC}_{0.5}/\text{Al}$ starting powders [10-23]. However, the problems

MECHANICALLY ACTIVATED SYNTHESIS OF NANOCRYSTALLINE Cr_2AlC POWDERS

such as high synthesis temperatures (1300-1450°C), relatively lower density and high impurities (Cr_7C_3 or Cr_3C_2) were always found during synthesis of Cr_2AlC . Reducing the grain size in bulk materials has been a major technological challenge, which has not been overcome so far for these compounds. Recently Li et al. synthesized low temperature and high density fine grained Cr_2AlC (about 2 μm) ceramics by mechanical alloying and hot pressing [10]. Mechanical alloying based synthesis process can be used to produce fine powders from low cost starting powders. It is believed that the more fine and uniform particles are having advantage to improve the sinterability of powders and reduce the amount of pores. Tian et al. synthesized fine Cr_2AlC (2-8 μm) powders by molten salt method at around 1000°C [11]. Panigrahi et al. produced Cr_2AlC powders (about 9 μm) through two step reaction above 1100°C [12]. In the present work mechanically activated reaction synthesis technology was used to synthesize a fine-crystalline Cr_2AlC powders at relatively low temperatures using CrC_x and Al as a starting powders to prevent the loss of Al loss and particle growth. Production of pure and ultrafine MAX phase powder has several advantages over direct sintering of MAX phases, which widen the application area of the MAX phase compounds. Therefore it is reasonable to think to fabricate Cr_2AlC ultrafine powders that could be used to fabricate fine grain and dense Cr_2AlC bulk ceramics through pressureless sintering, which is beneficial technically and economically.

Experimental Procedure

Cr_2AlC powder synthesis was carried out in three stages: firstly, the CrC_x ($x = 0.5$) powder was produced at 1100°C for 2hr using Cr (99% purity, <45 μm , Sigma Aldrich) and graphite (99% purity, <10 μm , Sigma Aldrich) powders in 2:1 molar ratio in high pure Argon

atmosphere. In the second stage, high energy ball milling of synthesized CrC_x powders was performed in a Fritsch P-5 planetary ball mill for various milling durations of 10hr and 15hr, using tungsten carbide (WC) containers and balls. The weight ratio of the ball to powder was 15:1, the rotation speed of the containers was 300 rpm. In the third stage, preparation of required Cr_2AlC powders were done by the mixing of milled CrC_x powders (10 and 15hr) with the Al powders in 2:1.4 molar ratio and heated in the range of 700-1100°C for 2hr with 15°C/min high purity Argon atmosphere. Finally samples were cooled down to room temperature and crushed into the powders. The phase analysis of the powders was characterized by X-ray diffraction (XRD) with $\text{Cu K}\alpha$ radiation using PANalytical, Model: X'Pert PRO. Scanning Electron Microscopy (SEM) Carl-Zeiss, Model: Supra 40 was used to analyze the phase formation and particle morphology of the products. Reaction route of activated powders was studied by Netzch 4.0 differential scanning calorimetry (DSC) with the heating rate of 20°C/min in high purity Argon atmosphere.

Results and Discussion

The XRD pattern of CrC_x powder synthesized at 1100°C for 2hr which has been shown in Fig. 1. The result shows that the synthesized CrC_x mainly consists of Cr_7C_3 and Cr_3C_2 phases. The weight fractions of above two phases were found about 59% and 41% respectively. So the actual starting powders to prepare Cr_2AlC were above carbides and Al powders as shown in eq.1 [12].



The XRD patterns of the Cr_2AlC powders synthesized using coarse CrC_x (without milling) and Al powders has been shown in Fig. 2. Here the extra 40mol% of Al was used to compensate the Al loss due to vaporization at

MECHANICALLY ACTIVATED SYNTHESIS OF NANOCRYSTALLINE Cr_2AlC POWDERS

higher temperatures and to reduce the amount of residual carbides in the final product, which was already reported in the previous works [11, 15, 20]. The results indicate that the amount of Cr_2AlC phase increases with synthesis temperature (Fig. 2). The powder synthesized at 900°C contains Cr_2AlC as a major phase along with large amounts of chromium carbides and Cr-Al intermetallic phases. At 1100 and 1200°C the intensities of chromium carbides decreased, while the intensity of Cr_2AlC increased. However, powder contains little amount of Cr_5Al_8 phase. Increasing temperature seems to be beneficial for producing high purity powder, however to avoid the problem of evaporation of Al and also grain coarsening, further heating was avoided.

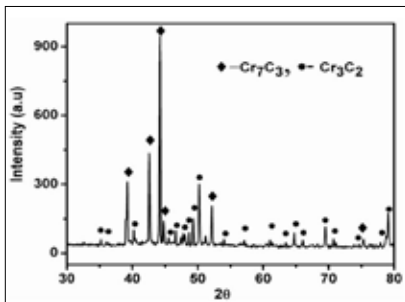


Fig. 1: XRD pattern of Cr_2AlC powders synthesized at 1100°C for 2hr

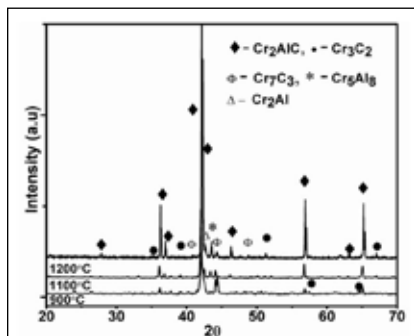


Fig. 2: XRD patterns of Cr_2AlC coarse powders synthesized at (a) 900°C , (b) 1100°C , (c) 1200°C for 2hr (from unmilled CrC_x and Al)

Fig. 3 illustrates the XRD patterns of Cr_2AlC powders fabricated from 10 and 15hr milled CrC_x and un-milled Al powders, which were heated in the temperature range of 700 to 900°C for 2 hrs. The formation of Cr_2AlC was observed at lower temperature (700°C); however, the powder was not of high purity. By increasing the synthesis temperature to 800°C only Cr_2AlC phase was detected with negligible carbides and other impurities. This could be attributed to the preservation of Al from evaporation; so that maximum amount of Al melt is available for reaction. Further increasing in temperature up to 1100°C , has no any considerable effect on Cr_2AlC purity, however the intensity of Cr_2AlC increased with synthesis temperature indicating the particle growth at high temperatures. DSC results also supported the Cr_2AlC phase formation and stability during the synthesis process. So the optimized temperatures to get fine and high purity Cr_2AlC powders are 800°C . Compare to the synthesis temperature of 1100°C , reported for achieving nearly pure Cr_2AlC powders, the present technique decreased the synthesis temperatures significantly. This is attributed the activation of CrC_x powders through providing high amount of milling energy; which enhances the reactivity of initial powders due to high surface area, high defect densities and strain accumulated during milling [24]. Figure 4 shows the XRD pattern of Cr_2AlC powders fabricated at 800°C from CrC_x powders milled at different milling durations of 10 and 15hr. The results showed that there is no significant change in phase formation of Cr_2AlC . The calculated crystallite sizes of the powders from the x-ray diffraction profile have been shown in Table 1. The crystallite size below 150 nm could be obtained in the present work.

MECHANICALLY ACTIVATED SYNTHESIS OF NANOCRYSTALLINE Cr_2AlC POWDERS

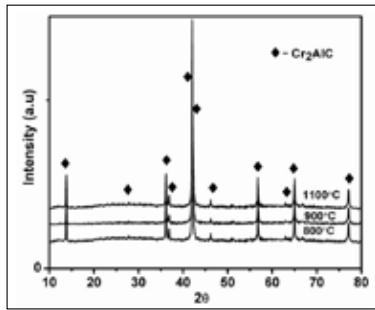


Fig. 3: XRD patterns of Cr_2AlC fine powders synthesized at (a) 800°C, (b) 900°C, (c) 1100°C after mechanical activation of CrC_x powders for 15hrs

TABLE 1. Crystallite size of Cr_2AlC powders obtained after reaction of Al with 15hr milled CrC_x

Synthesis temperature (°C)	Milling duration(hr)	Crystallite size (nm)
1100	15	327
900	15	182
800	15	124

Fig. 4 and 5 show the scanning electron micrographs of coarse and fine powders synthesized at 1100°C and 800°C respectively. In coarse structure there are many particles which are more than 20µm in size. The powders synthesized after mechanical activation of 15hr are in submicron size (<1µm). Powders were found to contain bimodal nature of particles; i.e., relatively larger particles and smaller particles, clearly visible in the SEM micrograph (Fig. 5). There are a significant amount of particles, which are smaller than 400 nm. Fig. 5(b) shows the fine Cr_2AlC particles of nano size crystallites as layered structures at low temperatures.

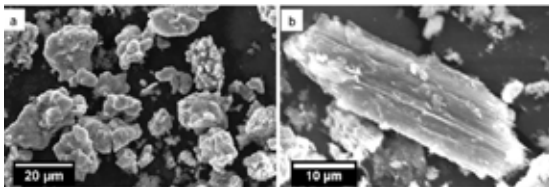


Fig. 4: (a) SEM micrographs of coarse Cr_2AlC powders synthesized at 1100°C for 2hr (b) Layered structure of a single Cr_2AlC particle

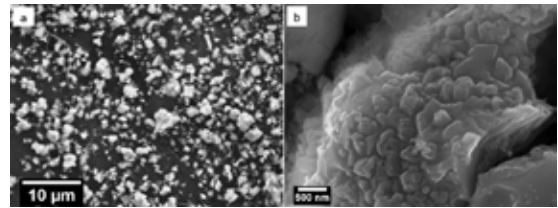


Fig. 5: (a) SEM micrographs of fine Cr_2AlC powders synthesized at 800°C for 2hr from 15hr milled CrC_x and Al (b) Cr_2AlC crystallite growth as a layered structure.

Differential scanning calorimetry performed with CrC_x and Al powders under flowing of Ar condition has been shown in Fig 6. It can be seen that for milled powders, there is an immediate exothermic reaction just after melting of Al. After the exothermic peak at around 700°C, almost there is no other peak up to 1400°C, which indicates that no further phase formation above 750°C except Cr_2AlC . On the other hand, un-milled reactant mixture shows smaller exothermic peaks and a large number of peaks spread over wide temperature range, confirming the formation of various undesirable phases.

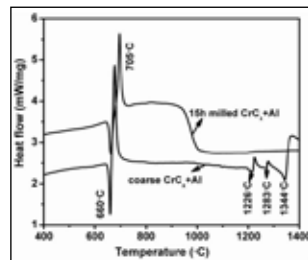


Fig 6: DSC curves profile of (a) un-milled CrC/Al (b) 15hr milled CrC/Al powders

Conclusion

This work studied the effect of mechanical activation of chromium carbide powders through the milling energy and reacting with aluminum powders on the formation of Cr_2AlC phase. The Cr_2AlC powders with smaller than 150 nm crystallite sizes with very high phase purity have been successfully prepared, at relatively lower temperature of 800°C. DSC analysis of the reactant mixture indicated the exothermic nature of the reaction.

MECHANICALLY ACTIVATED SYNTHESIS OF NANOCRYSTALLINE Cr₂AlC POWDERS

Acknowledgement

The SERB-DST (Govt. of India) is gratefully acknowledged for providing the financial support. Authors wish to thank to Dr. Atul S. Deshpande and Dr. S. Bhattacharya for useful discussions.

References

1. M. W. Barsoum, "The MAX Phases: A New Class of Solids; Thermodynamically Stable Nanolaminates", *Prog. Solid State Chem.*, 28, 201-81 (2000).
2. Z. M. Sun, "Progress in research and development on MAX phases: a family of layered ternary compounds", *Int. Mater. Rev.*, 56(3), 143 (2011).
3. G.M. Song, Y.T. Pei, W.G. Sloof, S.B. Li, J.Th.M. De Hosson, S. van derZwaag, "Oxidation-induced crack healing in Ti₃AlC₂ ceramics", *Scripta Mater*, 58, 13-16 (2008).
4. Z.J. Lin, M.S. Li, J. Y. Wang, Y. C. Zhou, "High temperature oxidation and hot corrosion of Cr₂AlC", *Acta Mater.*, 55, 6182-91(2007).
5. J.J. Li, M.S. Li, H.M. Xiang, X.P. Lu, Y. C. Zhou, "Short-term oxidation resistance and degradation of Cr₂AlC coating on M38G super alloy at 900-11000C", *Corrosion Science*, 53, 3813-3820 (2011).
6. J.M. Shrinder, Z. Sun, R. Mertens, F. Uestel, R. Ahuja, "Ab-initio calculations and experimental determination of structure of Cr₂AlC", *Solid State Commun.*, 130, 445-9 (2004).
7. M. W. Barsoum and M. Radovic, "Elastic and Mechanical properties of MAX phases", *Annu. Rev. Mater. Res.*, 41, 195-227 (2011).
8. W. Y. Ching, Y. Mo, "Electronic Structure and Mechanical properties of 20 MAX phase compounds", *26th Annual Conference on Fossil Energy Materials*, (2012).
9. C. Waller, DP Sigumonrong, T El-Reghy, J. M. Shrinder, "Towards the large area deposition of Cr₂AlC on steel", *Thin Solid films*, 515, 389-93 (2006).
10. S. B. Li, W. B. Yu, H. X. Zhai, G. M. Song, W.G. Sloof, S. Van der Zwaag, "Mechanical properties of low temperature Synthesized dense and fine grained Cr₂AlC Ceramics", *J. Euro. Ceram. Soc.*, 31, 217-24 (2011).
11. W.B. Tian, P. L. Wang, Y. Kan, G. J. Zhang, "Cr₂AlC powders prepared by moltensalt method", *J. Alloys Comp.*, 454-555, 132-8 (2007).
12. B. B. Panigrahi, M. C. Chu, Y-II Kim, S. J. Cho, "Reaction Synthesis and Pressureless Sintering of Cr₂AlC Powder", *J. Amer. Ceram. Soc.*, 93, No. 6 (2009).
13. Z. Lin, Y. Zhou, M. Li, J. Wang, " In-Situ Hot pressing of bulk Cr₂AlC Ceramics", *Z. Metallkd*, 96, 3 (2005).
14. W. B. Tian, Z. M. Sun, Y. Du, H. Hashimoto, "Synthesis reactions of Cr₂AlC from Cr-Al₄C₃-C by pulse discharge sintering", *Mater. Lett.*, 62, 3852-3855 (2008).
15. W. Tian, K. Vanmeensel, P. Wang, G. Zhang, Y. Li, "Synthesis and characterization of Cr₂AlC ceramics prepared by spark plasma sintering", *Mater. Lett.*, 61, 4442-4445 (2007).
16. G. Yinga, X. He, M. Li, W. Hana, F. He, S. Du, "Synthesis and mechanical properties of high-purity Cr₂AlC ceramic", *Mater. Sci. Engg.*, 528, 2635-2640 (2011).
17. Li-Ou, Xiao, S. B. Li, "Synthesis and Thermal Stability of Cr₂AlC Ceramics", *J. Euro. Ceram. Soc.*, 31, 1497-1502 (2011).
18. J. F. Li, T. Matsuki and R. Watambe, "Mechanical Alloying Assisted Synthesis of Ti₃AlC₂ powder", *J. Amr. Ceram. Soc.*, 85 (4), 1004 -1006 (2002).
19. S. B. Li, H. X. Zhai, G. P. Bei, Y. Zhou, "Synthesis and Microstructure of Ti₃AlC₂ by Mechanically Activated Sintering of Elemental powders", *Ceram. Int.*, 33, 169-173 (2007).

MECHANICALLY ACTIVATED SYNTHESIS OF NANOCRYSTALLINE Cr_2AlC POWDERS

20. M.Xue, X. Zhang, H. Tang, C. Li, "Synthesis of high purity Cr_2AlC nanolamellas with improved tribological properties for oil based additives", *Royal Soc. Chem.*, 4, 39280 (2014).
21. J. Zhu, H. Jiang, F. Wang, C. Yang, D.xiao, "Synthesis, microstructure and mechanical properties of $\text{Cr}_2\text{AlC}/\text{Al}_2\text{O}_3$ in situ composites by reactive hot press", *J. Euro. Ceram. Soc.*, 34, 4137-44 (2014).
22. Z. Lin, Y. Zhang, M. Li, "Synthesis, microstructure and property of Cr_2AlC ", *J. Mater. Sci. Tech.*, 23, 60721-46 (2007).
23. W. B.Tian, P. L. Wang, Y.-M. Kan, G.-J. Zhang, Y.-X. Li, D.-S. Yan, "Phase formation sequence of Cr_2AlC ceramics starting from Cr-Al-C powders", *Mater. Sci. Engg. A*, 443 (1-2), 229-234(2007).
24. C. Suryanarayana, Mechanical alloying and milling, *Prog. Mater. Sci.*, 46, 1-184 (2001).

PHYSICO-CHEMICAL CHARACTERIZATION OF RED MUD PRODUCED DURING EXTRACTION OF BERYLLIUM

B.M. Tripathi, Deep Prakash and P.K. Sinha

Powder Metallurgy Division, Bhabha Atomic Research Centre
Vashi Complex, Navi Mumbai - 400703

Abstract

Beryllium bearing solid waste is generated during the extraction of beryllium from its ore, beryl. This solid waste termed as red mud contains toxic beryllium at levels above the permissible limit and thereby prevents its direct disposal as solid waste. Therefore it becomes necessary to treat toxic red mud waste by suitable method and reduce water leachability of beryllium to acceptable limit for safe disposal. The present paper deals with detailed physical and chemical characterization of red mud with an aim to develop suitable method to fix beryllium in red mud waste. The physical characterization of red mud includes determination of major crystalline phases by X-ray diffraction (XRD), thermal behavior by differential thermal analysis (DTA), particle size distribution by laser diffraction. The chemical characterization mainly includes determination of chemical composition of red mud by energy dispersive X-ray fluorescence (EDXRF), total beryllium value and chemical form of beryllium in red mud. The study of physical and chemical properties of red mud is the foundation on which subsequent fixation of beryllium values is carried out.

Keywords: Beryllium, Red Mud

1. Introduction:

Beryllium and its compounds by virtue of unique combination of physical, mechanical and nuclear properties have varied applications in nuclear industry. Beryllium, due to low neutron absorption and high scattering cross section is used as neutron moderator and reflector in fission nuclear reactors. Beryllium is proposed as neutron multiplier material in International Thermonuclear Experimental Reactor (ITER) because it undergoes ($n,2n$) nuclear reaction when irradiated with high energy neutrons [1,2]. Because of its high thermal conductivity coupled with electrical resistivity, BeO is an ideal material for heat sinks in electronic circuits and packages. Beryllium-titanium intermetallic, called beryllide (Be_{12}Ti) an advanced material under consideration as neutron multiplier for fusion reactor. Advanced aluminium matrix-beryllium composites can find special applications in avionics,

space related optical systems and structural components for satellites, propellants etc due to its hybrid properties such as high modulus and low density of beryllium with the favourable fracture toughness, ductility and fabrication characteristics of aluminium [3]. In spite of having several applications in advance science and engineering, the high toxicity is major deterrent factor in usage of beryllium. The chronic exposure of beryllium causes a disease called berylliosis and skin dermatitis [4].

In India, beryllium is extracted on large scale from beryl ore. There are fairly large deposits of this ore available in India at different locations in Andhra Pradesh, Rajasthan and Bihar. Beryl ore, in its pure form is beryllium-aluminum-silicate ($3\text{BeO}\cdot\text{Al}_2\text{O}_3\cdot 6\text{SiO}_2$). A typical chemical composition of beryl is as follows: BeO (11-12%), Al_2O_3 (19%) and SiO_2 (64%), alkali metal oxides (1-2%) and minor amount of other oxides [5]. Sodium silicofluoride process is

PHYSICO-CHEMICAL CHARACTERIZATION OF RED MUD PRODUCED DURING EXTRACTION OF BERYLLIUM

used for extraction of beryllium from beryl. Sodium silicofluoride selectively fluorinates and renders beryllium value of the ore water soluble. Subsequently, beryllium is leached with water and around 60-70% of the ore remains as solid waste which is termed as red mud [5].

Red mud is considered to be toxic waste as it contains beryllium at levels above the permissible limit [6]. Therefore it can't be disposed directly as solid waste without proper treatment. The study on treatment strategies of red mud waste for beryllium fixation is scanty. There is no well established method till date for treatment and safe disposal of red mud generated during extraction of beryllium.

The broad objective of present work is to develop suitable method for treatment and safe disposal of toxic red mud waste. The first phase of work which is discussed in this paper involves physical and chemical characterization of red mud using several techniques such as Energy dispersive X-ray diffraction (EDXRF), Inductively coupled plasma atomic emission spectroscopy (ICP-AES), Thermogravimetric coupled with differential thermal analysis (TG-DTA), X-ray diffraction (XRD) etc. This work is very useful as it lays down foundation for development of technology for treatment and safe disposal of toxic beryllium containing red mud waste generated during extraction of beryllium in the plant.

2. Materials and methods:

Red mud was obtained from beryllium plant at Bhabha Atomic Research Centre (BARC), Vashi. Analar grade acids (HF and HNO₃) from Sigma-Aldrich were used wherever required during physico-chemical characterization of red mud. The chemical composition of major elements in red mud was determined by EDXRF spectrometer (Oxford, UK.). The concentration of total beryllium

in red mud and trace element composition was determined by microwave digestion of red mud sample and subsequent elemental analysis by ICP-AES (Horiba, Japan). Particle size distribution of red mud was obtained by laser diffraction particle size analyser (CILAS, France). Thermal analysis of red mud sample was carried out in air using TG-DTA thermal analyser instrument (Setaram, France). X-ray diffractometer equipped with Cu-K α radiation (Inel, France) was used for recording XRD pattern of red mud. Pellets of red mud samples (40 mm dia, 12 mm height) were prepared using hydraulic press and subsequently heated at 900, 950 and 1000°C in muffle furnace. The red mud samples heat treated at 900, 950 and 1000°C were labeled as HT-1, HT-2 and HT-3 respectively.

3. Results and discussion:

3.1) Chemical composition:

The chemical composition of major elements in red mud is shown in Fig.1. The figure shows that silica and alumina are major constituents of red mud, followed by sodium oxide and others. It is to be noted that concentration of elements are customarily expressed as their corresponding oxides. Also, it is significant to note that the concentration of total beryllium

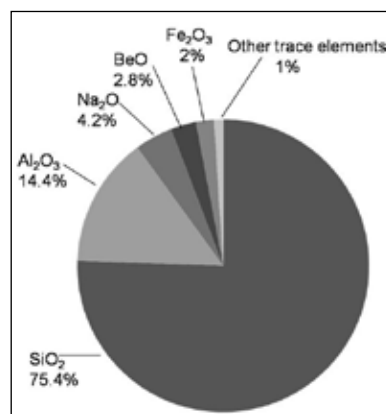


Fig. 1. Chemical composition of red mud

PHYSICO-CHEMICAL CHARACTERIZATION OF RED MUD PRODUCED DURING EXTRACTION OF BERYLLIUM

in red mud was estimated to be around 10,000mg/kg, whereas permissible limit for beryllium-bearing solid waste for direct disposal is 50mg/kg which renders the red mud hazardous and calls for special treatment for safe disposal.

3.2) Particle size distribution:

Fig.2 shows particle size distribution of the Red mud, as received from the process. The median of the particles is at 27.98 μm , and the maximum size is 81.67 μm . Since the leaching step pertains to separation of soluble (beryllium in the form of sodium beryllium fluoride) from the insolubles (SiO_2 , alumina and unreacted beryl and sodium silicofluoride), the size reduction of sintered mass during ball-milling helps in the process. However, the particle size distribution exhibit tri-modal distribution thus indicating further scope in improvement in the ball-milling process. At this juncture, it is important to mention that finer the size of red mud particles, better would be its leachability and hence better extraction of beryllium values. This would also mean lower values of beryllium in waste (red mud) thus making it less hazardous and easy to fixate.

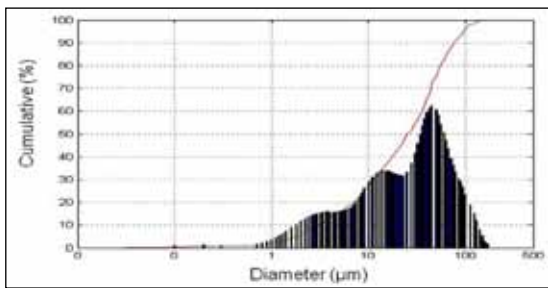


Fig.2. Particle size distribution of red mud

3.3) Thermal analysis:

The result of TG-DTA analysis of red mud is depicted in Fig.2. Two important features that can be revealed from TG-DTA curve are i) small weight loss region in 700-800°C and ii) a broad

endothermic peak centered at around 900°C. The weight loss is probably due to decomposition of unreacted sodium silicofluoride in red mud. The broad endothermic peak may be attributed to combination of phenomena such as decomposition of unreacted sodium silicofluoride, melting and formation of glassy phase of red mud occurring in temperature range 800-1000°C. It is worth to mention here that this temperature range where melting and formation of glassy phase may take place, could be very useful for beryllium fixation.

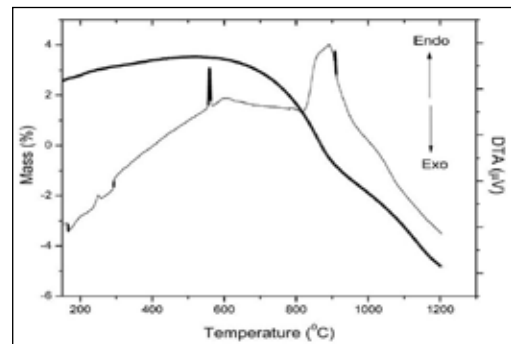


Fig.3. TG-DTA analysis of red mud

3.4) Phase characterization:

The result of XRD analysis of red mud is presented in Fig.4. The XRD pattern of red mud shows reflections that closely match with cristoballite phase along with few unidentified peaks. This is in accordance with selective reaction of sodium silicofluoride with beryllium value of the beryl ore leaving silica component unreacted in the red mud. The effect of heat treatment on phase characteristics of red mud is also shown in Fig.4. The XRD pattern of red mud heat treated at 900°C (sample:HT-1), shows a broad peak centered at two theta 25.0. This may be attributed to the transformation of cristoballite phase into glassy phase on heat treatment of red mud at 900°C which is also supported by endothermic peak in DTA (Fig.3.). The formation of glassy

PHYSICO-CHEMICAL CHARACTERIZATION OF RED MUD PRODUCED DURING EXTRACTION OF BERYLLIUM

phase is also evident from visual examination of sample HT-1. The photograph of sample HT-1 is shown in Fig.5. However, the glass is not fully transparent instead partially opaque. The heat treatment of red mud at 950°C results in emergence of crystalline peak again at same 2θ value as in crystoballite as shown in XRD pattern of sample HT-2. This may be due to recrystallisation of glassy phase into crystoballite. The XRD pattern of heat treated sample at 1000°C exhibits sharp peak having close resemblance with XRD peak corresponding to quartz phase. It is significant to mention here that XRD analysis shows

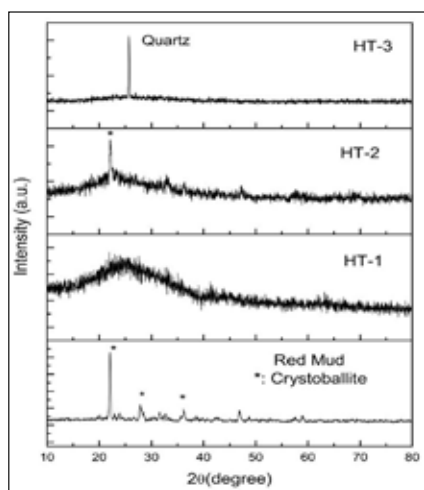


Fig.4. XRD pattern of as received and heated red mud



Fig.5. Photograph of red mud and HT-1 sample

formation of glassy, crystalline or mixture of both phases depending upon heat treatment of red mud which may facilitate the fixation of toxic beryllium.

4. Conclusion:

Red mud produced during extraction of beryllium contains toxic beryllium above the permissible limit. Therefore, proper treatment of red mud is required to fix beryllium for safe disposal. Silica and alumina are major chemical constituents of red mud along with sodium oxide and others. Thermal and XRD analysis shows that red mud can be transformed into glassy, crystalline or mixture of both phases depending upon heat treatment. These transformations may be useful for effective fixation of beryllium in red mud. Further study is underway to understand that whether glassy, crystalline or mixture of both phases are appropriate for effective beryllium fixation.

5. References:

1. D. Sathiyamoorthy, S. J. Ghanwat, B. M. Tripathi, C. Danani, "Novel mixed-oxide ceramic for neutron multiplication and tritium generation", *J. Nucl. Mater.*, 417(1-3), 775-779, (2011).
2. S. Saha, "Hydrometallurgy of beryllium in the Indian perspective", *Mineral Proc. Ext. Met. Rev.*, 13, 43-52, (1994).
3. D. D. Thorat, B. M. Tripathi, D. Sathiyamoorthy, "Extraction of beryllium from Indian beryl by ammonium hydrofluoride", *Hydrometallurgy*, 109 (1-2), 18-22, (2011).
4. B. M. Tripathi, J. Prakash, D. D. Thorat, D. Sathiyamoorthy, "Statistical Evaluation of Ammonium Hydrofluoride Process for Beryllium Extraction from Indian Beryl Ore", *Powder Metallurgy & Mining*, 2 (4), 4-7, (2013).
5. S. Saha, P. R. Roy, "Assessment of Waste of a Beryllium Extraction Plant", *J. Waste Management*, 12, 17-21, (1992).
6. Ministry of Environment and Forests, Draft Notification Of Hazardous Waste Management and Handling Rules, (1997).

STUDY OF POWDER FORGED PROPERTIES OF GEAR MATERIAL

J.D.Khatri, V.T.Thavale, N.B.Dhokey

Department of Metallurgical Engineering, College of Engineering, Shivajinagar, Pune-411 005, India

Abstract

Gears for engineering applications are normally manufactured by forging a blank, turning, hobbing, shaving and heat treatment followed by grinding. Due to the size of the gear, the net shape capability of powder metallurgy methods can be cost effective in place of conventional manufacturing. In the proposed research, sintering at 1120 °C was employed for Astaloy 0.45 Mo alloys (0.45 % Mo, 0.3% C, Fe balance) in reducing atmosphere having gas mixture of N₂: H₂ (90/10 by % volume) followed by close die powder forging. Forged specimens were characterized for density, hardness and microstructure. An optimum forging parameters were optimized which results in maximum achievable density of 98% of the theoretical density and hardness of 95 HRB.

Key words: Hardness, Density, Sintering, Compaction, Powder Forging.

1. Introduction

The slipping of a belt or rope is a common phenomenon in the transmission of motion or power between two shafts. The two most competitive high volume manufacturing processes for gear are wrought processing and powder metallurgy. Powder alloys have been widely used to produce high performance components [1]. Powder Metallurgy (PM) offers a versatile and efficient method for producing engineering parts and components especially for application in heavy duty components like gears, piston and connecting rod; today the fraction is rather between 70% and 80%. PM technique has been developed rapidly in recent years as a profitable technology owing to attractive features such as good strength, easy formability, near net shape manufacturability and competitive cost [2]. Higher relative density is one of the most important factors for producing high quality PM parts since the density strongly influences the physical and mechanical properties [3]. Mechanical behavior of sintered PM alloys is significantly influenced by the inherent

porosity, which can be removed to a great extent when the sintered alloys are subjected to cold or hot forging subsequent to sintering [4]. PM technique embraces both primary and secondary deformation processes. Primary deformation processes involves a PM technique and secondary deformation process involves powder forming technique such as powder preform forging, powder extrusion and powder rolling etc. Secondary deformation takes importance only when full densification is necessary to impart in the preforms [5]. The production of parts by powder forging is rapidly gaining acceptance as a competitive process for the production of high performance parts. Since it blends the time, material and cost saving advantages of conventional PM with the high production rates and property enhancement of conventional forge [6]. The two broad categories of forging process are open die forging and close die forging. The close die forging in which flash does not form (hence the term flash less forging), and the work piece completely fills the die cavity. Consequently, the forging pressure is very high, and accurate control of the blank volume and proper die

STUDY OF POWDER FORGED PROPERTIES OF GEAR MATERIAL

design are essential in producing a forging with the desired dimensional tolerances. Undersized blanks prevent the complete filling of the die cavity; conversely, oversized blanks generate excessive pressures and may cause dies to fail prematurely or the machine to jam [7].

There are two basic forms of powder forging, (1) Hot upsetting, in which the preform experiences a significant amount of lateral material flow and (2) Hot repressing, in which a material flow during densification is mainly in the direction of pressing is referred to as hot coining. Upsetting between flat dies is applicable as a model for initial stage of closed die forging until the lateral flow of the preform forces the material against the die wall, Dead zones created during initial deformation in which densification lags behind other regions may be difficult to compact later on, when they are enclosed by a shell of denser and stronger material [8]. The densification process has been studied in terms of shape change and forging cracks. In the presented paper, a prealloyed powder (ASTOLY) was powder forged to improve understanding on the Forgeability and its properties with a view to establish suitable methodology to standardize powder forging process.

2. Experimental methods and procedure

A prealloyed powder ASTALOY (Make: Hognas India) was chosen for carrying out proposed work, having nominal chemical composition as 0.3% C, 0.45% Mo. The calculated theoretical density by rule of mixture is 7.80 g/cc. The powder properties were A.D 4.1 g/cc and particle mesh size 100 to 120 μm . Compaction process was used to make green compact of the prealloyed powder using Hydraulic Powder compaction machine (50T). Cold compaction at varying compacting pressures ranging from 500 to 700 MPa. Sintering was carried out in a tubular furnace having reducing atmosphere at 1120°C with controlled heating rate of 5°C/min and then soaked for 30 min. After that, specimens were

taken out of the furnace followed by forging at 600°C. The temperature was maintained during transport of specimens from sintering furnace to compacting press for forging by preheated ceramic boat along with specimen to avoid any heat loss. Original height of the specimen was 11.2 mm and diameter was 10 mm. For 600 MPa compacting sample, as the close die forging process was carried out with 40% height reduction forging pressure was 1089 MPa. Similarly, reducing height by 45%, 50%, and 55%, the Pressure was increased to 1239 MPa, 1590 MPa and 1810 MPa respectively. Forging pressure increases as the densification and height reduction increases which demands of higher ejection pressure. In thermo mechanical processing cycle (Fig.1), specimens were allowed to cool to 600°C from sintering temperature and then forged immediately followed by air cooling. Then, forged specimens were heat treated at 860°C for hardening.

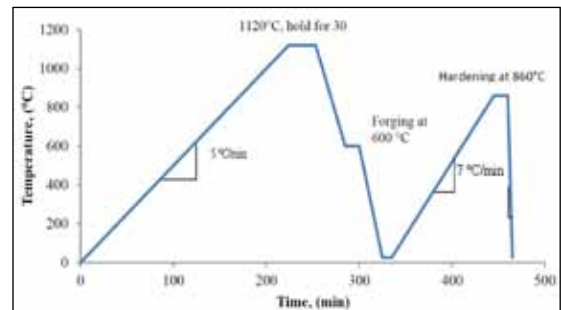


Fig.1 Schematic T-T diagram shows processing steps of thermo mechanical processing cycle.

3. Results and Discussion

3.1 Forgeability Limit

The maximum achieved density in green compact was 7.07 g/cc and then it increased to 7.15 g/cc due to sintering at cold compacting pressure of 600 MPa. As pressure is applied, the first response is rearrangement of the particles with filling of large pores giving a higher packing co-ordination. Increasing pressure provides better packing and leads

STUDY OF POWDER FORGED PROPERTIES OF GEAR MATERIAL

to decreasing porosity with the formation of new particle contacts. High pressure increases density by contact enlargement through plastic deformation as shown in Fig.2a. Sintered at 1120°C enhance mass transfer of diffusing atoms at higher temperature thereby improved strength and densification Fig.2b. It was essential to fix up optimum forging height of the specimen; therefore, four experiments were selected for varying height reduction in close die forging viz. (1) 40% reduced height was inadequate and it could not touch to the die wall with little increase in density 7.46 g/cc. (2) 45% reduced height gave rise to sufficient lateral flow of material which touches to the die wall but corners did not touch to the wall which has facilitated ejection of the specimen from die and achievable density was 7.50 g/cc. (3) 50% reduced height gave good surface finish, easy for ejection and improved density of 7.58 g/cc. and (4) 55% reduced height which resulted in excessive lateral flow thereby difficult to remove forged specimen from die and density was 7.65 g/cc. Overall, it was evident that 50% height reduction forging practice gave optimum forging condition.

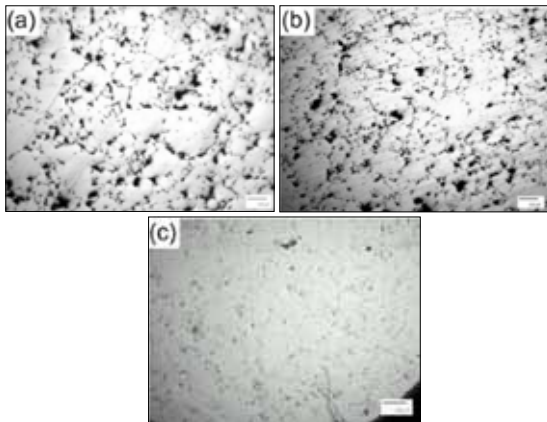


Fig.2 Unetched microscopic image shows porosity population of a cold compacted at 600Mpa (a) cold compacted specimen at 600 MPa (b) cold compacted specimen was sintered at 1120 °C (c) cold compacted sintered specimen forged at 600 °C with 50% height reduction

After forging, internal thermal stresses were developed into the specimens. Large Ferrite grains are visible in the microstructure of the cold compacted sinter forged and hardening (CCSFH) specimens, in which martensite is absent even after oil quench (Fig.3).

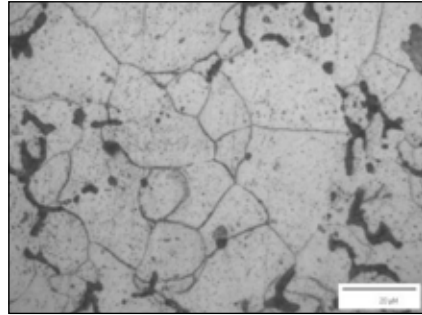


Fig.3. Microstructure shows grains of ferrite for CCSFH specimen ($P_c=600$ MPa, $T_s=1120^\circ\text{C}$, $T_f=600^\circ\text{C}$).

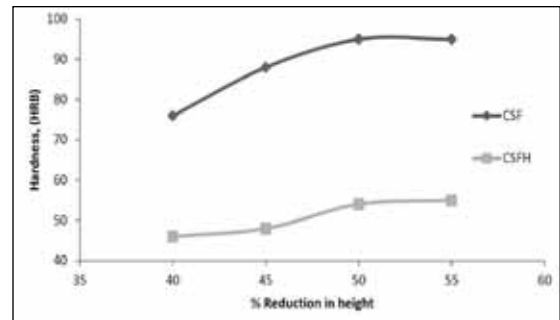


Fig.4 Effect of reduction in height on hardness of CSF and CSFH specimens.

CSF specimens having higher hardness than CSFH specimens, because of residual compressive stress present in the specimen. Maximum hardness achieved to 95 HRB by forging process but after heat treatment of forged specimen, hardness decreased to 55 HRB. Molybdenum is ferrite stabilizer which stabilizes ferrite phase in specimen. So, after heat treatment even oil quench process hardness reduces because there is no change in ferrite phase and no carbide formation occurs because of lower carbon availability.

STUDY OF POWDER FORGED PROPERTIES OF GEAR MATERIAL

In Astaloy 45 Mo powder approximately 98% of theoretical density of material can be achieved after forging and hardness achieved is 95 HRB. Presence of Molybdenum into material gives good compressibility to the material but Molybdenum is ferrite stabilizer and it stabilizes ferrite structure in specimen even after oil quench.

4. Conclusion

In the present context, the gear material Astaloy 45 Mo studied to understand density improvement by forging and effect on it with applied heat treatment and its subsequent quantification by microstructure and hardness. Based on the results, the following observations can be made.

1. In close die forging, 50% height reduction at 600 MPa pressure gives the highest density with increase in diameter by 20%. By forging to 50% height reduction in close die forging, increase in density by 97.94%. However, for compacting pressure of 700 MPa and 50% height reduction gives internal longitudinal crack, which corresponds to forging pressure of 1750 MPa.
2. Forging treatment improves hardness upto 95 HRB alloy powder compared to conventionally sintered specimen. Forging treatment results in decrease in porosity population and generates internal stress due to thermo mechanical treatment of alloy powder. Thus, forging process improves its ability to perform.

5. References

1. Q.Bai, J.Lin , "A Study of direct Forging Process for Powder Super alloys", *Materials Science and Engineering A* 621 (2015) 68-75.
2. H.Khorsand, M.Ghaffari, "Microstructural association Between Mechanical Behavior With Bending Fracture surfaces in Asaloy CrA Sintered Parts Alloyed By Cu and C," *Materials and design* 55(2014)979-986.
3. M.Azadbeh, A Mohammadzadeh, "Modeling the response of physical and Mechanical Properties of Cr-Mo Pre alloyed Sintered steels to Key Manufacturing parameters", *Materials and design* 55 (2014) 633-643.
4. A Rajeshkannan, K.S.pandey; "Some Studies on Sintered Cold Deformed Plain Carbon Steels", *Material and Design* 33(2012)115-120.
5. A. Rajeshkannan, K.S Pandey, "Some Investigation on the Cold Deformation Behaviour of Sintered Iron 0.8% Carbon Alloy Powder Preform", *Journal of Material Processing Technology* 203(2008)542-547.
6. K Sheikhi Moghaddam, M Ghambari; "Effect of Sinter Hardening on Microstructure and Mechanical Properties of Astaloy 85 Mo", *Journal of Iron and Steel Research, International*.2012, 19(10): 43-46.
7. Serope Kalpakjian,Steven R. Schmid," Manufacturing Engineering and Technology", *Sixth Edition IN SI Units*, Prentice Hall.(355-380)
8. "Powder Metal Technologies and Applications", *ASM Handbook Volume 7*, ISBN 0-87170-387-4. (409-411)

EFFECT OF Y_2O_3 ADDITION ON NON-LUBRICATED SLIDING WEAR BEHAVIOUR OF DUPLEX STAINLESS STEEL

Shashanka R., D. Chaira

Department of Metallurgical and Materials Engineering, National Institute of Technology Rourkela, India

Abstract

In the present work, non-lubricated sliding wear behaviour of nano-size (average particle size is 40 nm) Y_2O_3 (1wt. % Y_2O_3) dispersed duplex (Fe-18Cr-13Ni) stainless steel was studied. Yittria dispersed duplex stainless steel samples were cold compacted and then sintered at 1000, 1200 and 1400°C in tubular furnace using argon atmosphere for 1 hour. The sintered pellets were polished carefully and their density, hardness were measured by Archimedes and Vickers microhardness methods respectively. It has been found that both hardness and density increase with increase of sintering temperature. Microhardness values of duplex and yittria dispersed duplex stainless steel goes on increasing from 257 to 550HV25 and from 332 to 594HV25 respectively with increase in sintering temperature from 1000 to 1400°C. Density value increases from 66 to 90% in case of duplex stainless steel and 70 to 92% in case of yittria dispersed duplex stainless steel when sintering temperature increases from 1000 to 1400°C. Microstructures of consolidated stainless steel samples were studied by optical microscopy and scanning electron microscopy. X ray diffraction (XRD) was carried out to study the phase transformation of stainless steel during sintering at different temperatures. XRD analysis shows the presence of intense austenite phase than ferrite at higher temperatures. The amount of ferrite phase decreases with increase in sintering temperature from 1000 to 1400°C. Wear volume of both the stainless steel samples were calculated by using Archard equation. The volume of wear debris produced decreases with the dispersion of nano Y_2O_3 and increasing sintering temperature.

Key words: Powder metallurgy, Duplex stainless steel, Sintering, Phase transformation

1. Introduction

Duplex stainless steel is the combination of almost equal proportions of austenite and ferrite phases, but their proportions may vary depending upon the methods of preparation, composition and experimental conditions. This combined effect improves the corrosion resistance, high strength, good weldability, low thermal expansion, high energy absorption, good high-temperature tensile and creep strength of individual phases [1]. Therefore duplex stainless steel is one of the important grades of stainless steel mainly used in oil, petrochemical, marine, nuclear power, chemical, paper and pulp industries [2-5].

The amount of austenite and ferrite volume percentage depends upon the extent of heat

treatment and re-crystallization. Austenite and ferrite phases in duplex stainless steel impart corrosion resistance and toughness respectively [6]. Duplex stainless steel exhibits improved mechanical properties such as yield strength, tensile strength, toughness and low percentage elongation due to the presence of interstitial atoms and inter-metallic phases which act as obstacles for dislocation motion [5, 7]. Due to the wide range of applications of duplex stainless steel, many researchers are working to improve the structure and properties of duplex stainless steel by bringing down their structures to nano range and also by adding metal oxide dispersing agents.

One of the widely accepted methods to refine the structure of materials is by mechanical alloying

(MA) route [8]. MA involves bulk synthesis of utmost refined materials at a very short interval of time and less possibility of oxidation of materials. Oxygen active dispersing agents like Y_2O_3 nanoparticles can also improve the thermal, mechanical properties of duplex stainless steel. Addition of yttria nanoparticles into duplex dual matrix imparts maximum strength to interfacial bonding, hinders grain growth, results in phase transformation and increases the hardness of the materials [9-12]. Therefore, we have prepared duplex (Fe-18Cr-13Ni) stainless steel powders by MA method using specially designed dual drive planetary mill (DDPM). The design, fabrication and parameters of the mill and powder synthesis were reported by the authors in their previous publication [8].

Pandya et al. consolidated austenitic stainless steel at 1200, 1300, 1400°C temperatures and studied the effect of sintering temperature on the microstructure and mechanical properties of austenitic stainless steel. They concluded that density of austenitic stainless steel increases with increase in sintering temperature [13]. Vijayalakshmi et al. investigated the microstructural evolution, mechanical properties of duplex stainless steel at 1100, 1200, 1300 and 1350°C temperatures. They concluded that surface properties mainly depend upon the phases present in the stainless steel [14].

One of the important mechanical degradation of materials is wear. Wear involves the reduction of material dimension due to the loss of materials from contacting surface and results in wear debris. Wear leads to large gap between moving parts and causes maximum vibration, reduced efficiency, high noise, system malfunction etc [15]. Wear debris may be in the form flakes or powders depending upon the hardness of materials and they causes harmful contamination in food and beverage industries, it may block a valve in critical pipe lines, filters etc [15]. Hence, researchers put

their efforts to improve the wear resistance of materials.

Karak et al. investigated the effect of dispersoids like yttria nanoparticles and sintering temperature on the wear resistance of ferritic stainless steel. They consolidated yttria dispersed stainless steel by hot isostatic pressings at different temperatures under 1.2 GPa uniaxial pressure. They concluded that fretting wear resistance increases with increase in sintering temperature from 600, 800 and 1000°C [16]. Fargas et al. studied the wear resistance of commercial super duplex stainless steel at 875 and 975°C sintering temperatures. They found that hardness and wear resistance of super duplex stainless steel increases due to the increase in volume fraction of sigma phase at higher temperature. They reported wear mechanism was ductile abrasive and lower fatigue wear with ploughing and plastic deformation modes respectively [17].

In the present work, we studied the effect of yttria addition on the morphology, density, hardness and wear resistance of duplex and yttria dispersed duplex stainless steel fabricated by conventional sintering at 1000, 1200 and 1400°C in argon atmosphere.

2. Experimental

The duplex (Fe-18Cr-13Ni) stainless steels were prepared by planetary milling of elemental composition of Fe, Ni and Cr in a dual-drive planetary mill. The detailed procedure was explained by the authors in their previous paper [8]. Milled stainless steel powders were mixed with 1wt.% Y_2O_3 nanoparticles in a turbula shaker mixer (TURBULA® T2F, Willy A. Bachofen AG Maschinenfabrik, Switzerland) for 3 hours. Duplex and yttria dispersed duplex stainless steel powders are compacted using hydraulic press at 700 MPa with polyvinyl alcohol as binder. Compacted stainless steel samples are conventionally sintered at 1000, 1200 and 1400°C respectively in a tubular furnace with

EFFECT OF Y_2O_3 ADDITION ON NON-LUBRICATED SLIDING WEAR BEHAVIOUR OF DUPLEX STAINLESS STEEL

holding time of 1h each in argon atmosphere. Sintered stainless steel samples were then polished carefully to study the microstructure, density, microhardness and wear behaviour. Vickers microhardness studies were carried out using LECO-LM248AT fitted with a Vickers pyramidal diamond indenter. Carl Zeiss optical microscopy is used to study the microstructure of consolidated stainless steel samples and phase fraction was calculated by using Axio Vision Release 4.8.2 SP3 (08-2013) software. The consolidated stainless steel samples were characterized by X-ray diffraction (XRD) in a Philips PANalytical diffractometer using filtered Cu $K\alpha$ -radiation ($\lambda = 0.1542$ nm). The wear studies were carried out in Ball-on-plate wear tester (Ducom, TR-208 M1) using diamond indenter with 20rpm speed at room temperature. All the wear studies were performed at applied loads of 10 and 20N and with track radius of 4mm. Before and after wear tests, the diamond indenter was cleaned ultrasonically and dried. Wear track depth studies were carried out in Veeco Dektak 150 surface profilometer. Wear mechanism was studied by investigating the wear track and wear debris morphology by JEOL JSM-6084LV scanning electron microscopy.

3. Results and discussion

3.1 Phase analysis by XRD

Fig. 1 (a) and 1 (b) show the XRD spectra of duplex and yttria dispersed duplex stainless steel sintered at 1000, 1200 and 1400°C for 1 hour respectively. Diffraction spectra of both the stainless steels show sharp and crystalline diffraction peaks of ferrite and austenite phases. As sintering temperature increases from 1000 to 1400°C, the sharpness and crystallinity of stainless steel increases as shown in the figure. Milling increases the number of defect storage sites, shorter diffusion paths, amorphization and reduction in crystallite size and also increases the volume fraction of grain boundaries [18]. But sintering of milled powder leads to increase in

crystallite size, improvement of crystallinity; therefore XRD spectra show sharp peaks after sintering. Increase in sintering temperature increases the rate of diffusion, grain growth and the atomic periodicity. Fig. 1 (b) depicts the phase transformation from α -Fe to γ -Fe during sintering and results in more dominant austenite phase at higher temperature. As the sintering temperature increases from 1000 to 1400°C, the intensity and percentage volume of austenite phase increases and it becomes more dominant at 1400°C. But phase transformation is limited in case of duplex stainless steel even at higher temperature. The phase transformation is due to the dispersion of nano- Y_2O_3 in stainless steel matrix. The interstitial site of ferrite is very less compared to austenite, therefore dispersed yttria diffuses into the smaller interstitial sites of ferrite crystallites and forms mismatch strains [8]. This results in phase transformation from α -Fe to γ -Fe and more research work is to be carried out to study the role of yttria during austenitic stabilization.

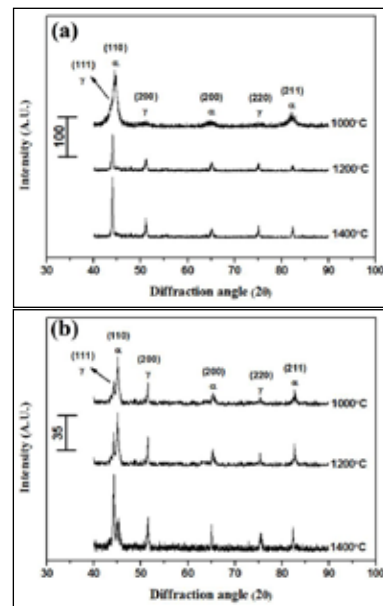


Fig. 1 XRD spectra of (a) Duplex and (b) Yttria dispersed duplex stainless steel samples sintered at 1000, 1200 and 1400°C

3.2 Microstructure and phase analysis

Fig. 2 (a) and 2 (b) represents the optical micrographs of duplex and yttria dispersed duplex stainless steel samples consolidated at 1000, 1200 and 1400°C respectively. Sintering was carried out at different temperatures to study the microstructural evolution and phase transformation in both cases. The porosity ratio decreases with increase in sintering temperature as shown in the micrographs. Pandya et al. reported material dissolution in the interior of stainless steel at 1400°C [13] and we also obtained similar results of material dissolution of both the stainless steel at 1400°C. The volume percentage of austenite phase increases with increases in sintering temperature and therefore we carried out an investigation to study the effect of sintering temperature on the volume fraction of ferrite and austenite phase in both the stainless steels by Axio Vision Release software. It was found that the volume fractions of austenite phase increases with increase in sintering temperature due to favourable phase transformation from α -Fe to γ -Fe at higher temperatures. Amount of austenite phase increases from 51 to 65 volume fractions with increasing temperature from 1000 to 1400°C in case of duplex and from 57 to 72 volume fractions in case of yttria dispersed duplex stainless steel. In the micrographs, ferrite (α -white), austenite (γ -grey) and pores (P-black) are shown.

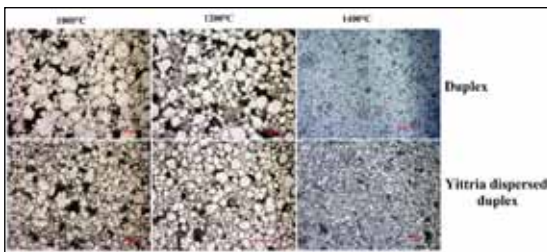


Fig. 2 Optical microstructure of duplex and yttria dispersed duplex stainless steel samples sintered at 1000, 1200 and 1400°C (P- Pores)

3.3 Density and hardness study

Fig. 3 represents the effect of sintering temperature on the densities and microhardness (25gf load) of duplex and yttria dispersed duplex stainless steel respectively. Density of both the stainless steel samples increases with increase in sintering temperature from 1000 to 1400°C. This is due to the effective rate of diffusion at higher temperature and the higher degree of atomic periodicity in a dense pattern. Density of duplex and yttria dispersed duplex stainless steel increases from 71 to 91% and from 78 to 94% respectively at sintering temperature of 1000 to 1400°C. The yttria dispersed duplex stainless steel exhibits higher density than yttria free duplex stainless steel. The addition of yttria nanoparticles hinders the grain growth and this results in higher density values. Optical microstructure confirms the low porosity ratio at higher sintering temperature and hence more density and hardness values for both the stainless steels.

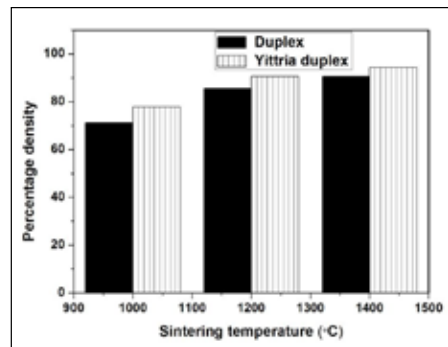


Fig. 3 Graph of Percentage sintered density of Duplex and Yttria dispersed duplex stainless steel sintered at 1000, 1200 and 1400°C

The Vickers microhardness values for duplex and yttria dispersed duplex stainless steel were calculated using the relation [19].

$$HV = 1.8544 \frac{P}{d^2} \quad (1)$$

EFFECT OF Y_2O_3 ADDITION ON NON-LUBRICATED SLIDING WEAR BEHAVIOUR OF DUPLEX STAINLESS STEEL

Where, P is the applied load and d is the diagonal length of the indentation. From the Fig. 3 it is confirmed that yttria dispersed duplex stainless steel samples show more hardness values than yttria free duplex stainless steel. This is due to yttria effect, where yttria imparts more strength to stainless steel. The Vickers microhardness values of duplex and yttria dispersed duplex stainless steel changes from 257 to 567HV₂₅ and 332 to 576HV₂₅ respectively for variation of sintering temperature from 1000 to 1400°C. Fig. 4 (a) and 4 (b) shows the effect of indentation load on microhardness of duplex and yttria dispersed duplex stainless steel samples sintered at 1000, 1200 and 1400°C respectively.

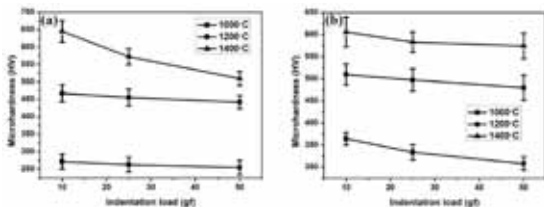


Fig. 4 Effect of indentation load (10, 25 and 50gf) on Vickers microhardness of (a) Duplex and (b) Yttria dispersed duplex stainless steel samples sintered at 1000, 1200 and 1400°C

The Vickers micro hardness measurements of all the stainless steel samples were carried out at 10, 25 and 50gf loads with a dwell time of 10 seconds. At least 5 trials of indentations were made and the average values of the diagonal lengths of indentation marks were measured as hardness in both the stainless steels. From the Fig. 4 it is observed that hardness values of stainless steels decreases with increase in applied indentation load due to indentation size effect (ISE) [6, 20]. The ISE can occur due to the surface effect; strain gradient effect based on mass transport by point defects, work hardening during indentation, indentation elastic recovery, surface dislocation pining [20-22]. The values of volume fractions, density

and hardness of austenite and ferrite phases of duplex and yttria dispersed duplex stainless steels sintered at different temperatures are tabulated in Table 1.

3.4 Wear behaviour study

Fig. 5 (a) and 5 (b) represent the variation of wear depth with sliding time for duplex and yttria dispersed duplex stainless steel sintered at 1000, 1200 and 1400°C at 10N applied load. From the optical microstructures it is clear that the stainless steel samples sintered at 1000°C depicts irregular shape and size, sharp edge pores, higher porosity ratios and ineffective diffusion of atoms results in less harder materials. But at 1400°C, the grains become more spherical, exhibit maximum density due to shrinkage of compact and formation of hard austenite phase. Hence, wear resistance of both the stainless steel samples increases with increase in sintering temperature.

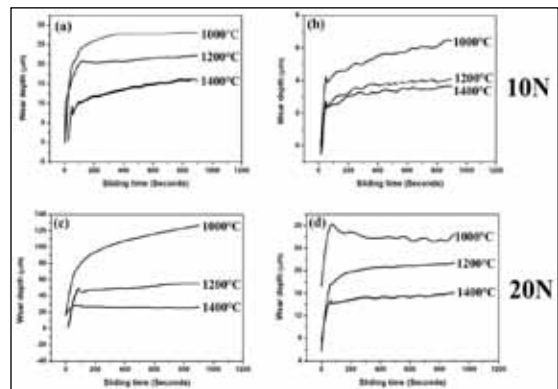


Fig. 5 Variation of wear depth with sliding time of (a, c) Duplex and (b, d) Yttria dispersed duplex stainless steel samples sintered at 1000, 1200 and 1400°C at 10N and 20N

From the microstructures it is confirmed that dispersion of yttria in stainless steel fortify the bonding between the atoms, enhances the phase transformation from α -Fe to γ -Fe, hinders the grain growth during sintering. Hence yttria dispersed duplex stainless steel

EFFECT OF Y₂O₃ ADDITION ON NON-LUBRICATED SLIDING WEAR BEHAVIOUR OF DUPLEX STAINLESS STEEL

show maximum wear resistance than yttria free duplex stainless steel. Fig. 5 (c) and 5 (d) represent the variation of wear depth with sliding distance for duplex and yttria dispersed duplex stainless steel sintered at 1000, 1200 and 1400°C at 20N applied load. As applied load increases from 10N to 20N, wear depth also increases as shown in the figures. This is due to the increase in coefficient of friction with increase in applied load [23]. The wear depth of duplex and yttria dispersed duplex stainless steel at 10N applied load is found to be 28 and 7µm. Similarly, the wear depth of duplex and yttria dispersed duplex stainless steel is found to be 127 and 30µm respectively at 20N. Fig. 6 (a) and 6 (b) shows a typical front view of depth of worn region of duplex and yttria dispersed stainless steel sintered at 1000°C respectively.

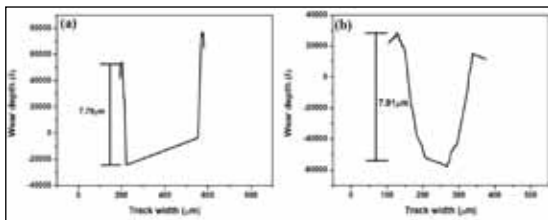


Fig. 6 Surface profilometer data of depth of worn region of (a) Duplex and (b) Yttria dispersed duplex stainless steel samples sintered at 1000°C

Generally the apparent depth of worn surface of stainless steel decreases with increase in sintering temperature and addition of yttria nano particles. Therefore, wear depth of duplex stainless steel is more than the wear depth of yttria dispersed duplex stainless steel. Hence, duplex stainless steel produces more volume of wear debris than yttria dispersed duplex stainless steel. Volume of wear debris can be calculated by using Archard equation [24] as follows,

$$Q = \frac{KWL}{H} \quad (2)$$

Where, 'Q' is the total volume of wear debris produced, 'K' is dimensionless constant, 'W' is total normal load, 'L' sliding distance and 'H' is the hardness of the softest contacting surface (stainless steel).

Fig. 7 (a) and 7 (b) represents the volume of wear debris produced at an applied load of 10N and 20N by duplex and yttria dispersed duplex stainless steels sintered at 1000 to 1400°C.

The volume of wear debris produced decreases with addition of yttria and increase in sintering temperatures due to higher density and hardness of materials. It is also observed that increase in applied load from 10 to 20N increases the volume of wear debris as shown in the Fig.7. The volume of wear debris produced at different sintering temperature at 20N loads is tabulated in table 1.

Table 1: The values of volume fractions, density, hardness and volume of wear debris produced by duplex and yttria dispersed duplex stainless steels sintered at different temperatures

Sample	Sintering Temperature (°C)	Volume fraction (%)	Theoretical density (g/cc)	Sintered density (%)	Vickers microhardness (HV _{0.05})	Volume of wear debris X10 ⁻⁴ (mm ³)		
							Austenite phase	Ferrite phase
Duplex stainless steel	1000	51	49	71.05	265	3.79		
	1200	62	38	85.55	455	2.16		
	1400	65	35	90.56	572	1.73		
Yttria dispersed duplex	1000	57	43	77.81	354	2.79		
	1200	65	35	7.80	90.60	497	1.97	
	1400	72	27	84.28	593	1.44		

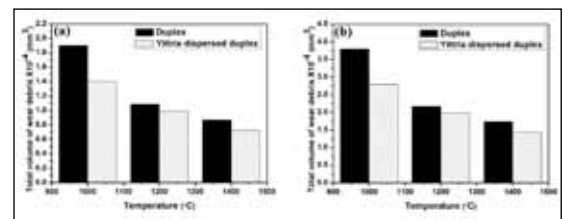


Fig. 7 Volume of wear debris produced by duplex and yttria dispersed stainless steel at (a) 10N and (b) 20N applied load sintered at 1000 to 1400°C

EFFECT OF Y_2O_3 ADDITION ON NON-LUBRICATED SLIDING WEAR BEHAVIOUR OF DUPLEX STAINLESS STEEL

3.5 Scanning electron microscopy analysis

The morphology of wear debris and worn surfaces has been investigated using SEM to study the wear mechanism and wear modes.

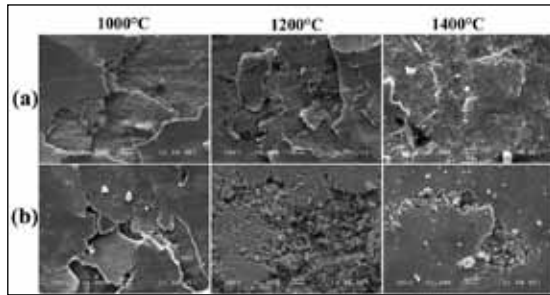


Fig. 8 SEM images of worn surface of (a) Duplex and (b) Yttria dispersed duplex stainless steel samples sintered at 1000, 1200 and 1400°C at 20N load

Fig. 8 (a) represents the worn surface of duplex stainless steel sintered at 1000, 1200 and 1400°C respectively at an applied load of 20N. As explained earlier, wear resistance, density and hardness increases with sintering temperature. SEM microstructures shows the clear indication of abrasive wear mechanism along with mild oxidation wear during wear study at 20N applied load at different temperatures. Fig. 8(b) represents the worn surface of yttria dispersed duplex stainless steel sintered at 1000, 1200 and 1400°C respectively at an applied load of 20N. Both the stainless steel follows same abrasive and mild oxidative wear mechanisms.

Fig. 9 (a), 9 (b) and 9 (c) represents the EDS spectra of duplex stainless steel sintered at 1000, 1200 and 1400°C temperature respectively. The extent of oxidative wear increases with increase in sintering temperature from 1000 to 1400°C as confirmed by EDS. Volume percentage of oxygen increases due to enhanced oxidation of Fe at higher sintering temperatures. Wear debris will be produced by work hardened mode rather than ploughing

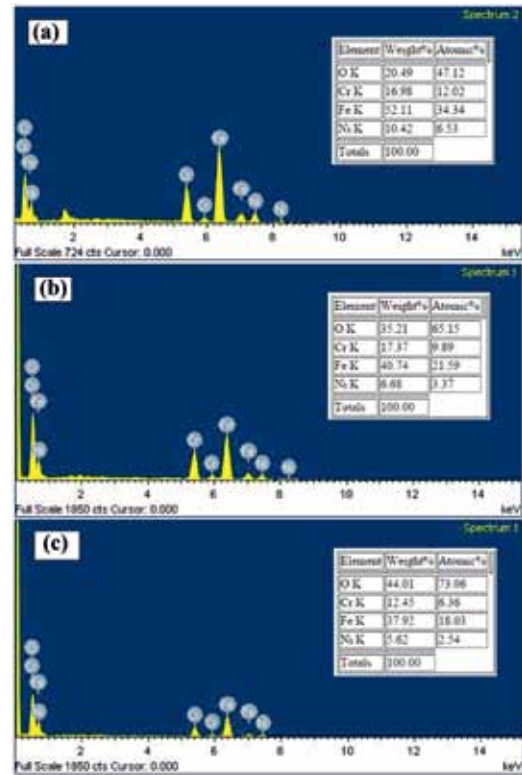


Fig. 9 EDS spectra of worn surfaces of duplex stainless steels at (a) 1000°C (b) 1200°C and (c) 1400°C at 20N load

mode due to higher hardness and brittleness of the stainless steel. As a result, wear debris detach from worn surface in the form of small particles instead of flakes. This leads to entrapment of metallic wear debris between the two contacting surfaces and dismantles the contacting interface to sufficiently small sizes. The surface area and surface energy of wear debris and wear surface is more and hence oxidation occurs very rapidly. Therefore we investigated the morphology of wear debris produced at 20N of 1400°C sintered stainless steels. During 10N applied load there is a negligible amount of wear debris produced and hence wear debris were collected at 20N applied load to study the wear mechanism.

EFFECT OF Y_2O_3 ADDITION ON NON-LUBRICATED SLIDING WEAR BEHAVIOUR OF DUPLEX STAINLESS STEEL

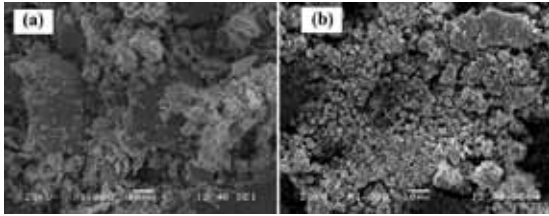


Fig. 10 SEM images of wear debris of (a) Duplex and (b) Yttria dispersed duplex stainless steel samples sintered at 1400°C at 20N load

Fig. 10 (a) and 10 (b) represents the wear debris of duplex and yttria dispersed duplex stainless steel respectively. The morphology of wear debris produced by duplex stainless steel is in the form of small flakes due to ductile nature. Whereas yttria dispersed duplex stainless steel produces work hardened particles as shown in the Fig. 10. From the morphology it is confirmed that both duplex and yttria dispersed duplex stainless steel undergoes abrasive wear mechanism with ploughing and plastic deformation modes respectively. From EDS it is confirmed that yttria dispersed duplex stainless steel is more prone to oxidation as the oxygen percentage is more than yttria free duplex stainless steel. Farias et al. [25], Quinn [26], Stott [27] and Jiang et al. [28] also observed similar kind of oxidative wear mechanisms.

4. Conclusions

Yttria dispersed and yttria free duplex stainless steel samples were fabricated by conventional sintering at 1000, 1200 and 1400°C and studied the effect of sintering temperature and yttria addition on microstructure, phase formation, density, hardness and wear behavior of stainless steel. Density, hardness, austenite phase formation (α -Fe to γ -Fe phase transformation) and wear resistance increase with increase in sintering temperature. Depth of worn surface increases with increase in applied load from 10 to 20N in both the stainless steels. XRD spectra

confirm the enhanced phase transformation from α -Fe to γ -Fe at higher temperature and yttria dispersion into duplex stainless steel. SEM microstructures of wear debris and contacting surface reveals the abrasive wear along with mild oxidation wear followed by ploughing (low sintering temperature) and plastic deformation (higher sintering temperatures) modes. Volume percentage of oxygen increases due to favorable oxidation of Fe at higher sintering temperatures. This is due to the detachment of very small particles from the contacting surfaces which leads to rapid oxidation due to large surface area and surface energy.

Acknowledgement

Financial support for this work from the Council of Scientific & Industrial Research (CSIR), India (Grant No. 22/561/11/EMR II Dated 11.04.2011) is gratefully acknowledged.

References

1. T. Karahan, H. E. Emre, M. Tumer, R. Kacar, "Strengthening of AISI 2205 duplex stainless steel by strain ageing", *Mater Des.*, 55, 250–256, (2014).
2. Y.Q. Wang, B. Yang, J. Han, F. Dong, Y.L. Wang, "Localized Corrosion of Thermally Aged Cast Duplex Stainless Steel for Primary Coolant Pipes of Nuclear Power Plant", *Pro Eng.* 36, 88–95, (2012).
3. S. Herenu, I. Alvarez-Armas, A.F. Armas, "The influence of dynamic strain ageing on the low cycle fatigue of duplex stainless steel", *Scripta Mater.*, 45, 739–745, (2001).
4. H. Miyamoto, T. Mirnaki, S. Hashimoto, "Super plastic deformation of microspecimens of duplex stainless steel", *Mater. Sci. Eng. A.*, 319, 779–783, (2001).
5. M.J. Schofield, R. Bradsha, R.A. Cottis, *Mater Performance.*, 35, 65–70, (2009).
6. R. Shashanka, D. Chaira, "Development of nano-structured duplex and ferritic stainless steels by pulverisette planetary milling followed

EFFECT OF Y_2O_3 ADDITION ON NON-LUBRICATED SLIDING WEAR BEHAVIOUR OF DUPLEX STAINLESS STEEL

- by pressureless sintering", *Mater. Charact.*, 99, 220-229, (2015).
- L.A. Dobrzanski, Z. Brytan, M. Actis Grande, M. Rosso, "Properties of duplex stainless steels made by powder metallurgy", *Arch. Mater. Sci. Eng.*, 28, 217-223, (2007).
 - R. Shashanka, D. Chaira, "Phase transformation and microstructure study of nano-structured austenitic and ferritic stainless steel powders prepared by planetary milling", *Powder Technol.*, 259, 125-136, (2014).
 - R. Liu, D.Y. Li, "Effects of yttrium and cerium additives in lubricants and corrosive wear of stainless steel 304 and Al alloy 6061", *J. Mater. Sci.*, 35, 633-641, (2000).
 - E. J. Felten, "High-Temperature Oxidation of Fe-Cr Base Alloys with Particular Reference to Fe-Cr-Y Alloys", *J. Electrochem. Soc.*, 108, 490-495, (1961).
 - C. S. Wukusick, J. F. Collins, "An iron-chromium-aluminum alloy containing yttrium", *Mat. Res. Standard*, 4, 637-646, (1964).
 - J. M. Francis, W. H. Whitlow, "The effect of yttrium on the high temperature oxidation resistance of some Fe-Cr base alloys in carbon dioxide", *Corr. Sci.*, 5, 701-710, (1965).
 - Shishir Pandya, K.S. Ramakrishna, A. Raja Annamalai, Anish Upadhyaya, "Effect of sintering temperature on the mechanical and electrochemical properties of austenitic stainless steel", *Mater. Sci., Eng., A.*, 556, 271-277, (2012).
 - K. Vijayalakshmi, V. Muthupandi, R. Jayachitra, "Influence of heat treatment on the microstructure, ultrasonic attenuation and hardness of SAF 2205 duplex stainless steel", *Mater. Sci. Eng. A.*, 529, 447-451, (2011).
 - C.X. Li, *Surface Engineering*, "Wear and Wear Mechanism", The University of Birmingham, UK, (1990).
 - S.K. Karak, C.S. Vishnu, Z. Witczak, W. Lojkowski, J. Dutta Majumdar, I. Manna, "Studies on wear behavior of nano- Y_2O_3 dispersed ferritic steel developed by mechanical alloying and hot isostatic pressing", *Wear*, 270, 5-11, (2010).
 - G. Fargas, A. Mestra, A. Mateo, "Effect of sigma phase on the wear behavior of a super duplex stainless steel", *Wear*, 303, 584-590, (2013).
 - M. Gojic, A. Nagode, B. Kosec, S. Kozuh, S. Savli, T. Holjevac Grguric, L. Kosec, "Failure of steel pipes for hot air supply", *Eng. Failure Anal.*, 18, 2330-2335, (2011).
 - Duyi Ye, "Investigation of cyclic deformation behaviour in the surface layer of 18Cr-8Ni austenitic stainless steel based on Vickers microhardness measurement", *Mater. Chem. Phys.*, 93, 495-503, (2005).
 - Ilze Manika, Janis Maniks, "Size effects in micro- and nanoscale indentation", *Acta Mater.*, 54, 2049-2056, (2006).
 - Jianghong Gong, Jianjun Wu, Zhenduo Guan, "Examination of the indentation size effect in low-load vicers hardness testing of ceramics", *J. Eur. Ceram. Soc.*, 19, 2625-2631, (1999).
 - H. Buckle, "The Science of Hardness Testing and its Research Application", J. H. Westbrook and H. Conrad, Metal Park, OH, American Society for Metals, 453-494, (1973).
 - Bharat Bhushan, "Modern Tribology Handbook", Vol. 2, CRC Press, (2000).
 - J. F. Archard, W. Hirst, "The Wear of Metals under Unlubricated Conditions, Proceedings of the Royal Society", A-236, 397-410, (1956).
 - M.C.M. Farias, R.M. Souza, A. Sinatora, D.K. Tanaka, "The influence of applied load, sliding velocity and martensitic transformation on the unlubricated sliding wear of austenitic stainless steels", *Wear*, 263, 773-781, (2007).
 - T.F.J. Quinn, "Review of oxidation wear, part 1: The origins of oxidation wear", *Tribol. Int.*, 16 (5), 257-271, (1983).
 - F.H. Stott, "The role of oxidation in the wear of alloys", *Tribol. Int.*, 31(1-3), 61-71, (1998).
 - J. Jiang, F.H. Stott, M.M. Stack, "Some frictional features associated with the sliding wear of the nickel-base alloy N80A at temperatures to 250 °C", *Wear*, 176 (2), 185-194, (1994).

MACHINABILITY OF SINTER-HARDENING PM MATERIALS WITH EXPERIMENTAL MACHINING ENHANCERS

Maryam Moravej¹, Francois Chagnon¹, Philippe Francois²

¹Rio Tinto Metal Powders, Tracy, Quebec, Canada

²Rio Tinto Metal Powders, Eschborn, Germany

Abstract

Although powder metallurgy is an economical method for production of near net shape components, machining operations are often required to deliver desired geometrical features, dimensional tolerances, and surface finish of PM parts. Machining enhancers are used to improve the machinability of PM components and to increase tool life. MnS is the most common machinability enhancer used for PM steel parts. However, it is less effective for harder materials and, especially, for sinter-hardening grades. It has also shown to stain steel parts and make them susceptible to corrosion. In this study the machinability of sinter-hardening materials with new experimental machining enhancers was investigated. Different additive formulations were evaluated and their performance was compared to that of the materials without machining enhancer and with MnS. Specimens were compacted, sintered, and cooled down at two cooling rates to evaluate the effect of post-sintering cooling rate on sintered properties and machinability. The results of the material characterization including dimensional change, static and dynamic properties, microstructural analysis, and machinability by drilling test are presented in this paper.

Keywords: Machinability, Machining enhancers, Sinter-hardening, Mechanical properties

Introduction

Machining enhancers (additives) are added in the initial powder mixture to enhance the machinability of PM parts after sintering especially in high strength steels. They should in general fulfil these requirements: mechanical and physical properties as well as dimensions of the sintered parts should be retained at the same values as for material without machining additives, and machinability should be improved [1].

Machining additives perform several functions during the cutting process: they promote microcracking and fracture of the chip/workpiece interface ahead of the cutting tip and prevent welding of the hot chips to form continuous swarf the removal of which is very complicated. They also prevent build-up edge formation in the area where local cutting forces and temperatures promote welding. A

third function is to act as complex lubricant and a barrier to diffusion in the region of the tool face behind the cutting edge where crater wear normally occurs. In general, machining additives have to decrease tool/chip friction thereby decreasing the cutting forces and the temperature in the cutting zone. This can result in improved surface finish and improved machinability [1-3].

The most common machining enhancer in PM industry is MnS. The beneficial effect of machining additives can be explained by the role of MnS which has been most frequently investigated. MnS inclusions act as stress concentration risers in the machining shear zone to initiate cracks that subsequently lead to fracture of the chip. These inclusions are also known to deposit a layer on the surface of the cutting tool. It means that MnS acts as lubricant in machining operation by minimizing tool/chip friction, reducing tool wear [1].

MACHINABILITY OF SINTER-HARDENING PM MATERIALS WITH EXPERIMENTAL MACHINING ENHANCERS

While MnS has many beneficial attributes, it has some limitations and potentially negative effects. The use of MnS may damage the sintering furnace through the production of a sulfur containing gas. In addition, MnS becomes less effective as alloy content increases and for sinter-hardening steel grades. It can also be detrimental to the mechanical properties of such grades. The other issue with MnS is that it can stain the PM parts after sintering and make them susceptible to corrosion [1,4]. In this context, alternative machining additives have been developed to enhance the machinability of PM steel components. Some examples of additive materials include oxides (CaO, MgSiO₃), fluorides (CaF₂), and temperature stable lubricants like talc, hexagonal boron nitride, and mica/bentonite [5-6].

As mentioned above, MnS is less effective to improve the machinability of sinter-hardening materials. One example of such materials is FLC-4608 that can be sinter-hardened or heat-treated with a microstructure mainly consisting of martensite with apparent hardness values ≥ 30 HRC. Therefore, these materials are very hard to be machined using conventional coated tools and often expensive cBN cutting tools are required. In this study the effect of new experimental machining additives on the machinability, physical and mechanical properties, and fatigue strength of sinter-hardening FLC-4608 was investigated and compared to the materials without additive and with 0.5% MnS.

Experimental methods

The master mix was prepared using ATOMET 4601 powder the composition of which is shown in Table 1. To the base powder 2% Cu, 0.9% graphite, and 0.75% wax were added to reach the MPIF FLC-4608 grade. The materials evaluated as machining additives were two non-sulfide conventional additives, lithium metaborate (LiBO₂), and lithium tetraborate

(LiB₄O₇). The borate glasses were used as it is believed that they can melt during machining where local temperatures are higher than their melting point being 850 and 917°C, respectively. The molten glasses can then act as lubricant on the tool during machining thereby improving tool life [7]. Different formulations of machining enhancers were prepared with at least one of the materials named above using Taguchi 8 arrays and added to the master mix. Two series of experiments using Taguchi 8 arrays were done giving a total of 16 new formulations of experimental additives. The mix without additive was used as reference and the one with 0.5% MnS was used for comparison.

Table 1 Composition of ATOMET 4601

Element	Fe	Mn	Mo	Ni	S	O	C
Wt. %	Bal.	0.19	0.54	1.84	0.009	0.1	0.008

To evaluate the green and sintered properties, standard TRS specimens were compacted from each mix to 7.0 g/cm³ density. For drilling machinability tests, ½ in thick (12.7 mm) TRS specimens were compacted to 7.0 g/cm³ density. The bars pressed with the first eight additive formulations were sintered at two conditions to evaluate the effect post-sintering cooling rate on their properties. The first sintering was done in 90% N₂-10% H₂ atmosphere for 25 min at 1120°C with a slow cooling rate of 0.3°C/s between 400 and 250°C. Second sintering parameters were 90% N₂-10% H₂ atmosphere, 35 min at 1130°C with a faster cooling rate of 1°C/s between 400 and 250°C. The specimens with the second series of additive formulations (ME11 – ME18) were sintered using only the fast cooling profile. All properties were evaluated after tempering at 200°C for 60 min.

The drilling tests were performed using Champion 705C cobalt HSS drill, ¼ in (6.35 mm) diameter, at rotating speed of 500 RPM, and feed rate of 0.64 mm/s. Three holes were

MACHINABILITY OF SINTER-HARDENING PM MATERIALS WITH EXPERIMENTAL MACHINING ENHANCERS

drilled on each specimen with a cutting depth of 0.47 in (12 mm). Average and maximum thrust forces were measured for each hole until tool failure or reaching the maximum number of holes for each material.

After the initial evaluations and the selection of more efficient additive formulations, tensile tests were performed on dog-bone specimens pressed to 7.0 g/cm³ density from the mixes containing the new additives, 0.5% MnS, and no additive. Also plane bending fatigue test was performed with R=0.1 load ratio and the fatigue limit at 50% survival value was determined using the staircase method with a run out limit of 2.5 million cycles. The microstructures were observed using optical microscope after metallography preparation and Nital etch.

Results and discussion

Fig. 1 shows the difference in the dimensional change (DC) of the mixes containing the first series of new additive formulations with that of the reference material without additive (DC=0.215 %). The most similar DC to the reference was achieved for the mix 3 followed by mixes 4 and 2. The transverse rupture strength (TRS) and hardness of these mixes are also presented in Fig. 2. All machining enhancers reduced the mechanical properties of FLC-4608 material with some formulations (mixes 2, 4, 6, and 8) having less detrimental effect than others.

The FLC-4608 material without machining enhancer had low drilling performance as the tool broke only after three holes with a high average thrust force (Fig. 3). The machining enhancers improved the drilling machinability in terms of the average thrust force and number of holes drilled. Another measure of machinability is the slope of the average thrust force versus number of holes which is an indication of tool life. The experimental enhancers improved also the tool life as this

slope decreased significantly compared to the reference. Additives of mix 8 and mix 5 showed the highest performance among the formulations tested. Based on the results of the preliminary tests with the eight experimental formulations, four mixes (2, 5, 7, and 8) were selected for further evaluation of the effect of post sintering cooling rate on mechanical properties and machinability.

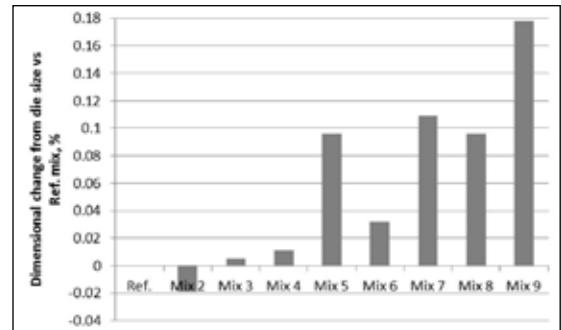


Fig.1 Dimensional change from die size: difference with the reference material without machining enhancer

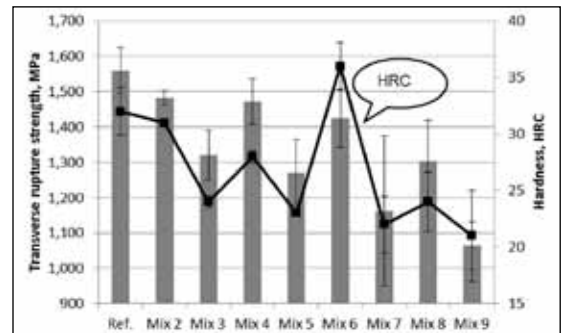


Fig.2 Mechanical properties of the mixes containing new additive formulations

For the specimens produced from mixes with the select additive formulations and fast cooled after sintering, the dimensional change from die size was very similar (less than ± 0.04 % difference) to that of the reference FLC-4806 material without additive, being 0.316 %. Fast cooling also reduced the negative effect of the experimental additives on the mechanical

MACHINABILITY OF SINTER-HARDENING PM MATERIALS WITH EXPERIMENTAL MACHINING ENHANCERS

properties, as shown in Fig. 4. Both TRS and hardness increased for the mixes with machining enhancers after fast-cooling. As illustrated in Fig. 5, drilling machinability of all materials tested decreased in terms of the average thrust force, and the slope of thrust force vs number of holes. For instance, the highest average thrust forces for the mix 8 increased from 75 lbf to 168 lbf, and the slope of average thrust force increased from 0.366 to 5.36 lbf/hole after sinter-hardening. Although the thrust forces increased for the sinter-hardened materials, the machining additives still improved the drilling performance of FLC-4608 material. Additive of mix 8 was selected for further evaluation of tensile and fatigue properties based on both its machining performance and its effect on the sintered properties.

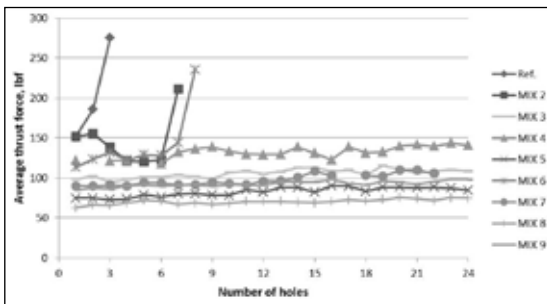


Fig.3 Drilling machinability of the mixes containing new additive formulations compared to the reference without additive: materials with slow cooling

Based on the results of the first series of experiments, another series of eight additive formulations was developed and tested. The materials containing these new additives were only tested in sinter-hardened condition. The drilling performance of these materials is illustrated in Fig. 6. Additive of mix 14 was selected from this series as it improved the machinability of FLC-4608 with acceptable sintered properties (DC=0.351%, TRS=1351 MPa, Hardness=27 HRC) compared to that of the reference without additive (DC=0.316%, TRS=1550 MPa, Hardness=29 HRC).

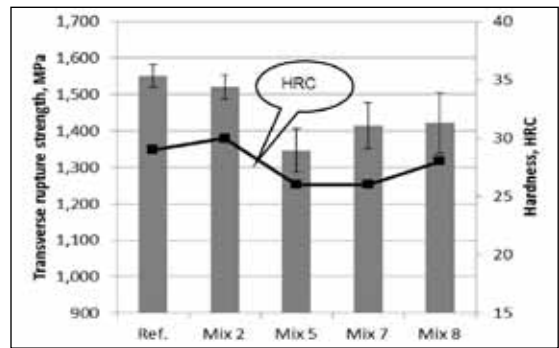


Fig.4 Transverse rupture strength and hardness of the materials containing experimental additive compared to the reference without additive: sinter-hardened materials

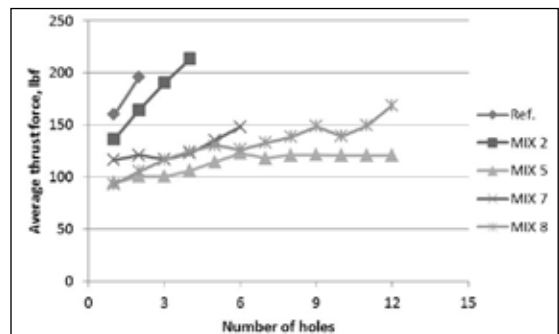


Fig.5 Drilling machinability of the materials containing select additive formulations compared to the reference without additive: sinter hardened materials

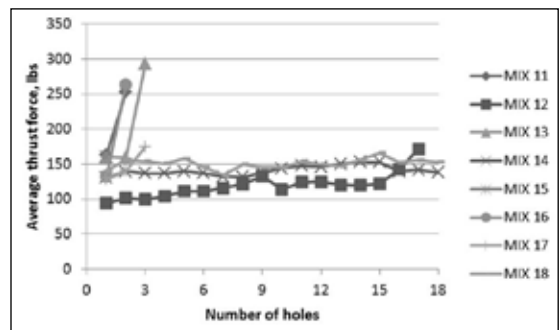


Fig.6 Drilling machinability of the materials containing the second series of experimental additives

MACHINABILITY OF SINTER-HARDENING PM MATERIALS WITH EXPERIMENTAL MACHINING ENHANCERS

In the next step, the materials containing machining enhancers of mixes 8 and 14 (ME 8 and ME 14) were tested for tensile and fatigue properties and the results were compared to the materials without additive and with 0.5% MnS. Ultimate tensile strength was lower for all materials containing machining enhancers compared to the reference, as shown in Fig. 7, while the material with ME 8 showed the lowest decrease of 9%. Yield strength also decreased slightly for the materials containing machining additives. Fig. 8 presents the dimensional change from die size of different FLC-4608 materials. DC was measured on TRS samples compacted to 7.0 g/cm³ density and sintered for fatigue testing from each material. All machining additives caused growth in FLC-4608 specimens compared to the reference without additive.

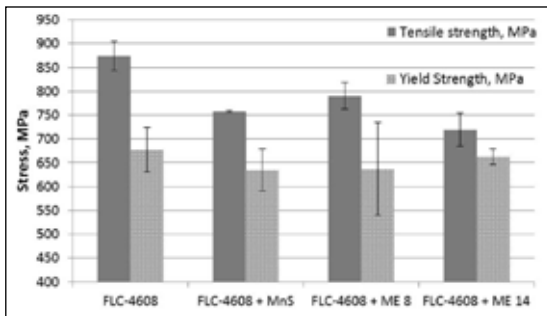


Fig.7 Ultimate tensile strength and yield strength of FLC-4608 materials with different machining enhancers

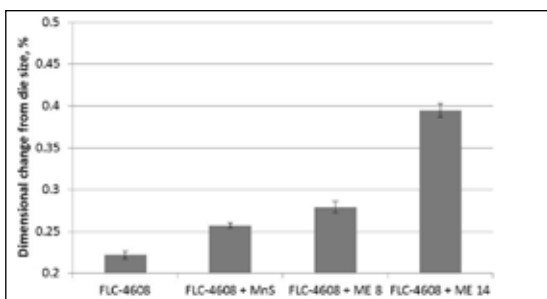


Fig.8 Dimensional change from die size of FLC-4608 materials with different machining enhancers

The results of bending fatigue test performed on TRS bars from materials with no additive, MnS, ME 8 and ME 14 are shown in Fig. 9. The reference material and the one containing MnS showed similar fatigue strength values, 418 and 414 MPa, respectively. The material containing ME 8 showed a 7% lower fatigue strength compared to the reference, 390 MPa, while the material with ME 14 had the lowest fatigue strength of 347 MPa, 17% below the reference.

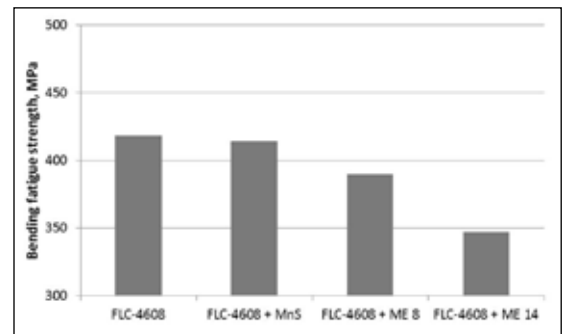


Fig.9 Bending fatigue strength of FLC-4608 materials with different machining enhancers: maximum stress at 50% survival rate, loading ratio of 0.1

Fig. 10 shows the variation of the average thrust force as a function of number of holes drilled for different FLC-4608 materials. As shown, the tool broke after two holes for the reference material and after 4 holes for the material containing MnS. Therefore, MnS was not efficient to improve the machinability of the evaluated sinter-hardening material. Machinability improved significantly with the use of both select machining enhancers with ME 14 being more efficient in general. The thrust forces were firstly lower for ME 8 containing material compared to ME 14 but increased rapidly after a certain number of holes. The slopes of average thrust force versus number of holes curves for different materials are also compared in Fig. 11. The slope values were 40 and 36 lbf/hole for the materials without

MACHINABILITY OF SINTER-HARDENING PM MATERIALS WITH EXPERIMENTAL MACHINING ENHANCERS

additive and with MnS showing a very short tool life for these materials. The slope was significantly lower for the materials containing both select machining enhancers and ME 14 could potentially provide longer tool life compared to ME 8. The microstructure of different sinter-hardened FLC-4608 materials is shown in Fig. 12. These microstructures were taken from the center of TRS bars where the effective cooling rate was the lowest and the difference in the evaluated materials could be better seen. For all materials, the microstructure was composed of tempered martensite and bainite. A higher proportion of martensite to bainite is seen for the reference material without additive and the one with MnS compared to the materials with select experimental additives. This is in accordance with the higher hardness of these materials presented in the parentheses. The material with ME 14 was composed of martensite and bainite with some retained austenite.

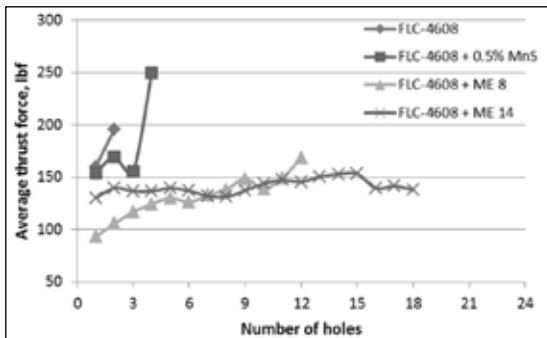


Fig.10 Drilling machinability in terms of average thrust force of FLC-4608 materials with different machining enhancers

Conclusion

The new experimental machining enhancers ME 8 and ME 14 improved the drilling machinability of sinter-hardened FLC-4608 material while MnS was not an effective enhancer for this system. ME 8 had less

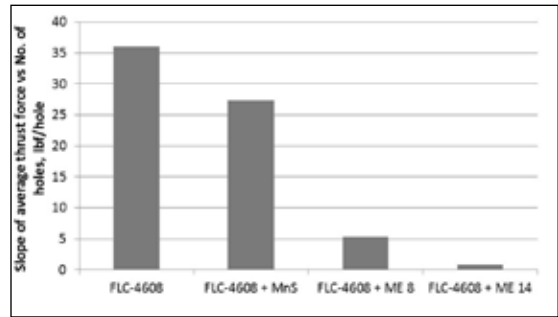


Fig.11 Slope of average thrust force versus number of holes for different FLC-4608 materials

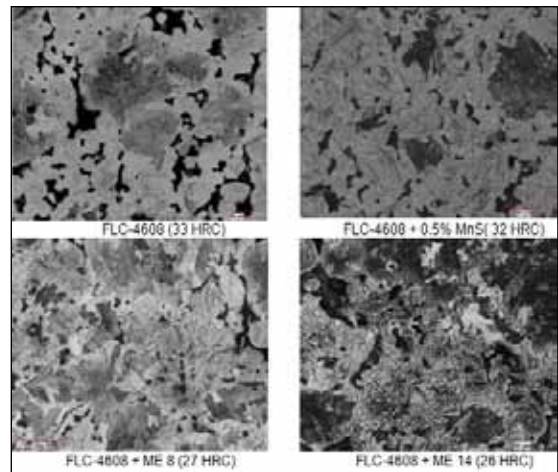


Fig.12 Microstructure of different sinter-hardened FLC-4608 materials: center of 1/2" TRS bars; hardness values in parentheses

negative effect on the mechanical properties of FLC-4608 compared to ME 14, while the latter showed better machining performance. Accelerated cooling also reduced the negative effect of machining enhancers on the sintered properties. Further evaluation of the machining performance of these new experimental enhancers should be done by performing turning test to validate their improving effect on the machinability of FLC-4608 material as this study was limited to drilling of certain number of holes for each material.

Acknowledgment

The authors would like to gratefully acknowledge Ian Bailon-Poujol and Chantal Labrecque for their valuable assistance throughout the preparation of this paper.

References

1. A.Salak et al., "Machinability of Powder Metallurgy Steels", 1st ed., Cambridge IntSci Publishing,(2005).
2. P.K.Wrighth and E.M. Trent, "Metal Cutting", 4th ed., Butterworth-Heinemann Publishing, (2000).
3. R.J. Causton and T.Cimino, "Machinability of P/M Steels", pp. 673 - 676, ASM Handbook Volume 7: Powder Metal Technologies and Applications, ASM International, Materials Park, OH, (2002).
4. H.A. Rodrigues et al., " Machinability of P/M Parts - Effect of Machining Additives and Processing", *Proceed. PM2010 Powder Metallurgy World Congress*, Florence, Italy, 10-14 October (2010).
5. F. Chagnon, "Effect of Machining Enhancer Additions on Static and Dynamic Properties of PM Materials", *Advances in Powder Metallurgy & Particulate Materials*, (2010).
6. O. Andersson and B. Hu, "Machinability improving composition", US patent No. US8795407, 2014.
7. F. Chagnon, "Effect of Machining Enhancer Additions on Static and Dynamic Properties of FD-0405 and FD-0408 Materials", *Euro PM2007 Congress Proceedings*, Copenhagen, Denmark, 12-14 October (2010).

SYNTHESIS AND APPLICATION OF $\text{CsSnBr}_x\text{I}_{3-x}$ AS A SOLID STATE HOLE TRANSPORT MATERIAL IN DYE SENSITIZED SOLAR CELLS.

Lekha Peedikakkandy¹, Parag Bhargava²

¹Centre for Research in Nanotechnology and Science

²Department of Metallurgical Engineering and Materials Science Indian Institute of Technology, Bombay.

Abstract

Mixed halides of p-type semiconducting perovskite, $\text{CsSnBr}_x\text{I}_{3-x}$ was prepared using solid state and solution route methods. Different characterisation techniques were used to investigate the opto-electronic properties of the prepared mixed halide perovskite. XRD and EDS analysis shows phase formation and phase transitions at room temperature. Optical analysis shows a shift in band edge emission and band gap values, from (1.3 eV) for CsSnI_3 to (1.5eV) for CsSnBr_2I . I-V characteristics of DSSC using pristine CsSnBr_2I and CsSnI_3 as HTM shows a conversion efficiency of 0.5% and 1.5% respectively. Based on XRD and EDS analysis it was found that mixed halides exhibits better stability and can be used as a solid state HTM for opto-electronic devices.

Keywords: Inorganic Perovskite, CsSnBr_2I , DSSC, Hole Conductor.

Introduction

The class of perovskites (CsSnX_3 , X=Cl, Br or I) exhibits a range of interesting physical properties. They exhibit strong luminescence in red and near-infrared regions of electromagnetic spectrum [1-3]. CsSnI_3 and CsSnBr_3 show high electrical conductivity at room temperature and have been used in solar cells as hole conducting materials. CsSnI_3 has a band gap of 1.3 eV and CsSnBr_3 has a reported band gap of 1.8 eV [4,5]. The high p-type electrical conductivity at room temperature for CsSnBr_3 and CsSnI_3 is explained as follows: the 4d unoccupied sites of Br- and I- overlap with the $5s^2$ state of Sn^{2+} leading to high metal like conductivity at room temperature [6-7].

Dye Sensitized Solar Cell (DSSC) is a cheaper alternate for the conventional semiconductor solar cells, but use of corrosive liquid electrolyte remain a challenge to overcome in commercialising DSSC [6]. To solve this problem and make DSSCs commercially viable several solid and semi-solid hole transport materials were used instead of corrosive

liquid electrolytes. Kanatzidis et al replaced the liquid electrolyte inorganic CsSnI_3 as a solid hole transport layer, with cell conversion efficiencies up to 10.2% [5]. The solubility of inorganic CsSnX_3 in organic solvents makes it easily penetrable in to the titanium oxide pores. In this study we synthesized and characterized mixed halide CsSnBr_2I for its application as an HTM for DSSC.

Experimental

Synthesis and Characterization

To synthesize $\text{CsSnBr}_x\text{I}_{3-x}$, stoichiometric mixture of CsI (99.9%, Sigma-Aldrich) and SnI_2 (99.9%, Sigma-Aldrich) and SnBr_2 (99.4%, Alfa Aesar) was mixed together under inert conditions of a N₂ Glove-Box. Mixed powder precursors were sealed in a quartz glass tube which was evacuated at 10^{-6} Torr vacuum. The sealed glass tube was annealed at 550°C for 30 minutes followed by cooling down to room temperature in 6 hours. The precursors melt to form a shiny black to Reddish-Brown ingots, which was taken out by breaking the glass tube, the ingot was ground into powder

SYNTHESIS AND APPLICATION OF $\text{CsSnBr}_x\text{I}_{3-x}$ AS A SOLID STATE HOLE TRANSPORT MATERIAL IN DYE SENSITIZED SOLAR CELLS.

using mortar and pestle. CsSnI_3 was also synthesized using dissolving stoichiometric composition of CsI and SnI_2 in DMF. Structure and composition of prepared materials were studied using X-Ray diffraction (XRD), Raman Spectroscopy and Energy-dispersive X-ray spectroscopy (EDS) scanning electron microscopy (SEM) and transmission electron microscopy (TEM). Band gap of the material was estimated from the diffuse reflectance spectroscopy using Kubelka-Munk equation. Photoluminescence (PL) spectra were measured at 514nm excitation wavelength.

Preparation of Dye Sensitized Solar Cells (DSSC) with CsSnI_3 as HTM

Synthesized $\text{CsSnBr}_x\text{I}_{3-x}$ and CsSnI_3 were used as a hole transport layer replacing the liquid iodine/tri-iodide redox couple in DSSCs. For this, fluorine doped tin oxide (FTO ~10 Ω /square) substrates were cleaned by ultrasonication in soap solution, distilled water and iso-propyl alcohol respectively and was dried in hot air oven. Titania paste (P20, Dyesol) was doctor bladed on to the FTO substrates and annealed at 500°C for one hour. Titania photo-anodes were dipped in 0.3mM ethanolic solution of dye, cis-bis(4,4'-dicarboxy-2,2'-bipyridine)-bis(isothiocyanato)ruthenium(II) (N3 dye, Solaronix) for 12 hours. Pt sputter coated on to the FTO glass substrate was used as counter electrode. Sensitized photo anode and Pt coated counter electrode was assembled with a spacer of 60-micrometer thickness. A saturated solution of $\text{CsSnBr}_x\text{I}_{3-x}$ and CsSnI_3 in a 1ml mixture of methoxyacetonitrile (MeAc), dimethylformamide (DMF) and acetonitrile (ACN) in a 1:3:2 volumetric proportion) and was used to infiltrate the porous titania layer. HTM solution was injected into the cell using a micropipette; cells were dried overnight inside the glove-box to remove the solvents. I-V characteristics of cells (area 0.25 cm^2) were measured under sun.

Results and Discussion

CsSnBr_2I crystals grown through solid state reaction route were reddish-brown in colour, as shown in Fig.1(a). Fig.1(b) shows XRD analysis of as prepared crystals of CsSnBr_2I .

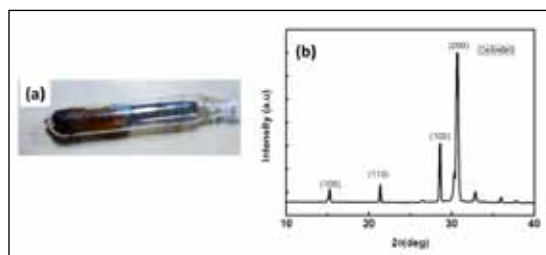


Fig.1 (a) CsSnBr_2I prepared through solid state reaction route. (b) XRD of CsSnBr_2I prepared through solid state route.

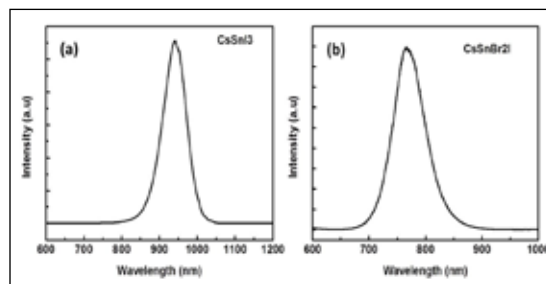


Fig.2 (a) Emission spectra of CsSnI_3 and (b) Emission spectra of CsSnBr_2I at room temperature.

Both CsSnI_3 and CsSnBr_2I show strong PL at room temperature with an emission maxima at 950 nm and 780nm as shown in Fig.2.(a) and (b) respectively. It was observed from the PL study that as the iodide is being replaced with bromide ion in CsSnI_3 the band gap of the material increases from 1.3 eV to 1.57 eV for CsSnBr_2I . The band gap for CsSnBr_2I was also estimated to be 1.57eV from band edge emission and Kubelka-Munk conversion of reflectance spectra. Fig.3 shows the SEM image of CsSnBr_2I recrystallized from electrolyte mixture.

SYNTHESIS AND APPLICATION OF CsSnBr_3 AS A SOLID STATE HOLE TRANSPORT MATERIAL IN DYE SENSITIZED SOLAR CELLS.

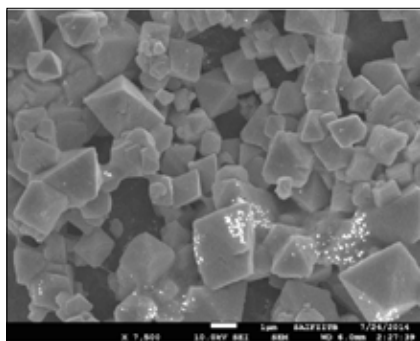


Fig. 3 SEM image of CsSnBr_2I recrystallized from mixture of solvents ACN:MeAc:DMF.

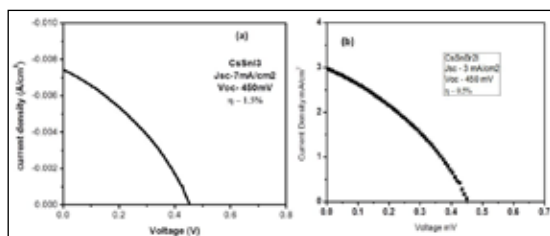


Fig.4 (a) I-V characteristics of CsSnBr_3 as HTM and (b) I-V of CsSnBr_2I as HTM in DSSC.

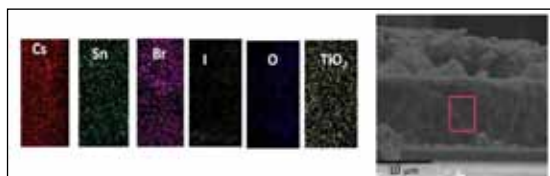


Fig.5. Cross-sectional SEM and elemental mapping image of DSSC with CsSnBr_2I as HTM.

Fig.4.a and b compares the photovoltaic performance between CsSnBr_3 and CsSnBr_2I as HTM in DSSC. Fig.5 shows the cross-sectional SEM and elemental mapping of DSSC with CsSnBr_2I as HTM. The cross-sectional elemental mapping shows that CsSnBr_2I has permeated through the titania matrix and recrystallized in stoichiometric ratio.

Conclusion

The results from XRD and optical characterisation studies confirm formation of CsSnBr_2I mixed halide perovskite. DSSCs assembled with CsSnBr_2I HTM showed a

photovoltaic conversion efficiency of 0.5% while a similar cell with CsSnBr_3 HTM layer showed an efficiency of 1.5%. To conclude, optical properties and semi-metallic properties of cesium tin tri-halides can find application as an absorber and as a hole transport material in solar cells as well as other opto-electronic devices.

Acknowledgments

The authors acknowledge financial support from the Department of Science and Technology of India and the Solar Energy Research Institute for India and the United States (SERIUS) and SAIF (IIT-B) for SEM images of crystals.

References:

1. D. E.Scaife, P. W. Weller, W.G. Fisher, "Crystal preparation and properties of cesium tin (II) trihalides", *J. Solid. State. Chem.*, 9,308-314, (1974).
2. K. Yamada, S. Funabiki, H. Horimoto, T. Matsui, T. Okuda, S. Ichiba, "Structural phase transitions of the polymorphs of CsSnBr_3 by means of Rietveld analysis of the x-ray diffraction", *Chem. Lett.*, 20, 801-804, (1991).
3. K. Yamada, T. Matsui, T. Tsuritani, T. Okuda and S. Ichiba, " ^{127}I -NQR, ^{119}Sn Mössbauer effect and electrical conductivity of MSnBr_3 (M = K, NH_4 , Rb, Cs and CH_3NH_3)", *Z. Naturforsch. A Phys. Sci.*, 45, 307-312, (1990).
4. I. Chung, J.H. Song, J. Im, J. Androulakis, C.D. Malliakas, H. Li, A.J. Freeman, J. T. Kenney, M. G. Kanatzidis, " CsSnBr_3 : Semiconductor or metal? High electrical conductivity and strong near-infrared photoluminescence from a single material. High hole mobility and phase-transitions", *J. Am. Chem. Soc.*, 134, 8579-8587, (2012).
5. I. Chung, B. H. Lee, J. Q. He, R. P. H. Chang, and M. G. Kanatzidis, "All-solid-state dye-sensitized solar cells with high efficiency", *Nature*, 2012, 486-489, (2012).
6. Z. Chen, J.J. Wang, Y. Ren, C. Yu, K. Shum, "Schottky solar cells based on CsSnBr_3 thin films", *Appl. Phys. Lett.*, 101, 093901, (2012).
7. M. Grätzel, "Photoelectrochemical cells", *Nature*, 414, 338-344, (2001).

SALT ASSISTED SYNTHESIS OF NANO ZIRCONIA

Divya P, P Bhargava

Metallurgical Engineering and Materials Science Department, Indian Institute of Technology Bombay, Powai, Mumbai.

Abstract

The synthesis of nanoparticles has been researched successfully in the last two decades and numerous methods for making of nanoparticles of zirconia have been reported. However the challenge in the making of nanoparticles is to retain the individual particles in an unagglomerated state. It is now well understood that nanoparticles have a tendency to form agglomerates due to their high surface energy. Agglomerated nanoparticles do not allow good densification during the sintering process. In the present work, zirconia nanoparticles were synthesized in the presence of salt (NaCl), and it was found that the presence of this salt helped in reducing the agglomeration. The powders obtained were characterized using X-Ray diffraction, Scanning Electron Microscopy, Transmission Electron Microscope, Thermogravimetric analysis, Dynamic Laser Scattering (DLS) Particle size measurement and Brunauer–Emmett–Teller (BET) surface area.

Keywords: zirconia, nanoparticles, deagglomeration

Introduction

In the last three decades, significant research on ZrO₂ based ceramics has been carried out due to it being used for numerous applications like cutting tools, milling media, solid oxide fuel cells, hip joint prosthesis and prosthodontics. It is being used for such variety of applications due to its high hardness, toughness and biocompatibility [1]. Since the last decade focus has been on producing nanoparticles of zirconia and a lot of researchers have been successful in doing so. There is a lot of literature that discusses various methods used in making of nanoparticles, however there is also a well accepted concern about agglomeration of the nanoparticles. The benefits of obtaining a very fine particle size are not achieved until the agglomeration of the particle is eliminated or minimized. This is because agglomerates do not sinter well and thus densification is not fully achieved.

Powders that have submicron or finer sized particles have a strong tendency for adhesion due to Van der Waals forces especially when the ambient humidity is lesser than a critical

relative humidity. Under conditions where the humidity is higher, it has been stated that capillary forces are responsible for the adhesion of particles due to the presence of condensed water in the contact areas between particles. In agglomerates, the forces that keep the particles adhered to each other are more often stronger than forces that are applied to cause their detachment. These detaching forces may be incidental during an application or may be applied mechanically with an intent to break down the particles [2]. Hence efforts should focus on preventing the formation of agglomerates or at least to minimize it to the best possible extent. It is known that for applications and technologies involving compaction and sintering, the preferred particles should be spherical, unagglomerated and have a narrow size distribution. Many researchers have been successful in synthesizing Yttria Stabilized Zirconia (YSZ) using various processes like sol-gel, hydrothermal processes, inert gas condensation using thermal evaporation and co-precipitation [3,4,5]. However disadvantages like long reaction time and low concentration of reacting species make

SALT ASSISTED SYNTHESIS OF NANO ZIRCONIA

them commercially unviable. Any process to be industrially relevant, needs to be low cost, be amenable for continuous operation and should have a high production rate.

The presence of a salt in the precursor solution is reported to help in producing deagglomerated nanoparticles. Typically, as part of the process the salt containing precursor solution is sprayed into fine droplets. Each of the droplets when calcined contains large number of nanoparticles within it, held together by the salt present. When these dried droplets are washed with water, the salts gets washed away and it must yield separated nanoparticles [6]. In the present work this concept formed the basis of our experiment.

Experimental work

Zirconium oxychloride ($ZrOCl_2 \cdot 8H_2O$) and yttrium nitrate hexahydrate ($Y(NO_3)_3 \cdot 6H_2O$) were used as the precursors to synthesize 3YSZ. A solution was prepared by mixing $ZrOCl_2 \cdot 8H_2O$ and $Y(NO_3)_3 \cdot 6H_2O$ in distilled water. In this solution, NaCl (5wt% of precursor) was added and then magnetic stirring of this mixed solution was done for 2 hours. Afterwards the solution was sprayed on an alumina tray kept on a heater. The spraying was done using a plastic spray bottle and it was expected that the sprayed droplet size must be around several 100 micrometers and even approaching a mm. The temperature of the tray was measured using a thermocouple and during the spraying it was maintained around $130^\circ C$. The powders thus formed were kept in an oven at $100^\circ C$ for 24 hours for complete drying. The powders were then divided into two batches. One of the batches was calcined at $600^\circ C$ and the other one was calcined at $900^\circ C$ for 1 hour each.

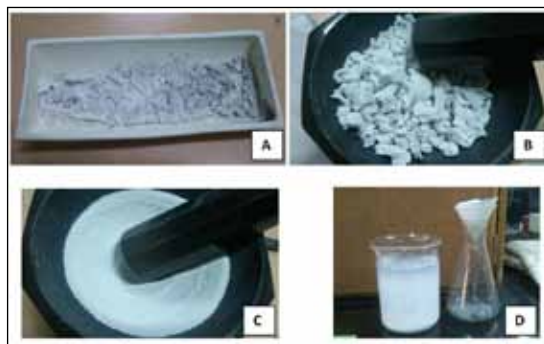


Fig. 1(A) 3YSZ powders on alumina plate after calcination (B) Calcined powders in pestle-mortar (C) Powders after grinding and (D) Filtering of powders after washing

3YSZ is known to crystallize around $470^\circ C$ [7] and hence temperatures higher than $470^\circ C$ were chosen for calcinations. Higher calcination temperature was chosen based on experience of obtaining particle size in a range which has lower agglomeration tendency. After calcinations, the respective powders were washed with distilled water and filtered and dried again in an oven. The powders obtained were finally ground using a mortar pestle. The characterization of all these washed and also unwashed powders was done using DLS, X-Ray Diffraction (XRD), SEM and TEM. The specific surface area of the particles was measured by gas sorptometer (nitrogen adsorption) using Brunauer-Emmett-Teller (BET). The obtained powders were subsequently pressed into pellets on a Universal Testing Machine at 200MPa peak pressure. The pellets were sintered at $1400^\circ C$. The XRD patterns were obtained by PAN analytical Instrument with Cu-K α radiation having a wavelength of 1.54 \AA . The analysis of the results was done on Xpert highscore software.

Results and Discussion

The thermogravimetric analysis of the as sprayed and dried powders indicated a weight

loss of approximately 37% on heating from room temperature upto 520°C. On heating further a little reduction of 8% was found upto 1200°C. This can be seen in Fig.2. This cumulative weight loss of 45% has been due to the decomposition of $ZrOCl_2 \cdot 8H_2O$ and $Y(NO_3)_3 \cdot 6H_2O$.

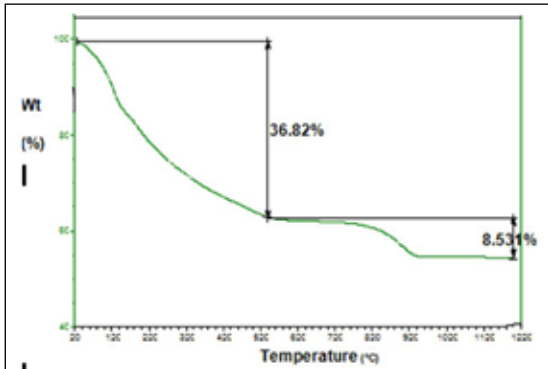


Fig. 2 TGA of as sprayed and dried powders

The Differential Scanning Calorimetry (DSC) of the as sprayed and dried powders indicates the formation of crystalline phases at a temperature of 483°C, seen in fig 3, as an exothermic peak.

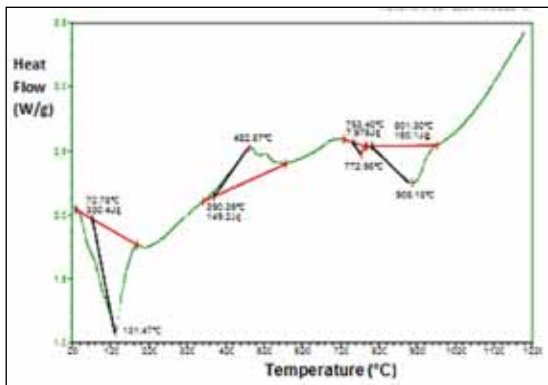


Fig. 3 DSC of as sprayed and dried powders

The as sprayed and dried powders had an amorphous structure, as seen in the XRD pattern in Fig 4.

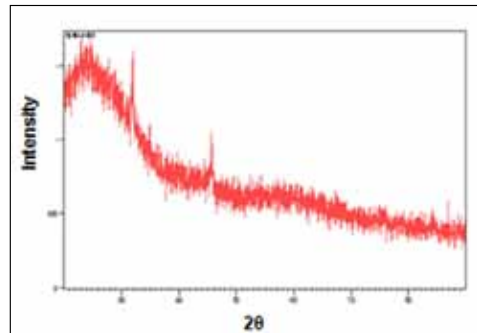


Fig. 4 XRD of as sprayed and dried powders

Peaks were observed after calcination only, indicating the formation of new crystalline phases occurred only post calcination and definitely not during the spray or drying step. This is because the temperatures were never higher than 150°C during spraying and this low temperature did not allow for the nucleation of the crystalline phases. Peaks of tetragonal zirconia were found after calcinations as can be seen in the XRD results in figs.5a and 6a.

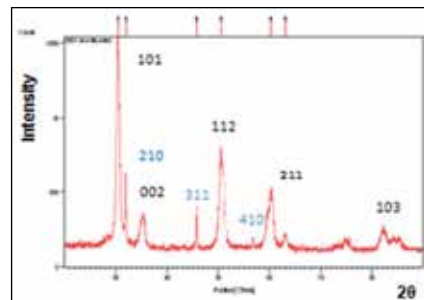


Fig. 5a: XRD of 600°C calcined unwashed powders

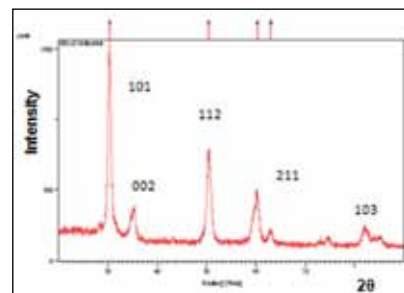


Fig. 5b: XRD of 600°C calcined and washed powders

SALT ASSISTED SYNTHESIS OF NANO ZIRCONIA

*black coloured indices are of tetragonal YSZ, blue coloured indices are of Sodium chlorate

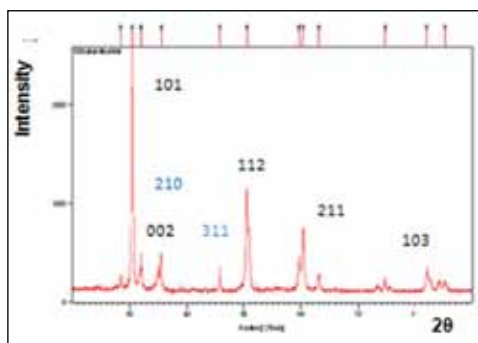


Fig. 6a: XRD of 900°C calcined unwashed powders

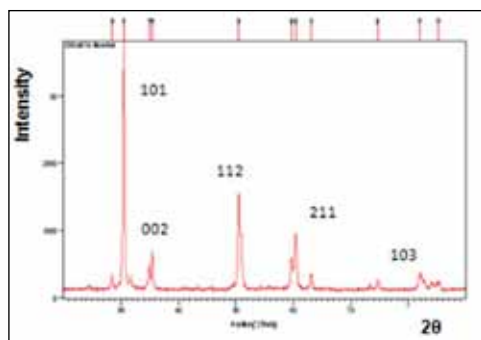


Fig. 6b: XRD of 900°C calcined and washed powders

The Figs.5a and 6a showed the presence of sodium chlorate in the calcined unwashed powders. The calcined and washed powders did not reveal the peaks of sodium chlorate as can be seen in Fig. 5b and 6b. Sodium Chlorate dissolves in water and therefore was eliminated on washing. These results indicated the presence of the salt during the synthesis of YSZ and its removal during the washing sequence. This was confirmed by the XRD results.

The FEGSEM images for the powders produced by spraying and drying showed their morphology to be acicular, flaky and in the form of ribbons. A similar observation was

also found for the powders that were calcined at 600°C and also 900°C. (Fig.7, 8a and 10a).

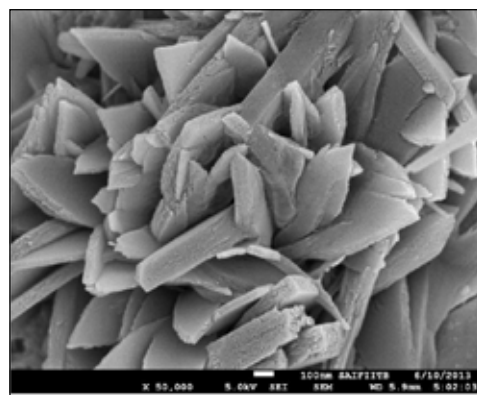


Fig.7: FEG SEM of as sprayed and dried powders

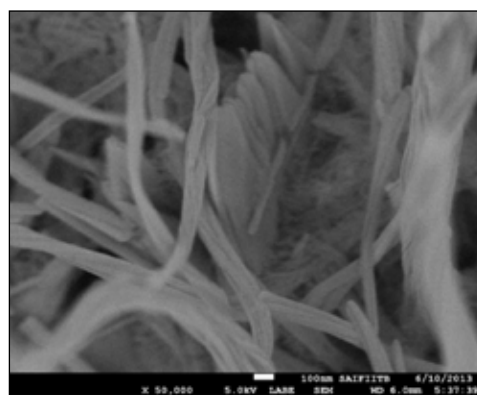


Fig. 8a FEG SEM of 600°C calcined unwashed

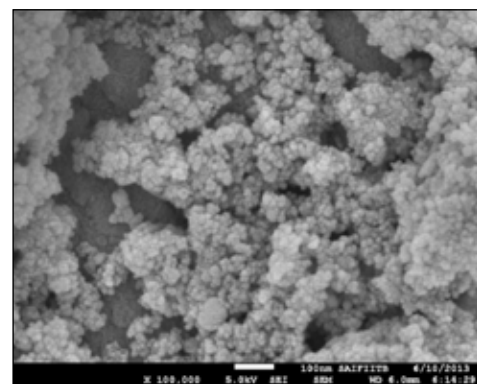


Fig. 8b FEG SEM of 600°C calcined and washed powders

On washing the flaky acicular layers appeared to have disintegrated and revealed the presence of nanoparticles. The salt acted as an additive and had kept the particles bound in layers of flakes. This can be seen in figs 8b and 10b. The TEM showed powder that was calcined at 600°C, with individual particles appearing to be of size approximately 100nm, as seen in fig 9a. These calcined powders after washing show a much smaller particle size of approximately 30-40 nm seen in fig 9b.

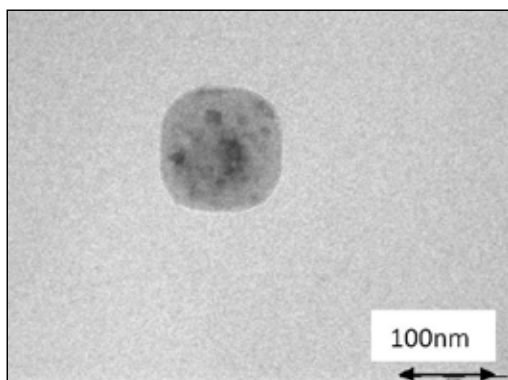


Fig. 9a TEM of 600°C calcined unwashed powders

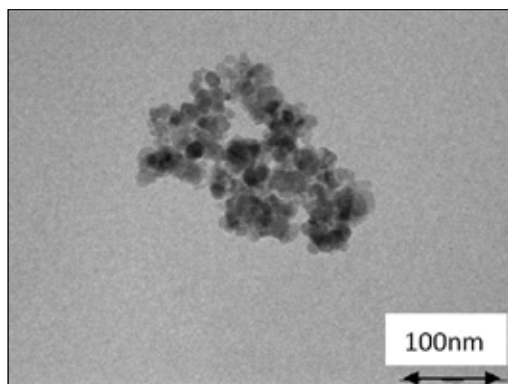


Fig. 9b TEM of 600°C calcined and washed powders

The powders which were calcined at 900°C also were in the form of ribbons and platelets, however on washing they disintegrated to reveal smaller particles. This can be seen in figs. 10a and 10b

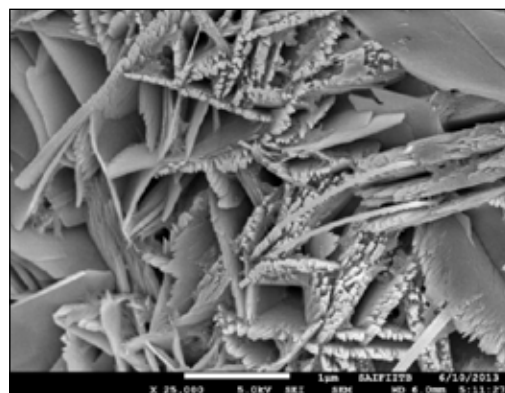


Fig. 10a: FEGSEM of 900°C calcined unwashed

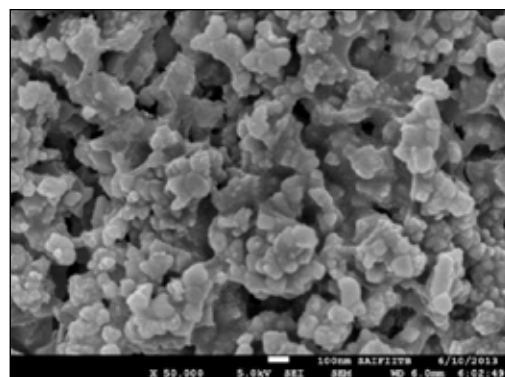


Fig. 10b: SEM of 900°C calcined and washed powders

The powders obtained on washing of 600°C calcined powders are extremely fine but lightly agglomerated. Whereas the washed powders of 900°C calcined samples show that the particles have fused together. This is highly probable because the melting point of NaCl is 801°C.

The reduction in the particle size after washing of the powders was also ascertained from the DLS particle size measurements. A reduction of 68% was seen in the washed powders calcined at 600°C. The extent of reduction in the powders calcined at 900°C and those that were washed subsequently was 25%. The results are shown in Table 1.

SALT ASSISTED SYNTHESIS OF NANO ZIRCONIA

Table 2. Surface area of the 3YSZ powders synthesised

3YSZ powders	As sprayed and dried	600°C calcined unwashed	600°C calcined and washed	900°C calcined unwashed	900°C calcined and washed
Particle size(nm)	490	4196	1351	2161	1631

The BET specific surface area of the powders was in complete agreement to the findings from FESEM, TEM and DLS and have been shown in Table.2.

Table 2. Surface area of the 3YSZ powders synthesised

3YSZ powders	As produced	600°C calcined unwashed	600°C calcined and washed	900°C calcined Unwashed	900°C calcined and washed
Surface area(m ² /g)	---	22.79	37.67	3.09	6.62

Pellets that were prepared under compaction pressure of 200 MPa and sintered as per the sintering cycle shown below was found to have sintered density of 75%.The shrinkages both radial and linear was also calculated and have been shown in Table.3

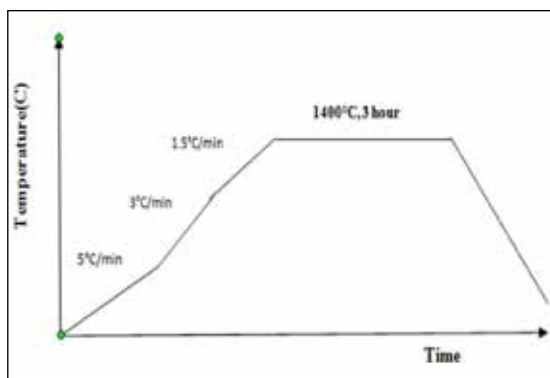


Fig. 11 Sintering cycle used for 3YSZ powders

Table 3. Density and shrinkage of the 3YSZ pellets

Sample condition	Green density(gm/cc)	Sintered Density(gm/cc)	Linear shrinkage%	Radial shrinkage%
1,600°C calcined and washed	2.85	4.01	9.7	5.74
2,900°C calcined and washed	3.04	4.49	12.77	14.62

Conclusions

The characterisation of the synthesised, calcined and washed powders clearly indicated that the inclusion of a soluble salt like NaCl helped in the synthesis of nanoparticles that were partially deagglomerated. The surface area of the powders were calcined at 600°C and washed with water was 37.67m²/g. The washing sequence that was followed in this study was simple and in a single step, which was probably a reason for not having achieved near 100% sintered density. After washing in water, there was an obvious decrease in the particle size which confirmed the role of salt during the synthesis. It was keeping the smaller particles together in a larger network and on washing and filtering the salt was eliminated. The optimised calcination temperature for this system is 600°C. The choice of calcination temperature in this process must be made in reference to the salt characteristics. The process using salt for achieving deagglomerated nanoparticles has potential of becoming a preferred process if appropriate salts are identified and the calcination treatments are chosen appropriately. Overall the process is extremely simple and can be applied without use of sophisticated equipment.

Acknowledgements

The authors wish to acknowledge the Sophisticated Analytical and Instrumentation facility, IIT Bombay and XRay Diffraction Laboratory, IIT Bombay for helping with the characterization. The author also expresses her gratitude to Mr. Ritwik Goyal and is thankful to all colleagues in the Particulate Materials Laboratory, IIT Bombay for all the support provided during this research work.

References

1. I. Birkby, R.Stevens, "Applications of zirconia ceramics", *Key Engineering Materials*, 122-124, 527-552, (1996).
2. J. A. Kurkela , D. P. Brown , J Raula, E I. Kauppinen, "New apparatus for studying powder deagglomeration", *Powder Technology*, 180, 164-171, (2008).
3. T. Omata, Y. Goto, S. Otsuka, "Nanocrystals of zirconia- and ceria-based solid electrolytes:Syntheses and properties", *Sci. Tech. Adv. Mat.*, 8, 524-530, (2007).
4. F. Kazemi, A. Saberi, S. Malekhamadi, S. Sohrabi, H.R Rezaie, M. Tahiriri, "A novel method for synthesis of metastable tetragonal zirconia nanopowders at low temperatures", *Ceramics*, 55 (1), 26-30, (2011).
5. R. Dwivedi, A. Maurya, A. Verma, R. Prasad, K.S. Bartwal, "Microwave assisted sol-gel synthesis of tetragonal zirconia nanoparticles", *J. Alloys Comp.*, 509, 6848-6851, (2011).
6. B.Xia , I.W. Lenggoro K. Okuyama, "Novel Route to Nanoparticle Synthesis by Salt-Assisted Aerosol Decomposition", *Adv. Mat.*, 13, 1579-1582, (2001).
7. S.B.Patil, P.Bhargava, "Characterization of agglomeration state in nanocrystalline 3YSZ powders through pressure-displacement curves and nanoindentation of green compacts", *Powder Technology*, 228, 272-276, (2012).

CORRELATION OF FAILURE MODES OF ZINC OXIDE VARISTORS WITH THEIR MICROSTRUCTURES

S. Saravanan, J. Nemade

CG Global R&D Center, Crompton Greaves Ltd. Mumbai - 400042, India

Abstract

High voltage equipment, such as surge arrestor, circuit breakers, instrument transformer, power transformer etc. are expected to operate fault-free, otherwise that can cause financial damages. In this sense, the technology of surge arresters has sought to produce varistors showing high electrothermal performance. ZnO varistor ceramics are polycrystalline semiconducting multi-component, with minor amounts of added oxides that play important roles, both in the tremendous non-linear electrical characteristic and for the control of microstructure. High voltage ZnO varistor disc fabricated through conventional ceramic powder metallurgy route. Grain size distribution, microstructural homogeneity and grain boundary plays the major role to control the electrical properties of the varistor. High voltage varistors can fail due to a large capacity to absorb energy because of lightning strikes, switching transients and similar disturbances. Ineffective microstructure leads to puncture and cracking failure due to high temperature and thermal stress when injecting impulse current in varistor. Major causes of failure modes such as puncture and cracking analyzed through microstructure characterization. The paper presents the correlation between grain size distribution, nature of grain boundary and phases present in the microstructure of high voltage varistor with the distribution of current, temperature, and thermal stresses in the same as a function of failure modes.

Keywords: ZnO varistor, Failure analysis, Puncture, Cracking, Microstructural characterization

Introduction

ZnO varistors are widely used as function elements of surge arresters that protect electrical equipment and electronics from overvoltage caused by lightning and switching transients since 1970s [1-2]. The semiconducting polycrystalline material is well suited for circuit protection against impulse surges in power transmission and distribution facilities because of its excellent nonlinear characteristics, and very high current and energy absorption capabilities i.e. highly nonlinear conduction with voltage in combination with an extremely low leakage current at low electric fields. They can be used over wide ranges in rating from a few volts to 1200 kV according to their specific properties. The nonlinear characteristics come from nm thick grain boundary regions where a barrier to majority of carriers (electrons) exists in the

depletion layer of the ZnO grains. The negative surface charge at the grain boundary interface is compensated by the positive charge in the depletion layer in the grain on both sides of the interface. The major transport mechanisms are thermionic emission and tunnelling. [3]

In service, varistors can fail due to a large capacity to absorb energy because of lightning strikes, switching transients and similar disturbances. Therefore energy handling capability is important to circumvent the occasional failures [4]. The significant failure modes of varistor elements are thermal runaway, puncture and cracking. If the temperature rise caused by the Joule heating of leakage current is above the thermal stability temperature, power input may exceed heat dissipation, and thermal runaway occurs. Cracking and puncture are caused by a localization of the current, which causes

CORRELATION OF FAILURE MODES OF ZINC OXIDE VARISTORS WITH THEIR MICROSTRUCTURES

local heating leading to nonuniform thermal expansion and thermal stresses. In puncture, a small hole resulting from melting of the low melting ceramics where high current concentrated which leads to the great thermal stress in the ZnO ceramics. The cracking failure occurs if the thermal stress is higher than the failure stress of ZnO varistor. These failures caused by the ineffective microstructure such as irregularities of the grain boundary, grain size distribution and phases present in the microstructure of the varistor. The main purpose this paper is to analyze the major failure modes such as puncture and cracking of high voltage varistor through the evaluation of microstructure of the same.

Experimental procedure

This work was based on the production of 3.25 kV varistor discs used in class 3 lightning arresters with nominal green dimensions of 71 mm outer diameter, 26 mm inner diameter and 22.5 mm height. The samples were prepared with 96 mol% of ZnO and small amounts of additives: 0.5 mol% of Bi_2O_3 , 1 mol% of antimony oxide Sb_2O_3 , 0.5 mol% of CoO, 0.5 mol% of MnO_2 , 0.5 mol% of Cr_2O_3 , and 0.5 mol% of SiO_2 , by using conventional ceramic processing, i.e., ball milling, drying, calcination, disper milling, spray drying, mixing, pressing, sintering, and finishing. The additives were ball milled before and after calcination with zirconia balls at 77 RPM for 12 hrs to bring the particle size $\leq 5\mu$. The ball milled oxides mixed with ZnO and binder by disper milling. The suspension was simultaneously dried and granulated by the spray drying process. The pressing operation under pressure ranging from 120 to 210 kg.cm⁻² was performed in a double-action 3 stage pressing (1/3, 2/3 and full pressure) using 70 T hydraulic press. Pressure was reduced to normal after every 1/3 pressure stage to release the trapped air if any. After pressing, the green discs were

subjected into binder burnout at 390°C for 1 h and calcination at 890°C for 1.5 h. Calcined samples were collared by high resistive coating and sintered at 1170°C in air in an electric furnace using a conventional sintering profile and a total sintering cycle time of about 4 h. After complete firing, the varistor blocks flat surfaces were carefully machined then heat treated at 490°C for 1.5 h and both inferior and superior faces were metallized by Al spray to improve their electrical contact.

Considering the main purpose of this work two kind of pulses such as large pulses (2000 μ s) and short pulses (8/20 μ s) to distinguish the effect of current pulses in the microstructure and the failure caused by electrical discharge. The major failure such as puncture and cracking occurred in the long duration-impulse test and depending on the intensity and frequency of the pulses the developed stress may damage the varistor. Each long-duration impulse current test consisted of 18 impulses divided into six groups of three impulses of 250 A, and the intervals between impulses did not exceed 60 s. Before long-duration test the samples were tested in the residual voltage test, reference voltage test according to technical standards for surge arresters [5]. Current-voltage measurements were taken over a wide range of currents, and the value of the nonlinear coefficient (α) was obtained in the nonlinear region.

The crystalline phases were identified by an XRD with $\text{CuK}\alpha$ radiation. The density of varistor ceramics was measured by the geometrical method [6]. One of the surfaces of samples was lapped and ground with SiC paper and polished with 1 μ m diamond suspension to a mirror-like surface. The polished samples were chemically etched with acetic acid for 10 sec. The surface microstructure of the good and failed samples was examined by Scanning electron microscope (SEM). The grain size

CORRELATION OF FAILURE MODES OF ZINC OXIDE VARISTORS WITH THEIR MICROSTRUCTURES

distribution, type of dopants and their distribution were also examined by SEM with EDS. The average grain size was determined by lineal intercept method [7].

Results and discussion

The main intension of our study was to correlate the major failure modes with microstructure of ZnO varistor. Table 1 shows the basic properties of 3.25 kV few ZnO blocks except long-duration test.

Table.1. Basic properties of the ZnO varistor

Sample no	Green density	Sintered density	Residual Voltage kV/(8/20 μ s)at 10 kA	Reference voltage(kV) at V1mA DC	Volts/mm	Average Grain size(μ m)
1	3.17	5.44	8.1	4.1	179.353	12
2	3.18	5.45	8.2	4.1	179.510	12
3	3.17	5.41	7.8	4	174.444	13
4	3.15	5.46	8.0	4	175.439	13

Fig.1 shows the XRD pattern of ZnO Varistor polished samples after testing. It reveals diffraction peaks of ZnO (JCPDS No. 36-1451), Spinel phase and Bi rich phase. The normal and failed samples contain the same phases and no other impurities were present.

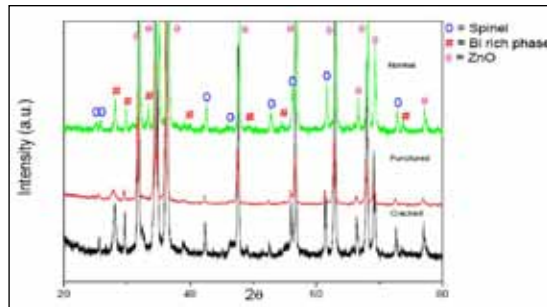


Fig.1. XRD patterns of the normal and failed ZnO Varistors

Fig.2 showed the SEM microstructure and Elementary composition analysis by EDS of normal ZnO Varistor after testing. The main constituents are ZnO, $Zn_7Sb_2O_{12}$ spinel and Bi_2O_3 -rich phases [8, 9, 10]. The average ZnO grains are 12-13 μ m and the grains differ a lot in geometry but are very similar with respect

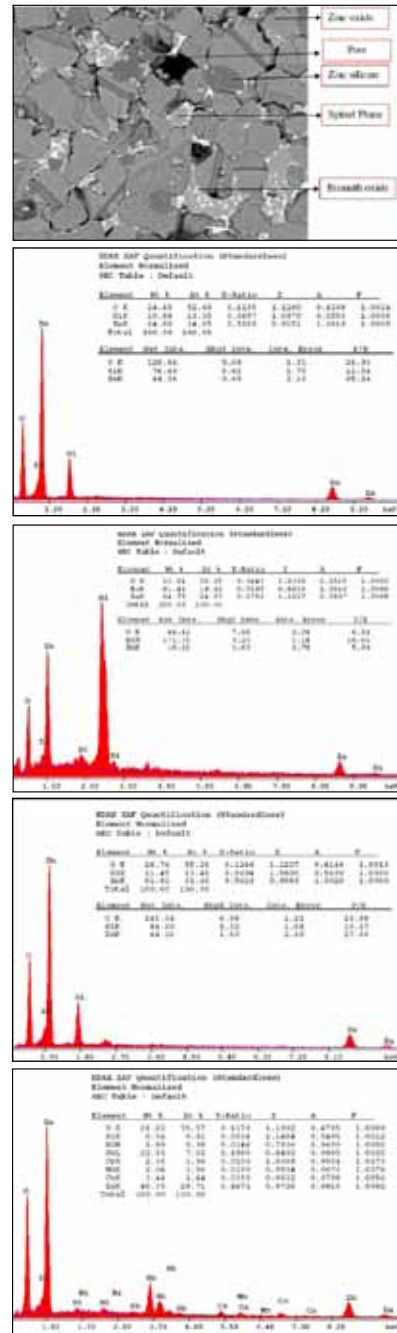
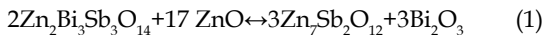


Fig.2. SEM micrograph of normal ZnO Varistors

CORRELATION OF FAILURE MODES OF ZINC OXIDE VARISTORS WITH THEIR MICROSTRUCTURES

to chemical composition. The grain size and distribution can be controlled by processing and also by different additives. In this present composition Sb and Si are used for grain growth suppression [11]. Small amounts of dopants Co and Mn are found in the ZnO grains. The spinel ($Zn_7Sb_2O_{12}$) grains are 2–4 μm in diameter and act, during the sintering process, as controller of grain growth by pinning the migrating ZnO grain boundaries. The spinel grains are present in Fig.1 as alone or in large clusters surrounded by Bi-rich phases but also inside ZnO grains. Spinel particles form during the early stages of sintering by reaction of ZnO with pyrochlore ($Zn_2Bi_3Sb_3O_{14}$) according to equation (1) [12],



Additives like Co, Mn and Cr promote the formation of spinel grains and also detected in the spinel grains [12, 13].

Long duration test has been carried out as per standard [5]. Total energy was injected to the ZnO varistor block. Totally 18 impulses divided into six groups were injected to the ZnO varistor blocks and the total energy 12.19 kJ have been dissipated per each shot at the interval of not exceed 60s. Few blocks failed by Puncture and cracking. Results indicate that the observed current concentration is related to the disorder in the microscopic scale (grain size scale) rather than to the macroscopic nonuniformities of varistor blocks. The current concentration phenomenon is very common in ZnO polycrystalline varistors and nonuniform current distribution to be an intrinsic feature of ZnO varistors. For high field applications, the microstructural requirements include homogeneous and uniform dopant distribution [14]. The current that can flow along the material is strongly affected by the microstructural disorder since the conductance of the surrounding regions changes. Thus, the

effect of microstructural disorder is especially pronounced when it is in direct electrical contact with the electrodes.

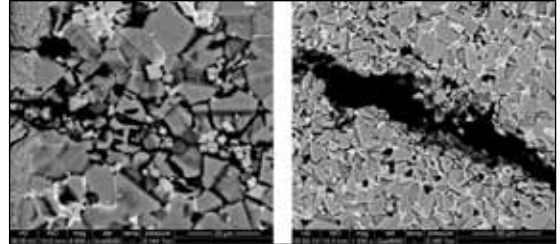


Fig.3. Microstructural disorder and cracking due to thermal distribution

Fig.3 shows the microstructural disorder and cracking after degradation due to thermal stress distribution. The ineffective grain boundary leads to fail due to current localization. Thermal stability of the ZnO varistor disks has been studied extensively [15, 16]. The microstructural inhomogeneities and large grains can cause current localization.

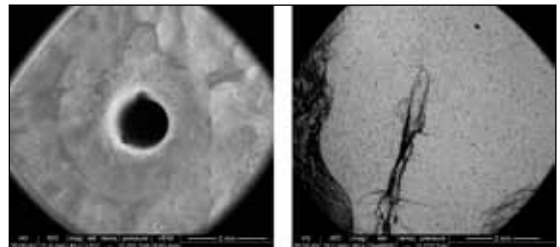


Fig.4. Top and cross section view of the puncture phenomenon

Fig.4 shows that the surface morphology of the puncture phenomenon. Micrographs indicate that there are only few grain paths carried most of the current within the voltage-sensitive region. The current distribution is related to the uniformities of grains, grain boundary and electrical characteristic of varistors. After the current is applied for 2ms, the temperature rise and distribute throughout the varistor body. Fig.4 indicate that the temperature

CORRELATION OF FAILURE MODES OF ZINC OXIDE VARISTORS WITH THEIR MICROSTRUCTURES

of the regions near the ceramic body where current is concentrated was much higher the else regions and penetrated from the top to the bottom. Jinliang He reported that the average temperature rise in this case was 153K, while the highest temperature rise reached 376K, the lowest temperature rise was only 22K [17]. If the temperature exceed 800 oC hot spot reaches, those regions in the ceramic body will be melted due to low melting oxides especially Bi_2O_3 , which leads to produce a puncture as shown in Fig as a penetrating hole. For low intensity hot spots, only puncture is predicted.

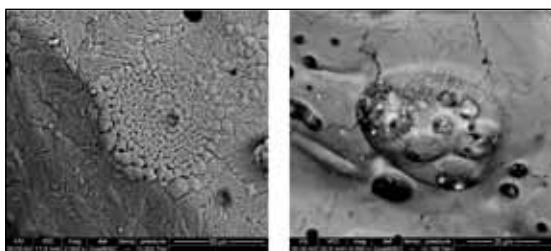


Fig.5. Surface morphology of failed surfaces

Fig.5 shows the tree like structure of melted component after failed by puncture. The ceramic oxides melted due to current localization and resolidified as a tree like structure. The energy handling capability depends only weakly on the diameter of a hot spot, but there is a tendency for smaller hot spots to lead to puncture and for larger spots to lead to cracking. Cracking failure occurs when the thermal stress exceeds the critical thermal stress. Cracking becomes more likely as the degree of nonuniformity increases [18]. Puncture and cracking are less when the current is uniformly distributed. The distributions of current, temperature and thermal stress were studied by simulation on the two-dimensional Voronoi network model [17]. Macroscopic nonuniformities that originate in ceramic processing lead to nonuniform current flow and

therefore nonuniform heating. The uniformity of the distribution of current, temperature and thermal stress can be improved by increasing the uniformity of grain size, effective grain boundary and the uniformity electrical character of grain boundaries.

Conclusion

Major cause of failure of high voltage varistor such as puncture and cracking has been analyzed through the microstructural characterization. Puncture phenomenon explained by microstructure disorder due to current localization. Ineffective microstructure leads to puncture and cracking failure due to high temperature and thermal stress when injecting rectangular impulse in long duration test. The microstructure of failed ZnO varistor ceramics can be effectively described Hence, it is very important that the homogeneous distribution in the microstructure which must be achieved by the processing of the varistor.

References

1. M. Matsuoka, "Nonohmic properties of zinc oxide ceramics", *Jpn. J. Appl. Phys.*, 10, 736, (1971).
2. T.K. Gupta, "Applications of zinc oxide ceramics", *J. Am. Ceram.Soc.*, 73, 1817, (1990).
3. M. S. Castro and C. M. Aldao, "Thermionic, tunnelling and polarization currents in zinc oxide varistors", *J. Eur. Ceram. Soc.*, 17, 1533-1537, (1997).
4. M. Bartkowiak, M. G. Comber, G. D. Mahan, "Failure modes and energy absorption capability of ZnO varistors", *IEEE Trans. Power Delivery*, 14, 152-162, (1999).
5. International Electrotechnical Commission. *Surge arresters – Part 4: Metal-oxide surge arresters without gaps for a.c. systems 60099-4. 2 ed.* Genebra (2004).

CORRELATION OF FAILURE MODES OF ZINC OXIDE VARISTORS WITH THEIR MICROSTRUCTURES

6. J. F. Wang, W.B. Su, H.C. Chen, W.X. Wang and G.Z. Zang, "(Pr, Co, Nb)-doped SnO₂ varistor ceramics", *J. Am. Ceramic Soc.*, 88, 331-334, (2005).
7. J. C. Wurst, J.A. Nelson, "Lineal intercept technique for measuring grain size in twophase polycrystalline ceramics", *J. Am. Ceram. Soc.*, 55, 109 (1972).
8. M. Inada, "Crystal phases of nonohmic zinc oxide ceramics", *Jap. J. App. Phys. part 1-Regular Papers & Short Notes*, 17, 1-10, (1978).
9. A. T. Santhanam, T. K. Gupta, and W. G. Carlson, "Microstructural evaluation of multicomponent ZnO ceramics", *J. App. Phys.*, 50, 852-859, (1979).
10. M. Inada, "Microstructure of nonohmic zinc oxide ceramics", *Jap. J. App. Phys., part 1-Regular Papers & Short Notes*, 17, 673-677, (1978).
11. K. Eda, "Zinc oxide varistors", *IEEE Electrical Insulation Magazine*, 5, 28-34, (1989).
12. M. Inada, "Formation mechanism of nonohmic zinc oxide ceramics", *Jap. J. App. Phys.*, 19, 409-419, (1980).
13. E. Olsson, L. K. L. Falk, G. L. Dunlop, and R. Österlund, "The microstructure of a ZnO varistor material", *J. Mat. Sci.*, 20, 4091-4098, (1985).
14. M. A. Ramtrez, "The failure analyses on ZnO varistors used in high tension devices", *J. Mat. Sci.*, 40, 5591-5596, (2005).
15. M. V. Lat, "Thermal properties of metal oxide surge arresters", *IEEE Trans. Power Appar. Syst.*, 102, 2194-2202, (1983).
16. A. Mizukoshi, J. Ozawa, S. Shirakawa, and K. Nakano, "Influence of uniformity on energy absorption capabilities of Zinc oxide elements as applied in arresters", *IEEE Trans. Power Appar. Syst.*, 102, 1384-1390, (1983).
17. Jinliang He, Jun Hu, Qingheng Chen, "Microstructure simulation on puncturing phenomenon of ZnO varistor under high current" *Properties and applications of Dielectric Materials, 2006. 8th International Conference*, 956-962, (2006).
18. H. Wang, M. Bartkowiak, F. A. Modine, R. B. Dinwiddie, L. A. Boatner, G. D. Mahan, "Nonuniform heating in zinc oxide varistors studied by infrared imaging and computer simulation", *J. Am. Ceram. Soc.*, 81, 2013-22, (1998).

DEVELOPMENT OF INVAR-SILVER COMPOSITE FOR MIC CARRIER PLATE OF SATELLITES

D. K. Mishra, T. T. Saravanan, G. P. Khanra, S. C. Sharma & Koshy M. George

Materials and Mechanical Entity, Vikram Sarabhai Space Centre, Trivandrum – 695022, India

Abstract

Invar based Invar-Silver composite has great potential for the use as carrier plate of Micro-wave Integrated Circuit (MIC) for satellites due to its high thermal conductivity and optimum co-efficient of thermal expansion (CTE). High Thermal conductivity material is required to dissipate the heat which is generated from the microcircuits. Whereas optimum Co-efficient of thermal expansion of the composite is to match with the CTE of the ceramic substrates (Such as Al_2O_3 etc.) bearing the carrier plate to prevent the failure of the solder due to the thermal stress.

In the present work, experiments trials were carried out to develop Invar based silver composite through Powder Metallurgy route, having 20 - 25 wt% silver and balance with invar. High purity Invar powder and Silver lumps were selected as a raw materials. Invar Powders were compacted at different compaction pressures and sintered at 1150 – 1250°C under hydrogen atmosphere to achieve a controlled porosity in sintered Skelton. Invar Skelton subsequently infiltrated with silver through capillary action at a temperature above the melting point of silver. The composite thus obtained was characterized through physical, thermal and mechanical property evaluation. Thermal conductivity of 48 – 55 W/m.K and CTE in the range of 5.8 – 6.2 ppm/K were obtained. SEM microstructures revealed the homogenous distribution of silver in the composite.

The present paper describes the details of processing and characterization of the composite with desired properties.

Key words: Composite material, Sintering, Compaction, Infiltration, Micro-wave Integrated Circuit

Introduction:

Microwave integrated circuit (MIC) is an integrated circuit design for operation at frequency of 1 GHz or more and these circuits are miniature in size, find its potential application in satellite. In satellites, high density MIC's printed on a ceramic substrates (Such as Al_2O_3 etc.) attached with metallic carrier plate. Optimal CTE to prevent the failure of the solder due to the thermal stress and high thermal conductivity to enhance the heat dissipation capability are essential requirement. Ceramic substrate is attached to the metallic carrier plate either by brazing or soldering. High thermal conductivity metallic material along with the optimum Co-efficient of thermal expansion (CTE) and

enhanced mechanical properties, finds its vital application for the use as a carrier plate of a Microwave integrated circuit. Conventionally, Kovar (Fe-30Ni-19Co alloy), tungsten – copper composite, tungsten-molybdenum composite, Copper, Aluminum, Invar, etc. are the candidate materials for the carrier plate application [1 -2]. In current scenario, Metallic material based carrier plate were used for providing the mechanical support to the ceramic substrate. Materials like W-Cu, W-Mo having the high thermal conductivity which is in the range of 180 – 200 W/m.K, 160 -170 W/m.K along with CTE of 6.5 – 8.3 and 7.8 respectively are suitable materials but adds weight penalty, not desirable for space application [3]. Copper and Aluminum

DEVELOPMENT OF INVAR-SILVER COMPOSITE FOR MIC CARRIER PLATE OF SATELLITES

having a high thermal conductivity along with high CTE, however high CTE difference between the Substrate and carrier plate should be avoided, which otherwise will produce the thermal mechanical stress and may cause the solder failure. Currently Kovar has been used for carrier plate because of its CTE (5.5 ppm/K) nearly matching with the CTE of ceramic substrate (Al_2O_3 ; 6.2 – 6.7 ppm/K) [3 – 4]. Owing to lower thermal conductivity, heat dissipation capability of Kovar is poor and does not dissipate the heat from the substrate to the surrounding so efficiently. In order to enhance the thermal conductivity of the Kovar, Silver has been added and comprehensive research on this topic are given by Eluri Ravindranath et al [5]. He found that with addition of silver (25 – 35 Wt.%) thermal conductivity of Kovar increased from 17 W/m.K to 75.3 – 102 W/m.K, and CTE increased from 5.5 ppm/K to 8.4 – 9.7 ppm/K. Sunil jha et al. [6] processed Cuvar, composite of Invar and Copper through Powder Metallurgy route having CTE in range of 7 – 9 ppm/K with high thermal conductivity. Authors mentioned that cuvar is thermally stable in the temperature range (-70°C - 400°C), and exposure to higher temperature will cause diffusion interaction between the components of the system. In order to overcome the issues like Optimum CTE, thermal conductivity and diffusion interaction, an Invar – Silver composite has been designed with CTE meeting with the ceramic substrate and thermal conductivity, more than that of Kovar. The above composite utilizes the advantage of the both constituent like low CTE of Invar and high thermal conductivity of Silver. Processing of the Invar-Silver composite needs optimization of the process route and parameters in order to realize a component with required properties. This paper details the complete characterization of the developed composite in terms of mechanical [like ultimate tensile strength

(UTS), yield compressive strength (YCS) etc.], Thermal and Physical properties.

Experiments:

For the development of the Invar - Silver composite; Invar Powder (Purity : 99 %, Average particle Size: -325 mesh), Silver powder (Purity: 99%, Average particle Size: 10 μ m) and Silver lumps (Purity : 99.5%) were taken as raw materials. Uniform Distribution of Silver in Invar matrix and its densification poses challenges during development of Invar-Silver composite, which calls for proper selection of process route and parameters. In general two different process routes were followed initially for the optimization of the process route, namely Compaction, Sintering and Infiltration route.

Compaction and Sintering route:

Powders of Invar and Silver were thoroughly mixed in turbo mixture (Make: Insmart system, India) for 4 hrs, in order to achieve a uniform distribution of Silver in Invar matrix. Invar – Silver mixed powder having silver content 20 – 25 Wt.% has been processed. The mixed powders were uni-axially green compacted at pressure within a range of 25 – 45 Kg/mm² using a Hydraulic Compaction press with a metallic die-punch system. The green compacts were sintered under hydrogen atmosphere at a temperature 900 \pm 25°C and 1150 \pm 25°C, for a soaking time of 90 minutes. Sintered specimens were shown in Figure: 1. Green density and sintered density were measured through geometrical formula, Density (ρ_1) = Mass / Volume. Mass of the specimens was measured using a single pan balance (Make: Afcosct) with an accuracy of \pm 0.01 gm. Dimensions were measured using a digital vernier caliper (Make : Mityutoyo) of accuracy \pm 0.03 mm. Volume was calculated using the formula $V = \pi r^2 h$. %TD (% Theoretical Density) of realized composite was calculated from

DEVELOPMENT OF INVAR-SILVER COMPOSITE FOR MIC CARRIER PLATE OF SATELLITES

measured density (ρ_1) and theoretical density (ρ_{th}), $\%TD = \rho_1 * 100 / \rho_{th}$. Theoretical density of Invar - Silver composite were calculated based on the Rule of Mixture and it is found 8.67 g/cc.

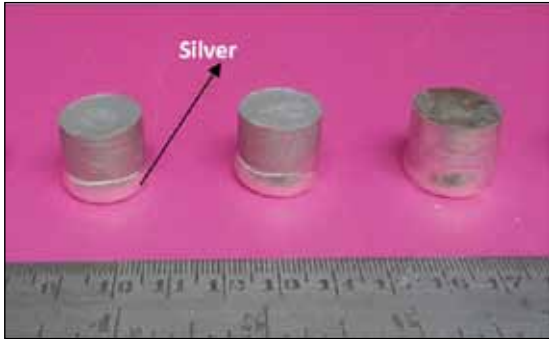


Fig. 1: Sintered at $1150 \pm 25^\circ\text{C}$, showing accumulation of Silver at bottom

Infiltration route:

Infiltration is a process, by which low melting point metal can be filled inside the porous skeleton material due to the capillary action. As per the literature it is found that there is no solid solubility between invar and silver, melting point difference between these two constituent make the infiltration route more attractive. In this experiment Invar powder were uni-axially green compacted at pressure within a range of 5 - 40 Kg/mm² using a Hydraulic Compaction press with a metallic die-punch system. The green compacts of invar were sintered under hydrogen atmosphere at a temperature $1250 \pm 25^\circ\text{C}$ for 90 minutes. Parameters like, sintering temperature and soaking time were kept constant in order to optimize the compaction pressure towards realization of Invar skeleton with required porosity. A porous skeleton of invar with 20 - 22 % porosity was realized which was subsequently infiltrated with silver at a temperature $1175 \pm 25^\circ\text{C}$, under hydrogen atmosphere for 60 minutes. In Infiltration process, processed Invar skeleton of 70 mm Diameter were kept

inside the graphite mould (a coating of Boron Nitride has been given to avoid the reaction of invar with graphite) and silver lumps (each of wt. approx. 15gm) uniformly distributed over the surface of the skeleton. Infiltration temperature and time were chosen in such a way so that flowability of molten silver will be sufficient for the filling the pores available inside the invar Skelton. Infiltrated Invar with silver block processed through in-house shown in Fig. 2.



Fig. 2: Processed Invar - Silver Composite through Infiltration route

Specimens for evaluation of the mechanical, thermal and physical properties were realized from the processed block as shown in Fig. 3.

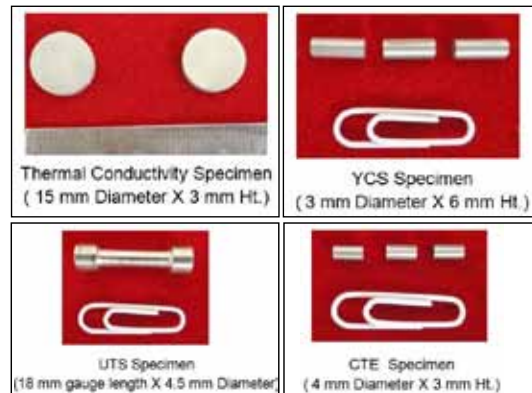


Fig. 3: Specimens realized from composite block towards property evaluation

DEVELOPMENT OF INVAR-SILVER COMPOSITE FOR MIC CARRIER PLATE OF SATELLITES

Uniform distribution of silver in invar matrix has been confirmed by SEM observation as shown in Fig.4.

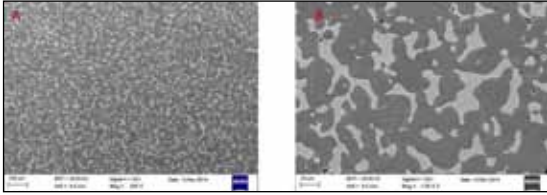


Fig. 4 : SEM photograph of infiltrated sample at 200 X (A) and 1000 x (B)

Hardness of the composite was measured by using a vicker hardness tester at a load of 5 Kg. Mechanical properties like Ultimate tensile strength, % elongation and Compressive strength have been evaluated at specimen level. Thermal conductivity was measured by laser flash apparatus under Argon atmosphere from RT to 200°C. Co-efficient of thermal expansion were evaluated from RT to 200°C by using Dilatometer. Poisson's ratio (μ) and Young's modulus were evaluated on the processed block by Ultrasonic means. For evaluation of Poisson's ratio, fundamental equation of sound wave were used:

$$\mu = [1/2 - (C_t/C_l)^2] / [1 - (C_t/C_l)^2]$$

Where C_t : Transverse Velocity in material,
 C_l : Longitudinal velocity in material

C_t and C_l where evaluated by normal pulse echo method and angle beam probe respectively. Young's modulus (E) was evaluated by Poisson's ratio from equation;

$$E = C_l^2 \times \rho [(1-2\mu) \times (1+\mu)] / [1-\mu]$$

Where ρ is the density of the processed composite.

Result and Discussion:

Processing of Invar - Silver composite involved the optimization of process route and process parameter with respect to initial raw material condition (Mixed powders of

Invar and Silver, Invar), Compaction pressure, Sintering temperature and soaking time. In order to optimize the process route and process parameter, mixed powder green compacted at pressure within a range of 25-45Kg/mm² followed by sintering under Hydrogen atmosphere at 900±25°C. Fig. 5 Shows the densification behavior of the specimen (processed through mixed powder) after green compaction and sintering. Green density and sintered density were observed in the range 72 - 81 % and 78 - 89% TD respectively, which indicates that further densification of the composite is required, to achieve optimal Mechanical, Thermal and Physical property.

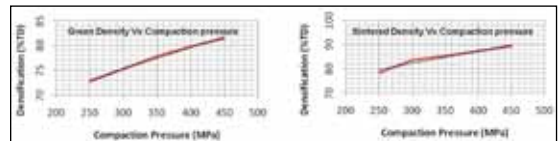


Fig. 5: Effect of compaction pressure on Densification of Mixed powder sintered at 900 ± 25°C

In expectation of improved densification specimens were green compacted (mixed powders) followed by sintering at 1150 ±25°C. After sintering Silver got melted and settled down at the bottom of the specimens, which was an issue for getting the homogeneity of the silver distribution in invar matrix, which results in an-isotropic property in the composite. Hence to maintain the homogeneity in the composite, Infiltration route were followed. During infiltration route, Invar powders were green compacted at pressure within a range of 5 - 40 Kg/mm² Fig. 6 shows the effect of compaction pressure on the densification of invar, as compaction pressure increases, density also increased. The green compacted specimens were sintered at 1250 ±25°C in order to achieve a controlled porosity Invar Skeleton followed by infiltration with silver in invar skeleton at 1175 ±25°C .

DEVELOPMENT OF INVAR-SILVER COMPOSITE FOR MIC CARRIER PLATE OF SATELLITES

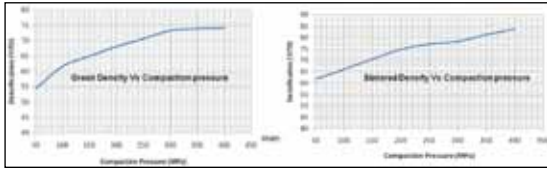


Fig. 6: Effect of compaction pressure on Densification of Invar powder sintered at 1250±25°C

Table: 1 Property Achieved in the processed block through infiltration route sintered at 1250 ± 25°C

Property	Achieved
Chemical Composition (Wt.%)	Silver : 24.2 – 25.8 , Invar : Balance
Density (g/cc)	8.44 – 8.48
Co-efficient of thermal expansion- CTE (ppm/K)	5.8 – 6.26
Thermal Conductivity (TC) @ 200°C (W/m.K)	50.37 – 56.37
Ultimate tensile strength – UTS (MPa)	344 – 349
Elongation (%)	23 - 25
0.2 % Yield Compressive Strength- YCS (MPa)	205.8 – 209.6
Young's Modulus (GPa)	121
Hardness (Vickers – VHN)	159 – 164

SEM photographs of the specimens confirm uniform distribution of the silver in invar matrix, along with the some leftover porosity in the composite. Chemical analysis of the sample were done in order to confirm the wt. % of Silver in composite and it was found in the range of 23 – 25.6 %.

Conclusion:

1. Compaction and sintering route were found not desirable, since sintering below melting point of silver will produces the composite with 11 % porosity. Sintering above melting point of silver will lead the segregation of the silver at bottom of the specimens.
2. Composite processed through Infiltration route, gives the densification 97 -98 %TD
3. Processed Composite showing better properties as compared to Kovar.

References :

1. A.V.pathak, K.J.Patel, B.S.rao, V.Jayaram, "The need and approach for the development of metal matrix composites for hybrid microcircuits for space use," *Proc. Conf.*, 250 – 256, 3rd Int. Conf. Advances Composites (ADCOMP), Bangalore, India, Aug. 24 – 26, (2000).

2. C. Zweben, " High Performance thermal management materials," *Electron. cooling*, 5 (3), 36 – 42, (1992).
3. Boddapati Srinivasa Rao, Ch. Hemambar, A. V. Pathak, K. J. Patel, Jürgen Rödel, and Vikram Jayaram, "Al/SiC Carriers for Microwave Integrated Circuits by a New Technique of Pressureless Infiltration", *IEEE Trans. Electr. Pack. Manuf.*, 29 (1), 58 – 63, (2006).
4. Carl Zweben, "Thermal Management and Electronic Packaging Applications", *ASM Handbook : Composites*, Volume 21, 1078-1084, (2001).
5. Eluri Ravindranath Tagore, Anish Upadhyaya, Anand V. pathak, "Processing of Silver for MIC Packaging Applications", *IEEE Trans. Electr. Pack. Manuf.*, 31 (3), 260 – 265, (2008).
6. Sunil jha, "CUVAR- a new controlled expansion, high conductivity materials for electronic thermal management", *Proc. Conf.*, 542-547, *Electron. Components and Technology Conference*, Las Vegas, NY, (1995).

RESEARCH TRENDS IN LASER ASSISTED ADDITIVE MANUFACTURING

Abhishek Singh Chauhan¹, Ujjwal Dubey¹, Arvind Kumar²

¹Dept. of Mechanical Engineering, National Institute of Technology, Bhopal – 462003, India

²Dept. of Mechanical Engineering, Indian Institute of Technology, Kanpur – 208016, India

Abstract

Laser Assisted Additive Manufacturing (LAAM) is used as an innovative tool to easily manufacture components from the structural ceramics such as alumina, or to process titanium alloys which are very effective for use in industries, especially aerospace, due to their light weight and high strength-to-weight ratio. Considering the advantages and applications of LAAM, much focus has been shifted to this field of manufacturing, in the last decade or so, in order to develop new technologies using lasers or to make this process sustainable and affordable in various fields. To explore the possibilities of research in this field, an attempt has been made to present a review of the available literature related to these LAAM processes. The present paper draws attention towards various laser assisted techniques, their current scenario and future research directions in this field.

Different laser assisted layered manufacturing techniques for the fabrication of components are discussed. A description highlighting the working principle, methodology and critical assessment for each of these techniques is provided. Current application, challenges and future possibilities of each process along with research trends in modelling of material fusion, melting and transport behavior during the process have been presented. Finally, the applications of these processes in various industries like biomedical, aerospace and automobile industry including the challenges and future directions for research and improvement in these fields are presented.

Keywords: *Laser Assisted Additive Manufacturing, Selective Laser Sintering, Selective Laser Melting, Laser Engineered Net Shaping, Modelling.*

1. INTRODUCTION

Additive Manufacturing (AM) refers to a process by which digital 3D design data is used to build up a component in layers by depositing material [1]. AM, another name for Layered Manufacturing, is defined as “the process of joining materials to make objects from 3D model data, usually layer upon layer, as opposed to subtractive manufacturing methodologies”. Additive manufacturing offers several advantages over conventional manufacturing techniques, such as reduced production time, zero material wastage, better process control, capability to form functionally

graded parts, no tooling requirement, feasibility of small production batches, economical and possibility to quickly change design[2]. AM can fabricate functional customized products for application in the aerospace, biomedical and automotive industry[3].

In the present competitive manufacturing environment, AM is widely billed as ‘the next industrial revolution’, but in reality there are still significant hurdles for successful commercialization of the technologies. AM is faced with numerous challenges such as increasing variations of products and product complexity, and decreasing delivery time. In

RESEARCH TRENDS IN LASER ASSISTED ADDITIVE MANUFACTURING

response to these challenges, major industrial and research efforts have been concentrated on rapid development of prototypes, rapid tooling, and rapid manufacturing[1]. The concept of Rapid Manufacturing (RM) – the production of end-use parts from additive manufacturing systems[4]– is emerging today; though its economic impact remains modest. A timeline is shown in Table 1 highlighting past,

Present and potential future AM developments and applications [5]. Lasers have been extensively used in various rapid prototyping (RP) technologies and are at the forefront of RP technologies. The applications of lasers in RP are derived from the ability to control the laser beam characteristics and quality such that desired interactions between the laser beam and a variety of materials can be achieved for the creation of final part geometry.

Table 1: AM application timeline [5]

This timeline lays out past, present and potential future AM developments and applications. (courtesy of Graham Tromans)	
1988-1994	rapid prototyping
1994	rapid casting
1995	rapid tooling
2001	AM for automotive
2004	aerospace (polymers)
2005	medical (polymer jigs and guides)
2009	medical implants (metals)
2011	aerospace (metals)
2013-2016	nano-manufacturing
2013-2017	architecture
2013-2018	biomedical implants
2013-2022	in situ bio-manufacturing
2013-2032	full body organs

Laser assisted additive manufacturing (LAAM) employs a laser beam as a heat source to melt a thin layer on the surface of the substrate while using blown metal powder to deposit a layer of predetermined shape and dimensions. A number of such layers, deposited one

on another, results in fabrication of three-dimensional (3D) components directly from their CAD models[6]. LAAM is an emerging process for manufacturing hard and brittle materials and fabricating complex shapes. LAAM is used as an innovative tool to easily manufacture components from the structural ceramics such as alumina, or to process titanium alloys which are very effective for use in industries, especially aerospace, due to their light weight and high strength-to-weight ratio.

There are various types of laser assisted manufacturing techniques like Selective Laser Sintering, Selective Laser Melting, Laser Engineered Net Shaping. Each of these techniques involves subjecting powdered form of material to laser pulses and has its own advantages and limitations.

In this paper, a description highlighting various aspects such as materials and properties, comparison, challenges, current research trends, future aspects and applications of these processes is presented.

2. VARIOUS LAAM TECHNIQUES

2.1 Selective Laser Sintering (SLS)

The process works by using localized heat from a laser to selectively fuse the powdered material, often via melting of the particles or melting of a binder applied to the powdered particles. Typically either a continuous wave or modulated CO₂ laser is used with power ranging from 1 – 250 W. However, more recently Nd: YAG lasers have also been successfully used. This process consists of three stages [7] as it is schematized in Fig 1. (1)

A layer of powder is deposited on the elevator and pressed; each layer of powder is pre-heated before the scanning to minimize the need of induced laser heat.

- (2) Laser radiation sinters the powder to form the profile of the section.
- (3) The elevator drops through a distance equivalent to the thickness of the section, and the process is repeated until the prototype is completed.

The laser beam is moved in the X-Y directions by a scanner system. There are very fast and highly-controllable motors which drive mirrors that paint the laser beam over the surface of the compacted powder in the build chamber. The laser selectively fuses the powder in the form of the cross section of the object. A nitrogen atmosphere is also maintained in the fabrication chamber which prevents the possibility of explosion in the handling of large quantities of powder. After the object is fully formed, the piston is raised to elevate the object. Excess powder is simply brushed away and final manual finishing may be carried out. To increase the density of the final part, additional operations, such as hot isostatic pressing or infiltration, are also required depending on the application [8].

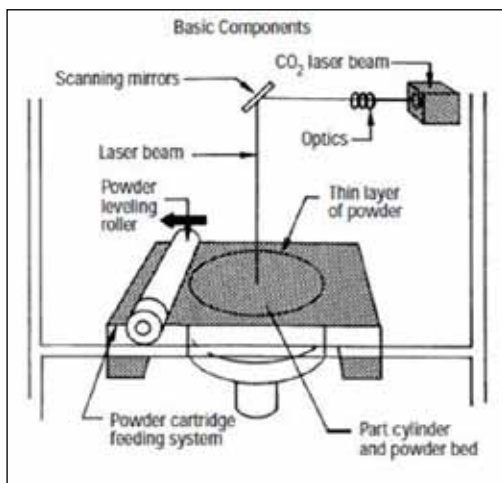


Fig. 1: Illustration of the Selective Laser Sintering process[9]

2.1.1 Advantages and Limitations

SLS, invented at the University of Texas at Austin and commercialized by DTM Corporation, has attracted a wide attention due to the fact that the SLS process fabricates the parts without the support structure and is applicable to a wide range of powder materials [10]. The ability to produce parts in a range of real engineering plastics and metals has enabled laser sintering to compete with less expensive technologies. It's often the method of choice for additively-manufactured parts with critical material properties in fields such as aerospace and medicine. A variety of thermoplastic materials such as nylon, glass-filled nylon, and polystyrene are available. In spite of its potential application in various areas, SLS is used limitedly only because dimensional accuracy of its products is still inferior to that of conventional machining processes and it fails to meet the expectation of the present parts. It requires expensive components such as the laser and scanner system, leading to very high equipment prices - often well over US\$100,000. Materials are also expensive. Improving the accuracy is vital to further commercializing SLS technology [11].

2.1.2 Types of SLS: Selective laser sintering process can be further divided into two different processes as

Indirect SLS: In the indirect SLS methods, organic materials such as polymers or inorganic material which exhibit low viscosity upon heating are used as binder materials. The structural metallic or ceramics powders are mixed with or coated with thin layer of binder prior to laser sintering. During sintering, the laser energy is selected such that the binder material melts and forms a bond between the structural particles without actually melting

them. The melting of the binder is exhibited by its high infrared absorption and low melting point [12]. The sintered parts obtained by the indirect SLS are highly porous (~45% porosity) and hence need to be further densified to achieve the desired mechanical properties.

Direct SLS: In direct SLS, a high-energy laser beam directly consolidates the metal powder to a high density (>80% theoretical density), preferably with minimal or no post-processing requirements.

The main advantages associated with this technique are the elimination of expensive and time-consuming pre-processing and post-processing steps, as compared to indirect or conventional processes. Direct SLS has been investigated on metal and metal-ceramic material systems in the past [13]. These material systems include binary and ternary mixtures, such as bronze-nickel and tungsten carbide-cobalt-nickel. Density of up to 80% of the theoretical density can be attained.

2.1.3 Materials

SLS can be used to process almost any material, provided it is available as powder and that the powder particles tend to fuse or sinter when heat is applied. Materials that can be processed by SLS are polymers such as nylon (neat, glass-filled, or with other fillers), metals including steel, titanium, alloy mixtures, ceramics (Al_2O_3 , SiO_2 , and ZrO_2), composites and green sand (Fig.2).

2.1.4 Past Computational and Experimental Studies

The important physical processes relevant with the SLS are heat transfer and sintering of powder [14]. Thus, the modelling of SLS primarily involves the sub-models

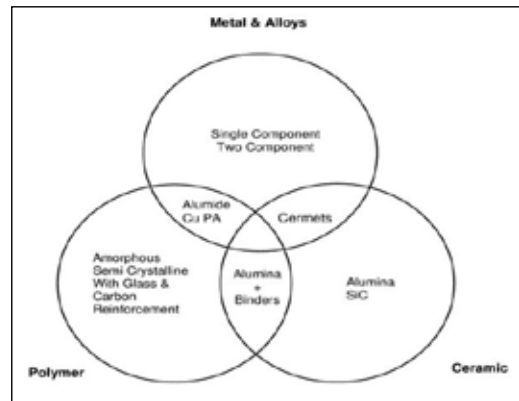


Fig.2 : Materials for SLS

corresponding to heat transfer and sintering [15]. The sintering models used are based on the analysis of Scherer [7, 16] and Mackenzie and Shuttleworth [17]. Buge daetal.derived a three-dimensional model for selective laser sintering based on the basic model structure: thermal and sintering sub-models. In these models, a new solution strategy has been implemented to rewrite the thermal and sintering equations in order to get a steady state problem[15]. The temperature and density distributions obtained provide useful information about the sintering properties such as the sintering depth.

Many researchers have proposed different ways to simulate this process so that process parameters (laser power, scan rate, etc.) can be optimized for the sintering of a given part and material. Matsumoto et al proposed a FE method for calculating the temperature and stress distribution in a single layer of sintered material [18]. Nelson et al.used empirical data to create a 1D heat transfer model of SLS that can predict sintering depths [19]. Simchi and Pohl et.al.used empirical results to determine a relationship between energy input and densification during SLS [13].

Thermal imbalance of SLS parts occurs in the build chamber during the sintering process, which is a typical factor for occurring shrinkage that severely influences the dimensional accuracy. Both powder properties and fabrication parameters have a strong influence on the shrinkage of SLS, with the latter more significantly. Therefore, understanding the relationships between the process parameters and shrinkage is the prerequisite to improve the accuracy of the parts. Much research has been devoted to the study of shrinkage and accuracy of the prototyping. Childs et al. reported on the thermal and powder densification modelling of the selective laser sintering of amorphous polycarbonate[20]. Li Xiang-sheng et al. investigated the shrinkage forms and shrinkage rules of the SLS process[21]. Williams et al. studied the energy delivery, heat transfer, and sintering process along with other pertinent phenomena[22]. Yang et al. studied the shrinkage compensation of SLS by using the Taguchi method[23].

2.2 Selective Laser Melting (SLM)

Despite the huge variety of additive manufacturing processes only a few of them have the potential to meet the requirements of flexible industrial manufacturing and one of those key processes is Selective Laser Melting (SLM). SLM, schematized in Fig. 3, is a powder bed process that begins with the deposition of a thin layer of powder onto a substrate. A high power laser raster scans the surface of the powder, the heat generated causes powder particles to melt and form a melt pool which solidifies as a consolidated layer of material [24]. Once the layer has been scanned another layer of powder is deposited and is again melted by the laser and solidifies to form the next layer of the part. The process is repeated layer after layer until the part is complete (wiki). SLM is very similar to SLS in terms of equipment but uses a much higher

energy density, which enables full melting of the powders. Therefore the fabricated parts exhibit a density very close to the theoretical one.

2.2.1 Advantages

Selective laser melting (SLM) allows the fabrication of complex three-dimensional (3D) and fully-dense physical models, parts and tools directly from computer-aided design (CAD) data using various powders, including metals, alloys and metal matrix composites (MMCs). Complete melting of powder in SLM could produce parts with much higher density and strength.

2.2.2 Materials

The types of materials that can be processed by SLM include stainless steel, tool steel, cobalt chrome, titanium & aluminium. All must exist in atomized powder form and exhibit certain flow characteristics in order to be capable for processing[25].

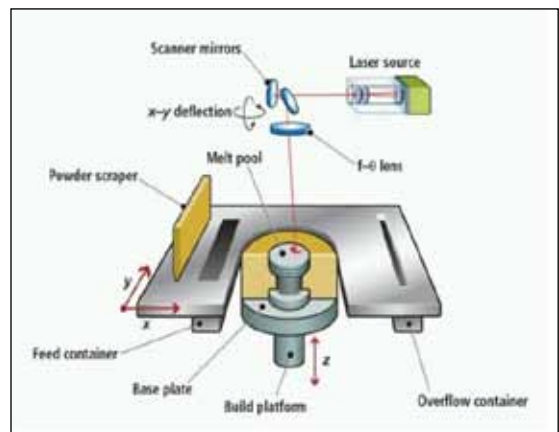


Fig. 3: Illustration of the Selective Laser Sintering process[9]

However the production of metal parts via SLM has many difficulties. Many processing issues arise due to the use of a high power laser to fully liquefy material from a powder bed.

High heat input often causes an increase in material vaporization and spatter generation during processing. Surface roughness is another SLM issue that is influenced by particle melting, melt pool stability and re-solidifying mechanisms which is discussed in section 2.4

2.2.3 Past Computational and Experimental Studies

Physical phenomena associated with LAAM processes are complex, including melting/solidification and vaporization phase changes, surface tension-dominated free-surface flow, and moving heat source. The variable process parameters together with the interacting physical phenomena complicate the development of process property relationships and appropriate process control. Thus, an effective numerical modeling of the process is very useful for understanding the impact of various process parameters and predicting optimized conditions. A lot of work has been done in the past to simulate the process, or parts of it, with various methods and for different materials.

A metal powder mixture of nickel and steel was investigated in the work of Chen and Zhang [26], where both powders had different melting temperatures. Their three-dimensional physical model, which is an extension of the 2D-model from a previous work (Chen et al., 2004)[27], contained the liquid flow of the molten material driven by capillary and gravity effects and was simulated with the finite volume method. Temperature distribution, influence of the intensity of the heat source and the scanning velocity were compared for different process parameter.

Kolossov et.al.developed a purely thermal model in three dimensions[28]. The model was discretized in time and space by applying the Finite Element method(FEM). Temperature dependent material parameters for a titanium

powder were used and emphasis was put on the modelling of the laser radiation. This same model was also used (Contuzzi et al.) to simulate the temperature distribution in the SLM process by means of the FE method. In this work, the powder-liquid-solid change of the material was included by checking the computed temperature values at the nodes of the FE mesh[29]. The goal of this work was to investigate the influence of the parameters on the temperatures occurring in the process

when using AISI 316 metal powder and a Nd:YAG laser beam. In the work of Zäh and Lutzmann, a thermo mechanical model was introduced and used to compute the deformations and residual stress of the produced part[30].

Riedlbauer et al.analyzed the laser energy input into a powder bulk for different process parameters by comparing temperature distributions and the size of melting pools[31]. Experiments with single-line specimens were conducted, analyzed and compared to numerical results from finite element simulations of the highly nonlinear thermal problem. The energy input of a laser beam into thermoplastic PA12 powder material was analyzed experimentally and numerically by means of temperature distributions and melting pool dimensions. Thereby, the influence of various laser powers and scanning velocities was evaluated. As expected, increasing the laser power or decreasing the scanning velocity increased the width and depth of the melting pool.

Dong et al. focused on the analysis of temperatures occurring in the selective laser melting process of polycarbonate powder, where also phase transformations were considered [32]. Furthermore, the influence of the scanning speed, the laser intensity and the beam spot diameter were investigated.

2.3 Parameters for SLS and SLM

There are various parameters which affect SLM/SLS (Fig. 4). These parameters are adjusted to get fully dense, direct to use parts. In theory, many materials could be processed by LAAM; however, the range of commercially available material for SLM/SLS is still limited today. This is because many physical properties of the materials affect their processing e.g. thermal expansion coefficient, melting point, thermal conductivity, surface tension, laser absorption and viscosity[33].

2.3.1 Material Parameters

Powder: Powder is a basic building block of the process. Its shape, size, type, and properties influence the process, the powder bed density, flowability and laser-material interaction.

Particle Size Distribution (PSD): PSD affects the important powder characteristics of flowability and compaction. If the powder consists of a very high percentage of larger particles, flowability is improved but the powder bed density is reduced which can reduce the final density of the part. By reducing the particle size, the layer thickness can be reduced, thus reducing the side surface roughness of the part. Therefore, a powder should consist of adequate amount of smaller particles to fill the gaps and increase the powder bed density but not influence the powder flowability and deposition[34].

Powder Morphology: Spherical particles are known to improve powder flowability and the quality of the layer and final product in additive manufacturing techniques [35]. A non-spherical powder has been observed to have less compaction and hence increased porosity in the parts.

Density: The individual particle density depends upon the type of material and is an intrinsic material property, while the packing density can be a loosely packed density or tapped density of the powder depending on the compaction method.

Thermal Conductivity: It depend upon the compaction of the powder (i.e. number of contacts of particles) If powder has high thermal conductivity, higher laser energy would be needed to melt it as because of its high conductivity, heat will dissipate faster[36].

Powder Flowability: For the powder to flow smoothly, it should have the following properties: spherical in shape, lowest surface roughness, narrow powder size distribution, incompressibility, high density, hard and stiff.

2.3.2 Laser Parameters: Since the SLM/SLS uses thermal energy of a laser beam to melt the powder, so properties of a laser are extremely important. Several important parameters like Pulse width/ pulse rate, time gap between two pulses wave length of the laser, mode, beam quality and spot size etc. affect the process [37]

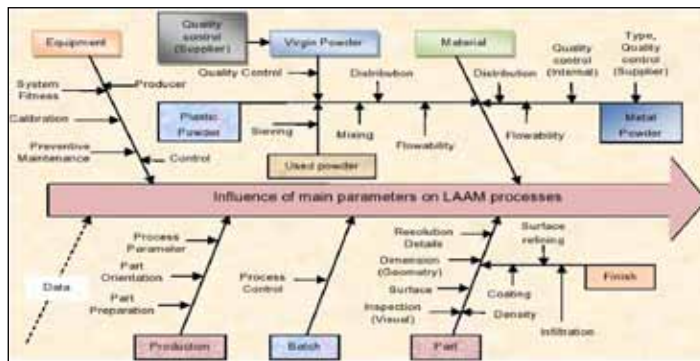


Fig. 4: Effect of Various Parameters

Laser Power: Surface roughness was found to increase with an increase in average laser energy density. Its magnitude depends upon the type of materials processed.

2.3.3 Process Parameters

Scan Speed: It directly influences its productivity. It also affects the density of the final processed part.

Hatch Spacing: Hatch spacing is the distance between two successive scan tracks. A certain amount of overlap is necessary between two consecutive hatch lines to avoid porosity and provide better layer integrity.

Layer Thickness: Layer thickness is another important parameter directly related to the production speed. With an increase in layer thickness, higher production speed is achieved while with its decrease, higher precision is achieved[38].

Scanning Strategy: It is a method of scanning powder bed with laser beam in order to increase the product quality. Good scanning strategy makes the resultant products free from distortion, warp, anisotropy, inaccuracy, and porosity.

The environmental factors which have an influence on the SLM process include the type of gas filled in the chamber, gas pressure and flow and powder bed pre-heating etc.

2.4 Challenges

Surface Finish: To achieve higher material removal along with a desired surface finish is always a critical issue. Variations in the surface topography/physical texture can influence a variety of performance characteristics as these characteristics become critical under certain operating conditions; the surface finish can dictate the performance, integrity, and service life of the component [37]. Commercial powder bed machines such as MTT's Realizer and EOS

M270 often require post-processing operations such as surface machining, polishing and shot peening to attain final part surface finish [39].

Surface roughness is heavily dependent on laser processing parameters and control of melt pool. A technique known as pulse shaping has been shown to extend the degree of control over a laser's energy distribution and therefore has the potential to improve the control over melt pool formation, stability and eventual part properties. Mumtaz and Hopkinson et.al. used pulse shaping to minimize the top surface roughness and melt pool width.

Pulse shaping is a technique used to temporally distribute energy within a single laser pulse[40]. This provides the user an added degree of control over the heat delivered to the laser material interaction zone. Pulse shaping was shown to reduce spatter ejection during processing, improve the top surface roughness of parts and minimize melt pool width.

Pulse shaping is also known to affect the properties of the built part, where a ramp-up pulse has a positive effect on reduction of part distortion and residual stresses, and a ramp-down pulse increases the time for which the material is kept in the molten state and helps improve top surface roughness[41].

Laser surface re-melting (LSR) may also be a solution that does not need removing the part from the building platform which avoids fixation errors. Experiments were carried out in which only the top surface was re-melted [42], surface quality of parts, manufactured by SLM and then exposed to LSR, demonstrated a significant improvement in term of measured average roughness. Dai et al has done the simulation of the melt pool dynamics and the top surface quality of selective laser melting(SLM) of TiC/AlSi10Mg composite powder system, using a finite volume method (FVM). They considered both thermo-capillary force and recoil pressure

induced by the material evaporation, which are the major driving forces for the melt flow[43]. It shows that the surface tension is an important factor in the formation of the solidified surfacemorphology and the role of applied laser energy input per unit length (LEPUL) in determining the surface quality of SLM-processed parts. They have optimized the laser energy input per unit length (LEPUL of 500J/ m) for the formation of a fine and flat melt pool surface.

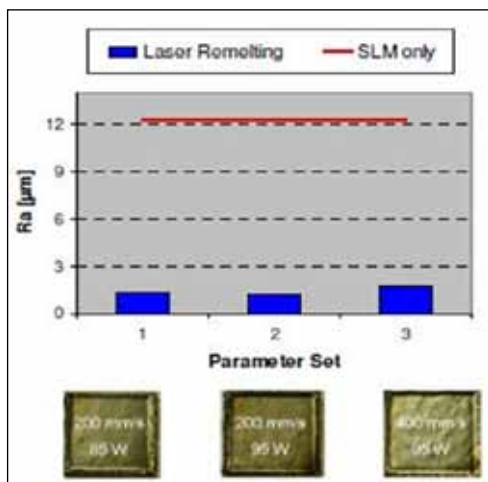


Fig. 5: Surface quality of parts manufactured by SLM and then exposed to LSR demonstrates a significant improvement in term of measured average roughness. (Source: Kruth et al., 2004) [25]

Density Problem: Density of the finished part after SLM/SLS is also an important concern. The density determines the part’s mechanical properties which in turn has direct influence on the component’s performance

Scan speed has a significant effect on density. At sufficiently low scan speeds, the relative density is almost independent of the layer thickness for the selected range of the layer thickness, and a maximum of 99% relative density is achievable. At higher scan speed values, a higher layer thickness results in less density [26].

Residual Stress: One of the major concerns in SLM/SLS parts is residual stress and distortion. Due to localized heating, complex thermal and phase transformation stresses are generated during SLM/SLS. In addition, frequent thermal expansion and contraction of the previously solidified layers during the process generates considerable thermal stresses and stress gradients that can exceed the yield strength of the material. Residual stresses can lead to part distortion, initiate fracture, and unwanted decrease in strength.

Balling: A very critical issue in SLM is the instability of a liquid on a solid where the liquid splits into smaller entities in order to reduce the surface tension variations. When the molten metal in the SLM process shows this behaviour, it is called balling. Kruth et al. examined the cause of this phenomenon in the SLM process and found that when the total surface of the melt pool becomes larger than that of a sphere of the same volume then balling occurs [25]. He also showed that if the length (L) to diameter (D) ratio of the melt pool is greater than 2.1 then the molten metal would break up into small droplets instead of a continuous line. Simchi and Pohl et.al. researched the surface conditions of pure iron powder under different scan line spacing’s, pointing out that the balling was because of capillary instability and the balling can be decreased by reducing the scan line spacing [13].

2.5 Laser Engineered Net-Shaping (LENS)

Laser Engineered Net Shaping (LENS) is a novel manufacturing process for fabricating metal parts directly from Computer Aided Design (CAD) solid models. LENS was developed in Sandia National Laboratories, USA, to fabricate metal components directly from CAD solid models and reduce the lead times for metal part fabrication. Figure (6) shows a schematic of the LENS process. The

fabrication process has several steps: First, a solid model is sliced electronically into a sequence of layers of a given thickness. Second, to build a metallic part, a solid substrate is used as a base and the laser beam is focused on the substrate to create a molten pool into which powder is simultaneously fed. Third, the substrate is moved beneath the laser beam, to trace out a pattern defined by the electronic slice of the model, melting material is added to the surface as a narrow strip of added material. Starting from the bottom of the part, one layer is produced at a time. After formation of a layer, the powder feeding nozzle and laser beam assembly is moved in the z direction. Accordingly, the part is then built line by line and layer by layer.

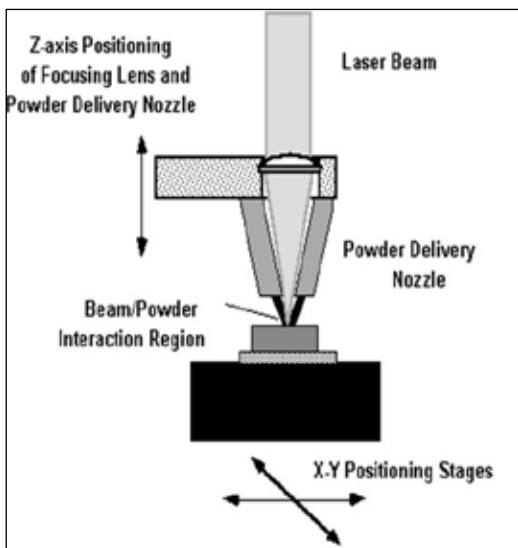


Fig. 6: Schematic of LENS Process [44]

2.5.1 Advantages

The advantage of the LENS process is to fabricate complex three-dimensional components with high strength and ductility directly from a CAD solid model. The process can reduce the cost and time significantly through a one-step operation[45]. The greatest advantage of laser cladding processes is their

unbeaten ability to produce gradient materials by applying different powder delivery nozzles that allow to gradually switch from one material to another, which is a unique feature that is of great interest to designers.

The most significant features of the LENS technology are its high cooling/solidification rate, rapid prototyping process, and proper shape control. It has the advantages of improving material structure, thermal stability and mechanical properties, and increasing manufacture efficiency when compared to conventional methods. Another unique processing feature of LENS is the capability of selectively applying metal to existing parts or repairing worn or broken parts while maintaining the integrity of the parent material[46].

LENS has the unique capability of producing parts with thin walls and high depth-to-diameter aspect ratios. Parts have been fabricated with 0.014 in. (0.356 mm) diameter holes and 1 in. tall having a depth-to-diameter aspect ratio of more than 70:1.

2.5.2 Materials

The LENS process allows deposition of an extremely wide range of materials, including tool steels, austenitic stainless steels, Ni-based superalloys, copper alloys, titanium alloys and functional composites with improved physical and mechanical material properties. The process also allows fabricating multiple materials structures with gradient or stepped material transitions [47]. It is presently commercialized by Optomec (NM, USA). Balla et al. have used LENS technique to fabricate compositionally and structurally graded Ti-TiO₂ structures [48]. These exhibit a stable interface between the two materials augmented by high surface hardness. Such gradient structures provide useful mechanical support for the wear resistant, low friction exterior layers and minimize the likelihood of localized

failure. The graded structures with varying concentrations of TiO_2 on the top surface were found to be nontoxic and biocompatible. These unitized structures with open porosity on one side and a hard, low friction surface on the other side can eliminate the need for multiple parts with different compositions for load-bearing implants such as total hip prostheses. Kathuria et.al.utilized laser micro cladding process with aNd:YAGlaser of average power of 20W and minimum spot diameter of 20 mm for the fabrication of micro parts made of Co-alloys, nickel and stainless steel [49-50].

2.5.3 Past Computational and Experimental Studies

The critical issues in the LENS process include the process repeatability, the geometry accuracy, and the uniformity of microstructure properties. In order to achieve the desired characteristics and improving the LENS process, the various parameters which affect the process are optimized. The main process parameters are laser power, travel velocity, and powder flow rate which affect the temperature profile and cooling rate in the molten pool, as well as thermal cycles at each location of the fabricated part. Consequently, these parameters determine the size of the molten pool, the part deformation, and the microstructure of the deposited layers [44].These, in turn, determine the geometry accuracy and the mechanical properties of the finished part.

There has been an increasing interest in investigating the LENS process. Many experimental studies have been performed in an effort to provide fundamental insight into the influence of process parameters on product properties [51]. The effects of the laser-processing parameters (laser power and scanning speed) on the molten pool size have been investigated both by experiments and modelling. For constant laser scanning speed,

the geometry of the molten pool depends on the heat input distribution. During operation of the LENS machine, real-time thermal images of molten pool size are used as a feedback mechanism to control the process [52]. The laser power is adjusted to make sure that the molten pool size is in the pre-defined range during the fabrication process.

The LENS process has the potential to dramatically reduce the time and cost required to fabricate functional metal parts. Since mechanical properties are dependent upon the microstructure of the material, which in turn is a function of the thermal history of solidification, an understanding of the thermal behavior of the fabricated part during the LENS process is of special interest. In particular, a number of these studies have attempted to clarify thermal measurement issues that emerge from the understanding of the interaction between the laser beam and the metal powder component. Researchers have studied temperature effects either by inserting thermocouples into the substrate [44]or by using thermal imaging techniques to measure the temperature during the build, coupled with finite element methods [51].

Optimization of the process requires a complete understanding of the complex thermal history during part fabrication. Numerical simulation methods have the potential to provide detailed information of the thermal behaviour. Numerical models have been performed by several authors to simulate the temperature history and microstructure evolution during the LENS process[53]. Some preliminary finite element modelling of the LENS process has also been published. Hofmeister et al. treated the problem as the multidimensional moving boundary problem[54]. They simulated LENS processing by finite element method (FEM) with element birthing. This method has a clear physical meaning and provides vivid thermal

images of the LENS process. The preliminary temperature field in the fabricated wall was obtained.

3. SCOPE FOR FUTURE MATERIALS IN LAAM

3.1 New Materials

One of the success factors of additive manufacturing in the future could well be its ability to produce complex shaped parts in materials that are difficult to manufacture conventionally, like hard metals, ceramics, composites, etc. (Fig. 7) During the past decade, tremendous progress has been achieved in developing new or better materials for additive manufacturing processes. Selective laser sintering can now be applied directly (i.e. without use of polymer binder) to metals like bronze, steel, hard metal (WC-Co), or to ceramics (Si-C). Today, parts in basically any materials can be produced by one or another additive manufacturing process: polymers (thermoplastics, thermo setters, and photo-polymers), metals, ceramics, wood-like parts, and composites.

Polymer matrix ceramic can be produced by selective laser sintering of polymer coated metal or ceramic powder.

Besides composites, many LAAM techniques allow production of multi-material parts, with for instance a soft core and hard skin. Multi-colour parts can be produced today by using appropriate colourable photo- polymers with a patented stereo-lithography process. Varying the laser energy allows selective colouring of certain areas of the part.

3.2 Metals

Different metals including high performance and bio-compatible metals are currently being processed and optimized for different engineering applications. All these materials find their use in different fields. Titanium, cobalt chrome and some precious metal alloys have been used in manufacturing medical

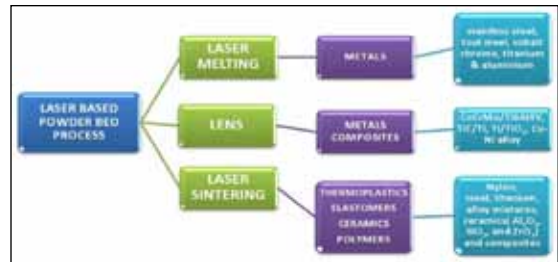


Fig. 7 : Types of Materials Processed By Different LAAM Techniques

implants because of their bio-compatibility. Nickel based super alloys, Inconel 635, 316L stainless steel and M2 alloys which are processed by LAAM techniques have been used for high performance applications such as in aerospace. Metal composites, combining a high strength structural metal having a high melting point with a low melting metallic binder; have been produced by selective laser sintering. Metal matrix ceramic composites (which normally include WC-Co ceramics) could also be produced easily by selective laser sintering) [55].

Although metallic parts have been manufactured by LAAM technologies, they are currently facing issues of quality, repeatability and standardization (to be qualified to be directly used in critical applications like the aerospace industry). Many people from the field of academics and industry are currently focusing on these issues and it is the focus of much current research.

3.3 Future Trends

Material selection is the real issue and the biggest opportunity in recent days. As the technology matures, the range of materials used will increase based on the need for improved mechanical properties as well as the life expectancy of produced objects. More than 20% of the output forms are end products, which emphasize the need of compatible materials to enhance the performance of products manufactured. According to the

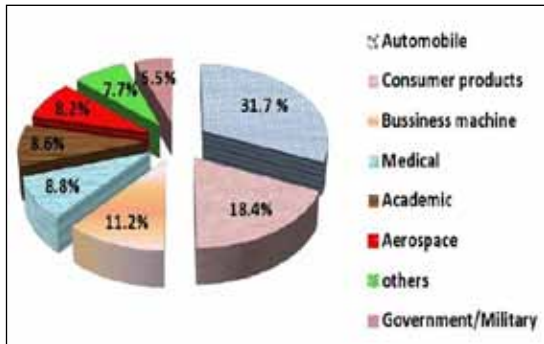


Fig. 8: Application of LAAM in Various Fields

industry experts, the number will increase up to 50% in less than 10 years. Plastics are becoming the material of choice with the market revenue for plastic materials in additive manufacturing forecasted to reach \$209.6 million by 2018.

Significant focus is expected in developing more cost effective materials that can be used for various end applications instead of specific ones; this will help in expansion of the use of a particular material for various applications. There is a demand for better materials to use as feedstock for LAAM. The development of machines that can process metals by sintering (creating objects from powders) is helping to open up the processes to industrial users. However, while new metal alloys such as Scalmalloy5 address manufacturers' needs, polymers require greater research and development.

Opportunities for biomaterials are expected to emerge in next five to six years in consumer, healthcare and energy industries. Plastics and composites will have increased adoption in electronics, automotive and aerospace industries.

4. APPLICATIONS AND DIRECTIONS FOR FUTURE RESEARCH FOR LAAM

Three of the fastest-growing areas for AM include the medical, automotive and aerospace

sectors. AM's success in the biomedical sector rests with its ability to create customised prosthetics, implants, replacement tissues and intricate body parts, including blood vessels. The largest adopter has been the aerospace industry with the entrance of metals-fed AM machines into the industry in 2011, resulting in good take-up of the technology owing to advantages of speed, cost and materials rationalisation.

4.1 Biomedical

With the development of modern design and manufacturing, additive manufacturing technology is broadly used in biological and biomedical engineering. Bio-additive manufacturing encompasses applications to tissue-engineered substitutes, artificial organs, orthopedic implants, medical devices, and biological chips produced by printing/patterning cells and proteins.

The introduction of additive manufacturing (AM) in combination with computer-aided technologies has offered new possibilities for medical modeling: using computer models. Medical modeling has a wide range of applications in anatomical representation, implant and prosthesis design, and surgical planning and rehearsal.

4.1.1. Using SLS

SLS was first used to make biomodel for operational and surgical planning and produced implants indirectly by fabricating corresponding pattern and molds. Making artificial limb for leg or shell for hearing instruments is another application. Extensive research has been done for developing scaffolds for tissue engineering using SLS [56]. Materials used are polymers and bio-composites[57]. The process gives facility to design various shapes and sizes of pores of scaffold, which facilitates the tissue ingrowth.

Changing the percentage of pores in scaffold helps adjust its mechanical strength. It helps to make scaffold of various strength as per the strength of the tissue, which is required to prevent stress shielding effect.

4.1.2 Using SLM

SLM has been used to make metallic scaffolds using steel and titanium. Some research is going on to develop magnesium-based biodegradable scaffolds. Another application of SLM is biomedical implants. A number of customized implants for hip, elbow, shoulder, knee, jaw, and skull have been successfully fabricated [58]. Research has also been done to make implants from alumina-zirconia but it has not yet reached the commercial stage. Dental health care has seen tremendous growth with the fabrication of dental implants, bridges, crowns, and partial removal denture. Recently, a dedicated machine has been introduced to make dental products using SLM [59].

Bio Additive Manufacturing (BAM): Biofabrication using cells, biologics or biomaterials as building blocks to fabricate biological and bio-application. Bio fabrication encompasses enormous applications in tissue science and engineering, disease pathogenesis and drug studies, biochips and biosensors, in-cell printing, patterning, assembly, and organ printing.

4.1.3 Challenges: For LAAM technology to move forward the following challenges have been identified:

- Lack of process repeatability and part reproducibility, particularly when using new materials.
- Lack of information and assurance from AM machine vendors about the end performance results.

- Integration of BAM with micro and nano systems is difficult because of the requirement for a clean environment.
- Lack of viable integrated fabrication processes to make heterogeneous BAM structures with cells, growth factors, and scaffolding materials included in the same physical model.
- Lack of capability of producing 3D cell biological models and tissue constructs with desired reproducibility and controllability.
- Lack of available biomaterials and cell delivery media for BAM.
- Lack of understanding of BAM process induced effects on living biologics and on subsequent structural and time-dependent cellular behavior.
- Lack of knowledge of cell behavior in BAM under a 3D structural environment, and lack of understanding of cell behavior under integrative structural, chemical and biological cues.
- Lack of computer modeling and simulation of heterogeneous tissues and cell/tissue growth.

4.1.4 Future Possibilities

- Better scientific understanding of BAM process.
- Increase of BAM process robustness.
- Integration of multiple BAM processes including printing, extrusion, spraying, electro spinning, coating, etc. for biofabrication.
- BAM of scaffolds, implants and prostheses with functionally gradient materials and customized structure to meet patient-specific anatomy, tissue function, and load bearing requirements.

- BAM of 3D cell aggregates and assemblies used as in vitro 3D biological models for regenerative medicine, disease pathogenesis and drug studies.
- BAM of human tissues for reducing and replacement of animal testing and BAM of organs.
- Modeling and analysis of cell/tissue growth in a 3D environment and multi-scale modeling: from sub-cellular to tissue level with time dependence.
- Development of integrated nano and micro BAM fabrication processes.
- Development of BAM for cell-integrated micro-fluidic devices, biochips and biosensors and of protein/biomolecule printing and patterning.

4.2 Aerospace

The aerospace industry is a key growth market for Laser Assisted Additive Manufacturing. Functional components with complex geometries and defined aerodynamic properties can be manufactured quickly and cost-effectively using it.

For the aerospace industry which is the biggest titanium market in the U.S. [60], LAAM are used for making turbine blades, turbine discs, hinges, metallic brackets, air grates, panel covers and other interior parts. For making engine parts operating at higher temperature, nickel-based alloys are used. Boeing and Airbus are using the process for making various aerospace parts. Advantages of LAAM are Cost Reduction, Tool less Production, Time Saving, Minimal waste, Light weight design.

4.2.1 Using SLS: Intelligent lightweight structures manufactured using laser sintering processes combine high strength with a weight reduction of 40-60%. The material savings translate into more flexibility in design and engineering. As a result airplanes consume

significantly less fuel and emit less carbon dioxide.

“Removing just one pound of weight from each aircraft in American’s fleet would save more than 11000 gallons of fuel annually”

AA flies 619 aircraft therefore 1 pound weight reduction on just one aircraft yields

- 114 pounds of fuel burn reduction annually, 2850 pounds over an aircraft’s service life
- \$55 per year fuel cost reduction, \$1375 of increased revenue for a plane’s service life [61]

SLS PA parts are used for making air ducts, panel, shroud, etc.

4.2.2 Using SLM: SLM processes are more advantageous since they can produce 100% dense functional metal parts. The motivation for using metallic SLM parts in aerospace is to increase the use of light metals (for decreasing the fuel consumption), to prevent the wastage of metals (so reduction of cost) and to decrease the lead time for production. When aerospace parts are fabricated through machining, only 2-10% of the initial block is used and the remaining material is wasted as chips. Adoption of SLM technology prevents this wastage and increases the buy-to-fly ratio. (EOS.info) The buy-to-fly ratio (the ratio between the weight of the raw material used to make a part and the weight of the finished part) can be up to 20:1 in conventional manufacturing and this can be reduced to less than 2:1 using LAAM. A good example is a titanium landing gear rib made by SLM, though previously made from steel by conventional machining. Total process time was reduced by SLM from 240 to 24 hours and waste from 91% to 13%.

4.2.3 Challenges and Future Direction

- SLS currently only offers control of thermal input, within a bounded space.

- Layer-wise manufacturing induces severe and variable 4D energy gradients.
- The processes are controllable, but new methods and approaches are required to be explored.
- New materials are becoming available for processing. Benefits of LAAM will be extended beyond current applications with new materials.
- Patent system and excessive litigation have slowed development.
- LAAM equipment needs to become more robust, like CNC and injection molding.
- Analysis methods need to grow with new geometric capabilities.

4.2.4 Future Possibilities

ALM will revolutionise the aerospace industry in the future due to its cost-savings and flexibility. Current research is going on how to improve and optimize the LAAM process for specific parts and alloys. Parameters being looked at include the powder size, the powder purity, the number of times the powder can be used before it is cleaned, the process parameters of power input, and the speed of the laser. The materials that are increasingly researched are titanium and its alloys (Ti6Al4V) because of their high specific strength.

LAAM can play an increasingly broad role in its manufacturing process, supporting the overall goal to make products that are greener and more efficient for customers.

4.3 Automotive

Additive manufacturing with metals is becoming increasingly important in the automotive industry. Time and cost reductions in production are making this generative technology increasingly attractive to the car makers. The primary focus is on aluminum

alloys which provide the basis for lightweight automobile construction. (Engineerlive.com) As conventional manufacturing techniques limit design freedom, so the components are always a compromise between function and feasibility. LAAM technology frees up development from these constraints, it only applies material where it is functionally necessary. This makes for extremely light and yet highly rigid parts which can even comprise integrated functions, it drastically reduce scrap and drive down material usage. Simple parts such as hinges, brackets and pneumatic actuators can be designed, produced and installed as integrated components. Reducing the mass of moving and/or accelerating components is especially important since this directly enhances energy efficiency. Furthermore, new technologies are increasingly able to produce multi material printed parts with individual properties such as variable strength and electrical conductivity. LAAM also plays an important role in creating faster, safer, lighter, and more efficient vehicles of the future.

LAAM is currently used to manufacture many parts of automotive (Eos.info). Some of them are:

Drive Shaft: An innovative drive shaft design results in more than 7 per cent weight reduction

Break Disk: Integrated cooling channels help to reduce weight and increase performance

Car Seat: Car seats can be designed much lighter and functions can be integrated

Heat Exchanger: New design structures in heat exchangers increase compactness and effectiveness.

As the number of additively manufactured parts increases, one company's goal is to use LAAM as the primary production technique for building vehicles. Urbee 2, an electric car with as many as 50 AM-produced parts, is under development and expected to debut in 2015[62].

4.3.1 Challenges and Future Possibilities

Nowadays the automotive industry is focused on energy-sustainable energy efficiency, the reduction of CO₂ emissions, ongoing cost pressure and the continuing demand for innovation - automobile manufacturers are faced with major challenges. Some of them are discussed below.

Materials: A wide variety of materials allows a greater number of properties to be embedded into final products. Currently research is going on the application of advanced materials that are already available. New processes capable of combining layer manufacturing with nano materials are under development, with the goal of increasing tensile strength, electrical conductivity, hardness, and impact strength[62]. Increase in strength without a corresponding increase in weight could potentially lead to LAAM even being used to make the body in white for automobiles in the future.

Manufactured Product Quality and Post Processing

Parts produced through most LAAM technologies occasionally show variability due to thermal stress or the presence of voids. This results in lower repeatability, which is a challenge for high-volume industries such as automotive where quality and reliability are extremely important. One way to tackle this challenge is through machine qualification, where companies follow industry standards.

Another concern is the dimensional accuracy of final parts produced is not always on par with those made through conventional manufacturing processes. Most components manufactured through LAAM require some form of post processing, which involves removing unused material, improving surface finish, and removing support material [63].

Hybrid manufacturing promises a solution for addressing current variability and finish quality concerns. Hybrid manufacturing refers to the combination of LAAM with traditional 3D opportunity in the automotive industry. This transforms the perspective of a product from a "single entity to a series of features" that can be produced through some combination of the techniques[64]. One example of a hybrid manufacturing technique is combining selective laser sintering and gel-casting technique for the fabrication of complex-shaped Al₂O₃ ceramic parts.

Economics of LAAM: The low production speed of LAAM is a significant impediment to its wider adoption for direct part manufacturing. This has made high-speed LAAM an important area of research.

Manufacturing Large Parts: One of the limitations of LAAM's utility in the automotive industry is the limited build envelopes of current technologies. Given this restriction, larger components such as body panels that are produced through LAAM still have to be attached together through processes such as welding or mechanical joining. To overcome this, low-cost AM technologies that can support larger build sizes for metal parts have to be developed. There is already significant research in progress. "Big area additive manufacturing," under development by Oak Ridge National Laboratory and Lockheed Martin, has the potential to manufacture products without any restrictions on size. (Areion by formula group T 75)

Currently a lot of work is going on LASER CUSING. The Laser cusing process allows the fabrication of both mould inserts with close-contour cooling and direct components for the medical, dental, automotive and aerospace sectors. Both prototypes and mass-produced parts are manufactured. The key benefits of Laser cusing include greater freedom

of geometry, coupled with much greater flexibility in terms of product development. Another central advantage of the process is the opportunity to produce components without the use of tools and the obviation of the machine programming associated with this.

Alternate energy/scanning sources: Though for polymeric systems, mask systems that are able to produce individual layers all at once (i.e., not point laser scanning) are becoming available, there is great potential for research to extend this approach for metal systems, which are universally using single point laser/electron beam scanning. Going away from point processing to line/full mask would provide significant speed and cost advantages

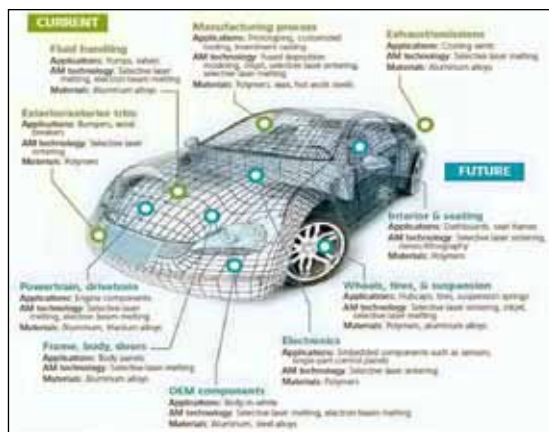


Fig. 9: A summary of components presently manufactured using AM and parts that can be potentially manufactured in the future (Source: Deloitte Analysis)

4.4 Micro Fabrication

Currently, one of increasingly important purposes in industry (from aerospace and automotive to biomedical and chemical) is to decrease component size and produce small-sized devices with high functionality. AM technologies have been widely utilized within a decade with the purpose of producing complicated 3D components. Fabrication of

3D micro parts/structures is also within the reach of some specific AM technologies via implementation of some essential modifications and improvements to get proper conditions for micro fabrication. Some of the common laser assisted 3D micro additive manufacturing techniques include Laser Micro Sintering and Laser Micro Melting. The research done in this field has been discussed in this section along with challenges and further improvements.

4.4.1 Laser Micro Sintering (MLS)

MLS first came into light in 2003 with the efforts of The Laser Institute Mittelsachene.V. when it proposed a unique MLS system and has since been employed for a variety of applications. MLS is distinct from SLS on account of q-switched pulses and a special coating procedure which was employed that resulted in preparation of functional micro parts with a structural resolution of 30µm from the respective powders. The micro components produced by this process reveal a general maximum resolution of less than 30 µm, resolution of 20 µm for ligaments, and resolution of 10 µm for notches at aspect ratios of 12 and a minimal roughness Ra of 1.5 µm can be obtained. Different micro parts from various metals can be produced by MLS process. Different powders such as tungsten, Cu, Ag and tungsten/Cu mixtures, single-phase Mo, and stainless steel alloy 316L have been successfully processed. Besides sub-micrometer sized powders also materials with grain sizes of 1-10 micrometers can be sintered. Regenfuss et al. has described the specific features and effects of q-switched laser pulses upon the powder materials[65]. In the middle of 2005, first successful results were achieved in generating oxide ceramics bodies with a special variation of the procedure and a modified type of the equipment. Non-oxide ceramics micro sintering is being investigated currently.

A critical challenge for MLS is the processing of non-metallic materials. Also, other challenges include limited materials, powder handling (recoating), part removal/cleaning, surface roughness and achievable resolution. Using dry powder dispensing techniques instead of conventional powder recoating can be a good solution to overcome fine powder handling problem. Dry powder dispensing systems (especially ultrasonic nozzle dispensing systems) have demonstrated their great ability in precise placement of fine powders [46-66]. Use of such a mechanism can be an efficient measure to solve the problem of fine powder handling and improve resolution of the process as well as adding possibility of lateral material change in multimaterial micro parts.

4.4.2 Laser Micro Melting (MLM)

Laser Micro Melting, a modification of SLM, makes it possible to create fully functional micro parts directly from metal powders without using any intermediate binders or any additional processing steps. Any specialized SLM system for micro manufacturing has not yet been developed, and few works have been addressed to fabrication of micro parts using SLM process [67].

Yadroitsev et al. has analyzed the possibility of using the SLM technology for fabrication of micro-sized parts. He conducted a series of experiments on pre-alloyed gas atomized SS grade 904L(-16 μm) and (-7 μm) powders on SLM machine PM 100 (Phenix Systems) [68]. He fabricated several models that could be used in micro cooling systems, the objects with highly developed surface and small-sized Kenics element to direct mixing of fluid flows. Also, the available commercial system SLM 50 of ReaLizer GmbH, Germany has the capability to produce fine features in the range of 40 μm , as it uses fine powders (smaller than 30 μm) and minimum layer thickness of 20 μm . A wide range of metals, including: super

alloys, aluminum (Al), stainless steel, tool steel, cobalt (Co) chromium and titanium have been processed successfully by ReaLizer's SLM system.

Further reduction in the size of the structural elements and fully functional objects leads to considerable difficulties and it also becomes complicated to reproduce the shape of the sample corresponding CAD model[69]. A critical challenge for MLM is the development of innovative systems for deposition thin layers of fine powders with high homogeneity and high packing density. Hence, to obtain positive results in the miniaturization process it is necessary to construct new specialized SLM machines.

It is possible to use compact laser of low power (0.2 W) with high stable and quality laser radiation. A small working area (1×1 cm) allows to apply the short-focal-length optics. At the focal spot diameter 10 μm , the laser power density is about $0.2 \times 10^6 \text{ W/cm}^2$ for these types of lasers, which is sufficient for melting metal and ceramic powders. Using a fine powder (~5 μm) and thin powder layers (~10 μm) will be able to produce the structural elements with the size about 20 μm and fully functional parts ~0.2 μm .

5. CONCLUSIONS

The future potential for meeting the AM requirements are very high, but have to be better focussed, combining its unique properties and features with the AM application needs. The role of the laser is important in context of AM with great potential and challenges. This paper contributes with an insight into the Laser Assisted Additive Manufacturing (LAAM) highlighting important techniques along with their relative advantages and limitations, materials that can be processed by each technique and current research trends in each technique. This article draws attention

towards application of LAAM techniques in different industries. To make LAAM more sustainable in these industries, challenges and future possible research directions in these fields are discussed. LAAM has a bright future but it needs to address several key issues including sustainability, affordability, repeatability, broader domain of materials processing and manufacturing speed for mass production. Much attention needs to be paid to manufacturing of functional parts for micro manufacturing industry. Also, better understanding and modelling of physical processes in LAAM will help in multi objective parametric optimization of these techniques which will yield the desired results in terms of dimensional accuracy, surface roughness and tolerances.

REFERENCES

1. Wohlers T. Additive manufacturing 101: Part I, Time Compression: accelerating product development, <http://www.timecompression.com/>, as 21.01.2010.(2010)
2. Paul C.P., Bhargava P., Kumar A., Pathak A.K., Kukreja L.M. in *Lasers in Manufacturing*, J. Paulo Davim (Ed.), 1-67, Wiley-ISTE, London, (2013).
3. Vaezi et al.(2013) Multiple material additive manufacturing-part 1: a review. *Virtual and Physical Prototyping* 8 (1):19-50.
4. Hague R., Campbell I., Dickens P.(2003) Implications on design of rapid manufacturing, *Proc. IMechE Part C: J. Mechanical Engineering Science* 217(1):25-30.
5. <http://www.raeng.org.uk/publications/reports/additive-manufacturing>
6. Gibson I., Stucker B., Rosen D.W. *Additive Manufacturing Technologies: Rapid prototyping to direct digital manufacturing*, Springer Science and Business Media,(2009).
7. Scherer G. (1977, a, b, c) Sintering of low density glasses: II, theory, experimental study and effect of a distribution of pore size. *J. Am. Cer. Soc.*,60:236-248.
8. Kruth J.P., Levy G., Klocke F., Childs T.H.C. (2007) Consolidation phenomena in laser and powder-bed based layered manufacturing. *CIRPAnnals - Manufacturing Technology* 56(2):730-759.
9. www.dabircan.blogspot.com
10. Maeda K. and Childs T.H.C. (2004) Laser sintering (SLS) of hard metal powders for abrasion resistant coatings. *Journal of Materials Processing Technology* 149(1-3):609-615.
11. Boillat E., Kolossov S., Gardon R. (2004) Finite element and neural network models for process optimization in selective laser sintering. *Proc. InstMechEng B J EngManuf* 218:607-614.
12. Kathuria Y.P. (1999) Microstructuring by selective laser sintering of metallic powder. *Surface and Coatings Technology* 116-119:643-647.
13. Simchi A., Pohl H.(2003) Effects of laser sintering processing parameters on the microstructure and densification of iron powder. *Materials Science and Engineering: A*359(1-2):119-128.
14. Ming-Shen, Sun, M. and Beaman, J. (1991a) A three dimensional model for selective laser sintering. *Proc. Solid Freeform Fabrication Symposium, Austin, TX* 102-9.
15. Bugeđa G., Cervera M., Lomberra G. (1999) Numerical prediction of temperature and density distributions in selective laser sintering processes. *Rapid Prototyping Journal* 5:21-26.
16. Scherer G. (1986) Viscoussintering under a uniaxial load. *J. Am. Cer. Soc.*, 69(9):206-07.
17. Mackenzie J. and Shuttleworth R. (1949). A Phenomenological theory of sintering. *Proc. Phys. Soc.*, London, Vol. 62(12-B):833-52.
18. Matsumoto M., Shiomi M., Osakada K., Abe. F. (2002) Finite element analysis of single layer forming on metallic powder bed in rapid prototyping by selective laser processing. *International Journal of Machine Tools and Manufacture* 42(1):61-67.
19. Christian Nelson J., Xue S. et al.(1993) Model of the Selective Laser Sintering of Bisphenol-A Polycarbonate. *Ind. End. Chem. Res.* 32.10:2305-2317.

20. Childs T.H.C., Berzins M., Ryder G.R. et al. (1999) Selective laser sintering of an amorphous polymer-simulations and experiments. *Proc. InstMechEng Part B* 213:333-349.
21. Xiangsheng LI, Ming H., Sheng S., Shuhuai H. (2001) Model of shrinking and curl distortion for SLS prototypes. *China Mechanical Engineering Journal* 12(8):887-889.
22. Williams J.D., Decard C.R. (1998) Advances in modeling the effects of selected parameters on the SLS process. *Rapid Prototyping J* 4(2):90-96.
23. Yang H.J., Huang P.J., Lee S.H. (2002) A study on shrinkage compensation of SLS process by using the Taguchi method. *Int J Mach Tools Manuf* 42:1203-12.
24. Santos E.C., Osakada K., Shiomi M., Kitamura Y., Abe F., (2004) Microstructure and mechanical properties of pure titanium models fabricated by selective laser melting. *Proc. InstMechEng Part C* 218:711-719.
25. Kruth J.P., Badrossamay M., Yasa E., Deckers J., Thijs L., Van Humbeeck J. (2004) Part and material properties in selective laser melting of metals. In: Wan Sheng, Z., Jun, Y (Eds.). *Proc. 16th International Symposium on Electromachining*, Shanghai Jiao Tong University Press, Shanghai, China.
26. Chen T., Zhang Y.(2006) Three-dimensional simulation of selective laser sintering of a two-component metal powder layer with finite thickness. *ASME J ManufSciEng*128:299-306.
27. Chen T., Zhang Y. (2004) Numerical simulation of two dimensional melting and resolidification of a two component metal powder layer in selective laser sintering process. *NumerHeatTransf, Part A: Appl.* 46:633-649.
28. Kolossov S., Boillat E., Glardon R., Fischer P., Locher M. (2004) 3D FE simulation for temperature evolution in the selective laser sintering process. *Int. J. Machine Tools Manufacturing.* 44 (2):117-123.
29. Contuzzi N., Campanelli S.L., Ludovico A.D. (2011) 3D Finite Element Analysis in the Selective Laser Melting Process. *International Journal of Simulation Modelling* 10: 113-121
30. Zäh M.F, LutzmannS.(2010)Modelling and Simulation of Electron Beam Melting. *Production Engineering* 4(1):15-23.
31. Riedlbauer D., Drexler M., Drummer D., Steinmann P., Mergheim J. (2014) Modelling, simulation and experimental validation of heat transfer in selective laser melting of the polymeric material PA12. *Computational Materials Science Journal* 93:239-248.
32. Dong L.,Makradi A., AhziS., Remond Y.(2009) Three-dimensional transient finite element analysis of the selective laser sintering process*Journal of materials processing technology* 209(2):700-706.
33. Khan M., Dickens P. (2010) Selective Laser Melting (SLM) of gold. *Rapid Prototyping Journal* 18(1):81-94.
34. Zhu H. H., Fuh J. Y. H., Lu L. (2007) The Influence of Powder Apparent Density on the Density in Direct Laser-Sintered Metallic Parts. *International Journal of Machine Tools and Manufacture*47(2):294-298.
35. Niu H.J., Chang I.T.H. (1999) Selective Laser Sintering of Gas and Water Atomized High Speed Steel Powders.*ScriptaMaterialia* 41(1):25-30.
36. German R. M. (1989), *Particle Packing Characteristics*, Metal Powder Industry, Princeton, New Jersey, ISBN: 0-918404-83-5.
37. Vora H.D, Santhanakrishnan S., Harimkar S. P., Boetcher S. K. S., Dahotre N. B. (2012) Evolution of surface topography in one-dimensional laser machining of structural alumina, *J EurCeramSoc*, 32(16): 4205-4218.
38. Majumdar J.D., Manna I.Laser-Assisted Fabrication of Materials. *Springer Series in Material Science*, e-ISBN: 978-3-642-28359-8.
39. DalgarnoK. (2007) Materials research to support high performance RM parts. *Rapid Manufacturing 2nd International Conference*, Loughborough University 147-156.
40. MumtazK.A., Hopkinson N. (2009) Selective Laser Melting of thin wall parts using pulse shaping. *Journal of MaterialsProcessing Technology* 210(2):279-287.

RESEARCH TRENDS IN LASER ASSISTED ADDITIVE MANUFACTURING

41. Mumtaz K.A., Erasenthiran P., Hopkinson N. (2008) High density Selective laser melting of Waspaloy(R). *J. Mater Process Tech* 195(1-3):77-87
42. Yasa E., Kruth J.P., Deckers J. (2008) Roughness improvement in selective laser melting. *Proc. of 3rd International Conference on Polymers and Moulds Innovations*, Ghent, Belgium 170-183.
43. Dai D., GuD. (2014) Tailoring surface quality through mass and momentum transfer modeling using a volume of fluid method in selective laser melting of TiC/AlSi10Mg powder. *International Journal of Machine Tools and Manufacture* 88:95-107.
44. Griffith M., Puskar J., Robino C., Brooks J., Smugeresky J. (2000) Understanding the microstructure and properties of components fabricated by Laser Engineered Net Shaping (LENS). *Materials Research Society Symp. Proc.* 625:9-20
45. Wang L., Felicelli S.D., Craig J.E. (2009) Experimental and Numerical Study of the LENS Rapid Fabrication Process. *ASME J Manuf Sci Eng* 131(4) 041019.
46. Yang S, Evans J.R.G. (2004) A dry powder jet printer for dispensing and combinatorial research. *Powder Technol* 142:219-222.
47. Keicher, D. M., Miller W. D., Smugeresky J. E.; Romero J. A. (1998) Laser Engineered Net Shaping (LENS): Beyond Rapid Prototyping to Direct Fabrication. *TMS Annual Meeting, Hard Coatings Based on Borides, Carbides and Nitrides: Synthesis, Characterization and Application* 369-377.
48. Balla V.K., Devasconcellos P.D., Xue W., Bose S., Bandyopadhyay A. (2009) Fabrication of compositionally and structurally graded Ti-TiO₂ structures using Laser Engineered Net Shaping (LENS). *Acta Biomater* 5:1831-1837.
49. Kathuria Y.P. (2000) Laser assisted metal rapid prototyping in microdomain. *Proc. Eighth International Conference on Rapid Prototyping*, Tokyo, Japan 160-165.
50. Kathuria Y.P. (2001) An overview of 3D structuring in microdomain. *The Journal of the Indian Institute of Science* 81:659-664.
51. Hofmeister W., Wert M., Smugeresky J., Philliber J.A., Griffith M., Ensz M.T. (1999) Investigation of solidification in the Laser Engineered Net Shaping (LENS) process *JOM* 51(7):1-6.
52. Griffith M.L., Ensz M.T., Puskar J.D., Robino C.V., Brooks J.A., Philliber J.A., Smugeresky J.E., Hofmeister W.H. (2000) *Mater. Res. Soc.* 625:9-20.
53. Wang L., Felicelli S.D. (2006) Analysis of Thermal Phenomena in LENS™ Deposition. *Mater Sci and Eng: A* 435-436:625-631.
54. Hofmeister W.H., MacCallum D.O., Knorovsky G.A. (1999), Video monitoring and control of the LENS process. *Proc. 9th International Conference on Computer Technology in Welding*, Detroit, MI 187-196.
55. Xiong Y., Smugeresky J.E., Ajdelsztajn L., Schoenung J.M. (2008) Fabrication of WC-Co cermets by laser engineered net shaping, *Materials Science and Engineering* 493(1-2):261-266.
56. Antonov E.N., Bagratashvili V.N., Whitaker M.J. et al. (2005) Three-dimensional bioactive and biodegradable scaffolds fabricated by surface-selective laser sintering. *Adv Mater* 17 (3): 327-330.
57. Cruz, F., Simoes J., Coole T., Bocking C. (2005) Direct Manufacture of Hydroxyapatite Based Bone Implants by Selective Laser Sintering. *Virtual Model Rapid Manuf* 119-125.
58. Emmelmann C., Scheinmann P., Munsch M., Seyda V. (2011) Laser Additive Manufacturing of Modified Implant Surfaces with Osseointegrative Characteristics. *Physics Procedia* 12(A):375-384.
59. Gebhardt A., Schmidt, F.-M., Hötter J.-S. (2010) Additive Manufacturing by Selective Laser Melting, the Realizer Desktop Machine and Its Applications for the Dental Industry. *Physics Procedia* 5:543-549.
60. Yu K.O., Imam M.A. (2007) Development of Titanium Processing Technology in the USA. *Proceedings of the 11th World Conference on Titanium (Ti)*, Kyoto, Japan.

61. Lyons.B (2011)Boeing Company National Academy of Engineering Frontiers of Engineering, Additive Manufacturing Boeing Research and Technology.
62. Kor J. (2012) URBEE: Designing with digital manufacturing in mind. Kor Ecologic.
63. Feloy M.,DSouza R., Jones R., Bayliss M. (2013) Technology and skills in the aerospace and automotive industries.Evidence Report 76.
64. Boivie et al. (2012) The concept of hybrid manufacturing for high performance parts, South African Journal of Industrial Engineering. 23 (2):106–115.
65. Regenfuss P., Streek A., Hartwig L., Klötzer S., Brabant T.H., Horn M., Ebert R., Exner H. (2007) Principles of laser micro sintering. Rapid Prototyping J 13:204–2120.
66. Yang S, Evans J.R.G. (2007) Metering and dispensing of powder; the quest for new solid freeforming techniques. Powder Techn 178:56–72.
67. Clare A.T., Chalker P.R., Davies S., Sutcliffe C.J., Tsopanos S. (2008) Selective laser melting of high aspect ratio 3D nickel–titanium structures two way trained for MEMS applications. Int J Mech Mater Des 4:181–187.
68. Yadroitsev I, Bertrand P. (2010) Selective Laser Melting In Micro Manufacturing. Annals of DAAAM for 2010 & Proceedings of the 21st International DAAAM Symposium 21(1) ISSN 1726-9679
69. Bartolo P.J. et al. (eds.) (2008) Virtual and rapid manufacturing, Taylor & Francis Group, ISBN: 978-0-415-41602-3, London.

NANO SIZED METAL OXIDE POWDERS FOR ENERGY STORAGE APPLICATIONS

Raghu C Reddy¹, R Narasimha Rao² and N R Munirathnam¹

¹Centre for Materials for Electronics Technology (C-MET), IDA Phase- 3, Cherlapally, HCL Post, Hyderabad, India.

²National Institute of Technology, Warangal, India.

Abstract

Materials for electrical energy storage are an important domain of research having vast possibilities for advancement. Lithium-ion batteries have emerged as work horse energy storage devices in modern electronic devices. Still the storage capacity and device durability are restricted by the materials of construction which are conventionally used. Any further improvement in the performance batteries is connected with research on these materials. The main components of Li-ion batteries are the electrodes and the electrolyte. This paper enumerates chemical methods employed for the preparation of oxide nanoparticles of tin for use in anodes of Li-ion batteries. The physical characteristics like, the crystallite/particle size and morphology were correlated with the preparation methods. The functional characteristics like the charge/discharge curves were correlated with the physical characteristics. The suitability of various nanopowders produced for use as electrodes in Li-ion batteries have been discussed.

Keywords: Energy Storage, nanomaterials, Li-ion battery

Introduction

Li batteries were developed as early as in the 1970's. Due to its lightweight, good voltage capability and energy density in comparison to other metals, Lithium (Li) has been the preferred material for the electrodes in Li cells. A decade later, attempts were made towards the development of rechargeable Li batteries using metallic Li as anode. Commercialization of such batteries was hindered due to difficulties in recharging the metallic Li-electrode [1,2,3]. The stripping and deposition of Li during electrochemical cycling caused roughness on electrode surface leading to increase in the surface area of the anode and formation of dendrites. These dendrites can grow to an extent that can perforate the separator and reach the cathode leading to internal short-circuiting. This may cause sudden increase in the temperature resulting in battery explosion. Several approaches have been tried

to overcome these problems with metallic Li. These include- usage of liquid electrolytes that are less reactive towards Li, adding surfactants such as hydrocarbons/ quaternary ammonium salts, that level the re-growth of Li, controlling properties of metal surface by using additives (CO₂, N₂O, HF etc.), coating Li with Li-ion conducting membrane, adding scavengers to the electrolyte that dissolve the Li-dendrites etc. [4]. These measures brought only a partial improvement in the cyclability of metallic Li. Lazzari and other workers worked on a solution to this problem as early as 1980, the period when Li-rechargeable batteries originated [5,6]. They suggested replacing Li metal by a non-metal compound capable of storing and exchanging Li. In conjunction with another non-metallic Li-accepting compound as cathode, the electrochemical cycling process would involve the transfer of Li-ions between the electrodes. This approach has led to development and commercialization

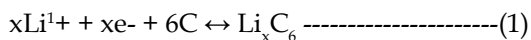
of Li-ion batteries (LIB). The development of LIB and the electrode materials have been described in various books and papers [1-4, 7-11]. One domain of research in the field of LIB anodes is directed towards improving the commercially used carbon anodes by bring about various modifications in their structure and morphology. The other domain is on replacing these by suitable alternates mainly consisting of metal oxides.

Carbon as anode

Carbon is the commercial anode material in use in LIB [1,2,4,9,11]. Its choice is attributed to a number of physico-chemical characteristics it possesses, including low atomic weight, chemical potential close to the metallic Li, operational safety, cyclability and recharge rate comparable to Li, flexibility and economy in cell design. The carbon anodes possess higher dimensional stability than metal alloys and also exhibit higher gravimetric and volumetric energy densities and negative redox potential as compared to many metal oxides, chalcogenides and polymers [1,2,4].

Reaction mechanism

The carbon electrodes undergo reversible reaction with Li according to Eqn. 1 and it is an insertion-de insertion also called as intercalation-de-intercalation reactions.



where, $0 < x < 1$, depending upon the type of carbon used.

Theoretically, Li-insertion in carbon is reversible. However, the lithium consumed in first charge (Li-insertion) exceeds the expected value of 372 mAh/g. Actually, Li-intercalated graphite is highly reactive and decomposes the electrolyte solution by consuming extra Li and

forms a solid film (solid electrolyte interphase, SEI) on the surface of the electrode. The SEI is stable and Li-ions consumed in this process are not released back during subsequent cycles, thereby causing irreversible capacity loss (ICL) during initial cycle. Thus, the following deinsertion of Li recovers only 85-90% of this charge. The subsequent cycles show good reversibility. However, whatever may be the developments in the carbon anodes; the limit of theoretical capacity remains 372 mAh/g. This requires research on alternative anode materials to improve capacity further.

Alloy Anodes

The systems that have been investigated to replace carbon for use as anodes through reversible reaction with Li via alloy formation are the metals and intermetallics such as Al, Si, Sn, Sb, Ge, Pb, Bi, In, SnSb, InSb, SnAg₃, Mg₂Si, Ni₃Sn₂ [2,4,7,9]. Equation 2 represents their electrochemical reaction with Li.



M= Al, Si, Sn, Sb, Ge, Pb, Bi, In etc.

The theoretical capacity with the alloy anodes is generally higher in comparison to graphite. However, the alloying/de-alloying reaction with Li is accompanied by enormous volume changes (~300% in case of Sn) as against LiC₆ formation that involves ~10% unit cell volume increase. This causes mechanical stresses leading to cracking and crumbling of the electrode which results in rapid capacity fading on cycling. As a consequence, feasibility of the pure metals for application in LIB gets impaired. However, the expected high reversible capacity remains the motive force to pursue research on alloy systems. It has been demonstrated by several researchers that the aforesaid shortcoming can be overcome

partly by reducing the particle size of the host material and partly by using multiphase instead of single-phase materials. A large number of binary and ternary alloy powders were investigated for their anodic response. Some examples are, sub micron size alloy powders of Sn-Sb, Sn-Ag, Sb-Ag, Sn-Sb-Ag [12], nano-Bi [13], mechanically alloyed Sn-Fe [14], superfine alloys of Sn/SnSb_x [15], Cu-Sn [16], etc. It is proposed that, upon Li-insertion, single phase Sn-Sb gets separated into Li-Sn and Li-Sb phases and the single phase Sn-Sb is reconstructed upon subsequent Li-extraction. This reversible phase separation-reconstruction process was found to be beneficial for good cyclability in comparison to that of the pure metals. Another limitation of alloy systems in comparison to graphite is the large Irreversible Capacity Loss (ICL) in the first cycle. The ICL occurs due to following reasons and has been reported extensively:

- Electrolyte decomposition at the electrode/electrolyte interphase to form Solid Electrolyte Interphase (SEI): Similar to graphite[17].
- Reduction of oxide impurities: Due to synthetic procedure, the alloy powders contain oxide impurities as well. These oxides undergo irreversible reaction with Li, forming metal and Li₂O during reaction with Li.
- Loss of contact: The variations in volume during reversible alloying reaction are considered to be the cause of electrode cracking and thus contact loss. This problem can be minimized by the use of finer particle size.
- Trapping of Li: This is due to immobilization of Li at the defect site inherent in the electrode material or created by the structure destruction during Li-insertion. Once Li-ions are trapped in these defect

sites, it may be impossible to extract all of them.

- Extended SEI formation: Due to loss of contact mentioned above, the breakup of existing SEI may occur thereby exposing fresh metal surface to the electrolyte. This will cause new SEI formation. Thus, the SEI formation gets extended to few initial cycles.

Keeping in view the stable cycling performance of graphite over large number of cycles and high capacity exhibited by alloys, it was envisaged to arrive at a compromising combination of the two [18,19]. Studies covering this aspect describe the electrochemical cycling of the composite- carbon nanotubes (CNT) with 28 and 56 wt% Sn-Sb nanoparticles [18] and a series of nano-SnSb with Meso Carbon Micro Beads (MCMB) [19]. Since both CNT/MCMB and SnSb are active hosts for Li, their composites in nanometer range, may enhance the interaction between the constituents and circumvent the deficiencies in the electrode performance when each constituent is used alone. It is reported that composite materials alleviate the volume variation effectively in MCMB/SnSb system if the weight ratio of Sn-Sb is less than 30%. In such a case, reversible capacity of 420 mAh/g with small capacity fading up to 25 cycles was achieved [19]. Among various alloy-systems investigated by researchers for anodic performance, tin (Sn) has been found to form alloy at ~0.25 V vs Li and provide high capacities (Li_{4.4}Sn: theoretical capacity: 761 mAh/g or 1941 mAh/cm³). Several studies on amorphous and crystalline Sn-oxides with or without additional metal/non-metal ions have been carried out.

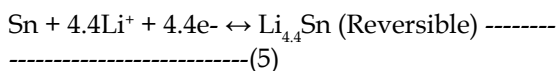
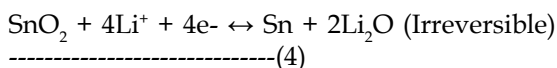
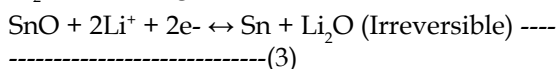
Tin-based oxides

Idota et al. [20] in 1997 reported that Amorphous Tin Composite Oxides (ATCO) could be the prospective anodes for LIB. The ATCO is a

tin oxide glass of the form, $\text{Sn}_x\text{M}_y\text{O}_z$, where M is a group of glass forming elements (boron and phosphorus), x, y and z's are variables. These oxides are prepared by quenching of constituent oxides from high temperatures. In ATCO, SnO acts as electrochemically active center for reaction with Li. The glassy matrix provides an electrochemically inactive network of $-(\text{M}-\text{O})$ bonds that separate the Sn atoms. Electrochemical cycling was done in the voltage range, 0.0-1.2 V vs Li. Initial discharge capacity was ~ 1030 mAh/g (~ 8 mol of Li per mol of ATCO). The corresponding charge reaction up to 1.2 V yielded a capacity of 650 mAh/g (~ 5 mol of Li per ATCO). Thus there was an irreversible capacity loss (ICL) of $\sim 37\%$. Subsequent discharge-charge cycles showed good reversibility with $\sim 100\%$ capacity retention. Chouvin et al. [21] have carried out Sn Mossbauer spectroscopic and X-ray absorption fine structure studies on ATCO ($\text{SnB}_{0.6}\text{P}_{0.4}\text{O}_{2.9}$) and showed that overall Li-insertion reaction involves two steps. First, Sn^{2+} reduction occurs and then Li-Sn alloy formation takes place. The findings of Idota et al. [20] have stimulated a large number of investigations on Sn-based compounds. Many types of Sn-composites and glasses [22-24], binary (SnO , SnO_2) [23,24] were studied as anodic systems. It was revealed that cyclability was not as promising as reported by Idota et al. [20] and capacity fading occurs in the ATCO.

Studies on crystalline SnO and SnO_2 [23,24] revealed the reaction mechanism regarding the first discharge and reversible charge-discharge cycling. The first discharge (reaction with Li) is the irreversible structure destruction of SnO/SnO_2 , with the formation of Sn-metal particles embedded in Li_2O matrix (Eqn. 2 and 4). The cycles afterwards are characterized by alloy formation as per eqn. 5 during charging and

de-alloying of $\text{Li}_{4.4}\text{Sn}$ during discharge with Li_2O remaining as inactive matrix.



Tailoring the microstructure and realization of amorphous or nano-crystalline tin oxides has resulted in the improved anodic performance [25,26]. Electrochemical tests on nano-crystalline/amorphous $\text{Sn}_3\text{O}_2(\text{OH})_2$ have shown that the first discharge and charge capacities are 1580 and 600 mAh/g respectively in the voltage window, 0.0-0.8 V. After 100 cycles, the reversible capacity remained as high as 500 mAh/g [26]. The improved cycling performance is attributed to the nano-crystalline active material with the restriction of Sn metal particle aggregation by limiting the voltage cut-off to 0.8 V. Attempts to tailor the morphology involve the synthesis of compounds as crystalline or amorphous thin films of the desired material. Techniques adopted for growing thin films are: electrostatic spray deposition, spray pyrolysis, electron beam evaporation and low-pressure chemical vapour deposition [27]. Another method reported by Li and Martin [28] to tailor the microstructure is template synthesis that resulted in SnO_2 nano-fibers protruding from the Al-current collector surface like bristles of a brush. With the above electrode, extremely high capacity values (>700 mAh/g in the voltage range 0.0 - 0.9 V), extraordinary rate capabilities and excellent cyclability ($\sim 100\%$ coulombic efficiency for ~ 1400 cycles) have been claimed. Kim et al. [29] have reported that AlPO_4 nanoparticle coating on SnO_2 particles to be beneficial in suppressing the capacity

fading. In contrast to bare (uncoated) SnO₂ particles that retained only 8% of the initial capacity after 15 cycles, the AlPO₄ coated SnO₂ retained 44% of the initial value after 15 cycles. Analogous to the approach followed in studies on intermetallics, metal oxide carbon composites were also tested as anodes for LIB. Studies on tin oxide-carbon composites include SnO₂ carbon, synthetic graphite -SnO composite [30], SnO₂ graphite nanocomposite [31], Sn-TiO₂, SnO₂/SiO₂ mesoporous composites, and nanosized tin-zinc composite oxide. It has been theoretically envisaged and subsequently established experimentally that due to the ductility and the electric conductivity imparted by the graphite matrix, the SnO graphite composite possesses greater cyclability as compared to the bare SnO. Lee et al. [30] have suggested that synergistic interactions are present between tin oxide and carbon. This leads to higher specific capacities of SnO graphite than the theoretically predicted values based on the algebraic sum of the contributions from graphite and tin-oxide. Wang and Lee [31] described the preparation and electrochemical response of polyvinyl pyrrolidone (PVP) protected SnO₂ nanoparticles dispersed in graphite. 14.5 wt.% SnO₂ graphite composite showed initial capacity of ~ 460 mAh/g, retaining 90% of this value after 30 cycles.

Synthesis of Tin Oxide nanopowder

Nano crystalline materials or nano materials may be easily synthesized in laboratory by wet chemical methods. To prepare desired nano crystalline structures, several chemical techniques have been developed and reported in the literature, namely co-precipitation, sol-gel, spray pyrolysis, hydrothermal routes and freeze drying etc [32]. Acarbas et al. [33] reported that the tin oxide for gas sensors

has been synthesized by various methods, such as direct strike precipitation, 2-step solid state synthesis [34], microemulsion [35], sol-gel [36], spray pyrolysis [37], gel combustion technique [38] and hydrothermal synthesis [39]. Controlled precipitation is best accomplished via homogeneous precipitation, which utilizes chemical reactions such as urea decomposition, whose kinetic rate limits the release of supersaturating species [40]. The homogeneous precipitation method uses urea as a reagent to control the pH and to obtain a pure and dense hydrous tin oxide [41]. When urea is gently heated to about 85 oC, it decomposes slowly during the release of the ammonia and carbonate ions into the solution. This uniform rise in pH results in the nucleation and growth of uniformly sized and shaped particles. The hydrothermal method is an alternative to calcination for the crystallization of SnO₂ at mild temperatures. In hydrothermal synthesis, water is used as a catalyst and as a component of solid phases at elevated temperatures and pressures [42]. The use of an expensive autoclave is a disadvantage of hydrothermal synthesis. Nanosized SnO₂ has been prepared with a variety of methods by using NH₄ OH at room temperature and the hydrothermal method [43,44], the water-in-oil microemulsion-assisted method, and the 2-step templating method. The rod-like structure [44] and wormhole-like phases of SnO₂ have been reported when using a counterion source of NaOH and NH₄ OH, respectively.

Experimental

Synthesis of Tin Oxide nanopowder

In this work, a simple wet chemical method [45-47] using a controlled precipitation process was used for the synthesis of nano tin oxide powders. In this process, 0.1 mol/l aqueous solution of SnCl₄ prepared by dissolving

stannous Chloride (Spectrochem make) in concentrated HCl. The precipitation was carried out with ammonia solution by its addition using a burette. Surfactant, viz., tri-sodium citrate was used in the experiments. The effect of pH was studied by varying the precipitation pH from 4 to 10 under constant speed continuous stirring. The grey colored gel obtained in the process was allowed to age at room temperature for 16 hours, centrifuged and then filtered using watt-man filter paper. The filtrate was washed until Cl^{-1} ion was not detected by AgNO_3 test. The wet hydroxide was dried in an oven at 80°C to constant weight. After wards, it was calcined at various temperatures for three-hour durations to obtain tin oxide nano powders. Calcination temperatures and durations reported in literature [47] were made use of in designing the experiments to convert tin hydroxide to oxide.

Characterization Techniques

Phase purity of the nano materials produced was determined by XRD analysis by using a Schimadzu make, model-7000 maxima XRD. Crystallite size of the powders was determined by Full Width at Half Maximum (FWHM) method from the XRD data. FESEM (Make: Hitachi Model: S-4800) and TEM (Make: PHILIPS, Model: CM200) analyses were carried out to determine the particle size and morphology. Electrochemical cells were fabricated using various nanopowders produced as anode material. The nanopowders were blended with 10% each of PVDF binder and calcined petroleum coke (CPC) respectively in 1-methyl 2-pyrrolidone medium and coated on cu-foil. After drying and pretreatment, the cells assembled with 1M LiPF_6 in ethylene carbonate (EC) and diethyl carbonate (DEC) in 1:1 ratio by volume as electrolyte. Polypropylene microporous membrane was

used as the separator and Li metal foil as cathode and reference electrode. The assembly was carried out in an inert atmosphere glove box. The cells thus assembled were suitably aged and electrochemical characterization was conducted using a battery test station supplied by Arbin Instruments, USA, Model: BT2000.

Results and Discussion:

The objective was to prepare SnO_2 nanopowders by a simplest method and to determine the process parameters for the bulk synthesis of these powders at 50 gram level. The other objective was to test these materials for their charge storage capacity. In the controlled precipitation experiments, pH was varied from 4 to 10 and calcinations temperatures from 400 to 700°C . It was found that calcinations temperatures below 500°C did not bring about complete conversion of hydroxide to oxides. Ten experiments each were conducted at pH values from 4 to 10 in intervals of $\text{pH}=1$ to ascertain the repeatability of the experiments. The effect of calcination temperatures was tested at 500 and 650°C .

X-ray diffraction analysis of Tin Oxide Nanopowders

X-ray diffraction patterns generated during the course of work were used for testing the samples of SnO_2 for the phase purity. It was confirmed that the process employed consistently produced phase pure tin dioxide. Typical XRD pattern generated for the samples produced is depicted in the fig. 1 All diffraction peaks can be indexed to tetragonal unit cell with lattice constant $a=4.737$ nm and $c=3.185$ nm. Six broadened diffraction peaks with d spacing of 3.35, 2.641, 2.376, 1.765, 1.674 and 1.436 nm were indexed as (110), (101), (200), (211), (220) and (112) respectively as per the powder XRD standard, JCPDS 72-1147.

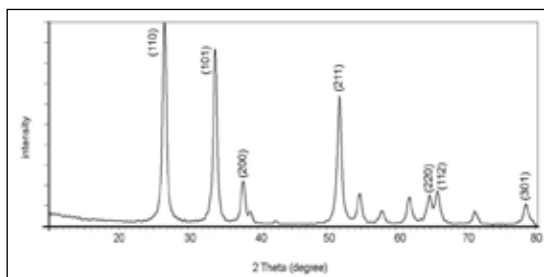


Fig. 1 X-ray Diffraction Patterns of SnO₂ prepared by controlled precipitation at pH = 6, calcined at 650 °C

Effect of precipitation pH and calcinations temperature on crystallite size

The crystallite sizes calculated using the FWHM method and plotted as a function of pH of precipitation is plotted in fig. 2. It was found that, the increase in the precipitation pH increased the particle size proportionately. The crystallite size varied from 5 to 19 nm as determined by the XRD analysis.

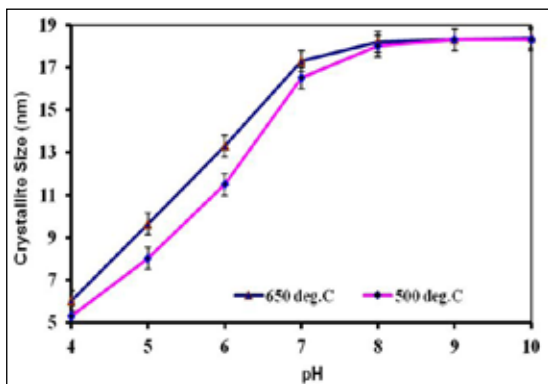


Fig. 2 Effect of precipitation and calcination temperature on the crystallite size determined by FWHM method.

Calcination temperature had a significant effect on the crystallite size as can be seen from fig.2. The effect was pronounced up to pH=7, in which, increase in calcination temperature from 500 to 650°C resulted in a maximum increase in crystallite size up to

20%. However, at pH above 8, the effect of calcination temperature was insignificant to pH=10.

FESEM analysis of Tin Oxide Nanopowders

The objective of the study was to ascertain the nano nature of particles produced in terms of particle size and also to study the morphology and agglomeration nature of the materials produced. A typical FESEM picture shown in fig. 3 which was captured on SnO₂ powders produced in batches of approximately 50 g by controlled precipitation at pH=8. Particles size was determined by image analysis and it was found that the particle size of SnO₂ powder produced ranged in sizes from 20 nm to 50 nm. The powders were generally in agglomerated form which is expected due to large number of electrons available at the surfaces of particles due to their nano nature and are attracted to each other due to the presence of equally large electron deficiency caused by electron migration.

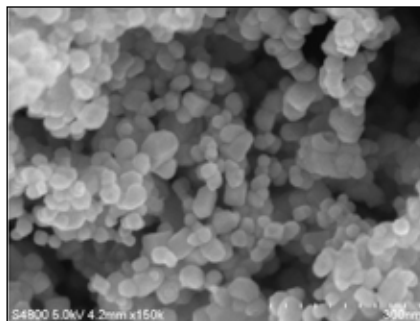


Fig. 3 FESEM Studies on Tin Oxide at 150K magnification

TEM analysis of Tin Oxide Nanopowders

Transmission Electron microscopy was used for corroborating the results of the FESEM analysis. The tin oxide powders studied were found to have spherical to angular well defined particle boundaries as depicted in Fig. 4.

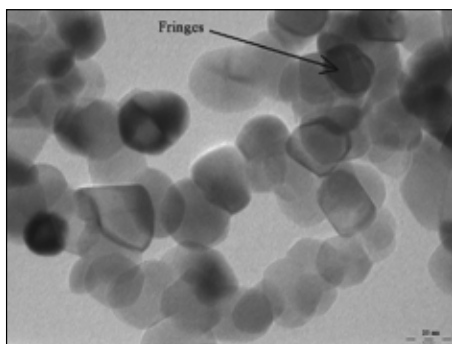


Fig. 4 TEM Studies on Tin Oxide depicting finer details of particle morphology

Electrochemical measurements of Tin Oxide Nanopowders

Potential versus capacity curves were determined at a current density of 100 mA/g of the functional material used and plotted from the electrochemical data is shown in Fig. 5. It was found that, nano SnO₂ exhibits first cycle specific capacity of 610 mAh/g in its first cycle charge. Francesca Di Lupo [48] have reported a specific capacity in the order of 500 mAh/g at C/10 current rate for SnO₂ powders. The values obtained in our work are thus comparable with the published literature (Theo. Value: 782 mAh/g). However, it is found that, it has a poor charge discharge characteristics with poorly defined constant potential plateau. This could be due to poor reach of electrolyte to the anode active nanopowders in the electrode.

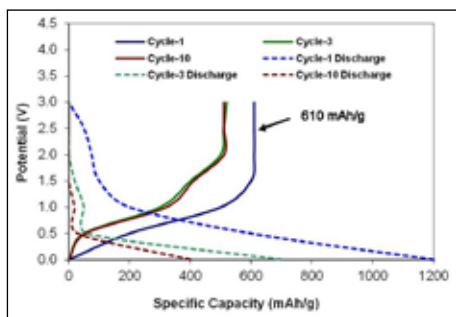


Fig. 5 Specific Capacity of nano tin Oxide Powders

Consistent charge characteristics were observed after an initial decay at cycle-1 seen between cycle-3 through cycle-10 indicates that, there is low degree of material decay with increase in number of cycles and may yield good cycle life in actual battery working conditions. Li⁺ ions have an ionic radius of 0.076 nm. The crystal structure and the void sizes in SnO₂ make Li⁺ ion make for higher storage capacity. The diffusion distances involved in charge discharge cycles is conducive for and explains the higher capacity, rate and cycling capacity of nano sized SnO₂. Apart from this high surface to volume ratio of nano powders contribute to uniform expansion, distribution and accommodation of physical expansion associated with intercalation during charge storage.

Conclusions

Process parameters have been optimized for the chemical synthesis of bulk quantities of nano sized oxide particles of Tin (SnO₂). The crystallite size as determined by XRD was in the range 5-19 nm. The corresponding particle sizes determined by SEM were in the range 20-50 nm. Nano SnO₂ exhibits specific capacity of 610 mAh/g (Theo. Value: 782 mAh/g) with poor charge discharge characteristics which needs further study.

References

1. W. A. van Schalkwijk, B. Scrosati (Eds.), "Advances in lithium-ion batteries", *Kluwer Acad./Plenum*, NY (2002).
2. G. A. Nazri, G. Pistoia (Eds.), "Lithium batteries-science and technology", *Kluwer Acad.*, NY (2003).
3. M. Broussely, G. Archdale, "Li-ion batteries and portable power source prospects for the next 5-10 years", *J. Power Sources*, 136, 386-394, (2004).

4. M. Winter, J. O. Besenhard, M. E. Spahr, P. Novak, "Insertion electrode materials for rechargeable lithium batteries", *Adv. Mater.*, 10, 725-763, (1998).
5. M. Lazzari, B. Scrosati, "A Cyclable Lithium Organic Electrolyte Cell Based on Two Intercalation Electrodes", *J. Electrochem. Soc.*, 127, 773-774, (1980).
6. B. Di Pietro, M. Patriarca, B. Scrosati, "On the use of rocking chair configurations for cyclable lithium organic electrolyte batteries", *J. Power Sources*, 8, 289-299, (1982).
7. J.M. Tarascon, M. Armand, "Issues and challenges facing rechargeable lithium batteries", *Nature*, 414, 359-367, (2001).
8. S. Megahed, B. Scrosati, "Lithium-ion rechargeable batteries", *J. Power Sources*, 51, 79-104, (1994).
9. J. L. Tirado, "Inorganic materials for the negative electrode of lithium-ion batteries: state-of-the-art and future prospects", *Mater. Sci. & Engg.*, R40, 103-136, (2003).
10. B. Scrosati, "Lithium Rocking Chair Batteries - An Old Concept", *J. Electrochem. Soc.*, 139, 2776-2781, (1992).
11. B. Scrosati, "Recent advances in lithium ion battery materials", *Electrochim. Acta*, 45, 2461-2466, (2000).
12. M. Wachtler, M. Winter, J. O. Besenhard, "Anodic materials for rechargeable Li-batteries", *J. Power Sources*, 105, 151-160, (2002).
13. O. Crosnier, X. Devaux, T. Brousse, P. Fragnaud, D. M. Schleich, "Influence of particle size and matrix in "metal" anodes for Li-ion cells", *J. Power Sources*, 97-98, 188-190, (2001).
14. O. Mao, J. R. Dahn, "Mechanically Alloyed Sn-Fe(-C) Powders as anode materials for Li-ion batteries 3Sn₂Fe SnFe₃ C active Inactive Composites", *J. Electrochem. Soc.*, 146, 423-427, (1999).
15. J. Yang, M. Wachtler, M. Winter, J. O. Besenhard, "Sub-Microcrystalline Sn and Sn-SnSb Powders as Lithium Storage Materials for Lithium-Ion Batteries", *Electrochem. Solid State Lett.*, 2, 161-163, (1999).
16. S.-J. Lee, H. Y. Lee, S. H. Jeong, H.-K. Baik, S.-M. Lee, "Performance of tin-containing thin-film anodes for rechargeable thin-film batteries", *J. Power Sources*, 111, 345-349, (2002).
17. J. S. Gnanaraj, R. W. Thompson, S. N. Iaconatti, J. F. DiCarlo, K. M. Abraham, "Formation and Growth of Surface Films on Graphitic Anode Materials for Li-Ion Batteries", *Electrochem. and Solid State Lett.*, 8, A128-A132, (2005).
18. W. X. Chen, J. Y. Lee, Z. Liu, "Electrochemical lithiation and de-lithiation of carbon nanotube-Sn₂Sb nanocomposites", *Electrochem. Commun.*, 4, 260-265, (2002).
19. L. Shi, H. Li, Z. Wang, X. Huang, L. Chen, "Nano-SnSb alloy deposited on MCMB as an anode material for lithium ion batteries", *J. Mater. Chem.*, 11, 1502-1505, (2001).
20. Y. Idota, T. Kubota, A. Matsufoji, Y. Maekawa, T. Miyasaka, "Tin-based amorphous oxide a high-capacity lithium-ion-storage material", *Science*, 276, 1395-1397, (1997).
21. J. Chouvin, C. P. Vicente, J. O. Fourcade, J. C. Jumas, B. Simon, P. Biensan, "Deeper insight on the lithium reaction mechanism with amorphous tin composite oxides", *Solid State Sci.*, 6, 39-46, (2004).
22. R Demir-Cakan, Young-Sheng H, Markus A, J Maier, Maria-Magdalena T, "Facile one-pot synthesis of mesoporous SnO₂ microspheres via nanoparticles assembly and lithium storage properties", *Chem. Mater.*, 20, 1227-1229, (2008).
23. I. A. Courtney, J.R.Dahn, "Electrochemical and In Situ X-Ray Diffraction Studies of the Reaction of Lithium with Tin Oxide Composites", *J. Electrochem. Soc.*, 144, 2045-2052, (1997).
24. I. A. Courtney, W.R.McKinnon, J.R.Dahn, "On the Aggregation of Tin in SnO Composite Glasses Caused by the Reversible Reaction with Lithium", *J. Electrochem. Soc.*, 146, 59-68, (1999).
25. J. S. Sakamoto, C. K. Huang, S. Surampudi, M. Smart, J. Wolfenstine, "The effects of particle size on SnO electrode performance in lithium-ion cells", *Mater.Lett.*, 33, 327-329, (1998).
26. J.-H. Kim, G.-J. Jeong, Y.W. Kim, H.J. Sohn, C. W. Park, C. K. Lee, "Tin-Based Oxides as Anode Materials for Lithium Secondary Batteries", *J. Electrochem. Soc.*, 150, A1544-A1547, (2003).

27. T. Brousse, O. Crosnier, X. Devaux, P. Fragnaud, P. Paillard, J. Santos-Pena, D.M. Schleich, "Advanced oxide and metal powders for negative electrodes in lithium-ion batteries", *Powder Technol.*, 128, 124-130, (2002).
28. N. Li, C.R. Martin, A High-Rate, High-Capacity, "Nanostructured Sn-Based Anode Prepared Using Sol-Gel Template Synthesis", *J. Electrochem. Soc.*, 148, A164-A170, (2001).
29. T.-J. Kim, D. Son, J. Cho, B. Park, H. Yang, "Enhanced electrochemical properties of SnO₂ anode by AlPO₄ coating", *Electrochim. Acta*, 49, 4405-4410, (2004).
30. J. Y. Lee, R. Zhang, Z. Liu, "Lithium intercalation and deintercalation reactions in synthetic graphite containing a high dispersion of SnO", *Electrochem. Solid State Lett.*, 3, 167-170, (2000).
31. Y. Wang, J. Y. Lee, "Preparation of SnO₂-graphite nanocomposite anodes by urea-mediated hydrolysis", *Electrochem. Commun.*, 5, 292-296, (2003).
32. Sanjay R. Dhage, S. P. Gaikwad, Violet Samuel, V. Ravi, "Synthesis of nanocrystalline SnO₂ powder at 100°C", *Bull. Mater. Sci.*, 27(3), 221-222, (2004).
33. Acarbas O, Suvaci E and Dog A., "Preparation of nanosized tin oxide (SnO₂) powder by homogeneous precipitation", *Ceramics International*, 33, 537-542, (2007).
34. Li, F.; Chen, L.; Chen, Z.; Xu, J.; Zhu, J.; Xin, X., "Two-step solid-state synthesis of tin oxide and its gas-sensing property", *Mater. Chem. Phys.*, 73, 335-338, (2002).
35. Song, K. C.; Kim, J. H. J., "Preparation of Nanosize Tin Oxide Particles from Water-in-Oil Microemulsions", *Colloid Interf. Sci.*, 212, 193-196, (1999).
36. Adnan, R, Razana, N.A., Rahman, I.A., Farrukh, M.A., "Synthesis and characterization of high surface area tin oxide nanoparticles via the sol-gel method as a catalyst for the hydrogenation of styrene", *J. Chinese Chem. Soc.*, 57(2), 222-229, (2010).
37. Lee, J. H.; Park, S. J. J., "Preparation of spherical tin oxide powders by ultrasonic spray pyrolysis", *Am. Ceram. Soc.*, 76, 777-780, (1993).
38. Bhagwat, M.; Shah, P.; Ramaswamy, "Synthesis of nanocrystalline SnO₂ powder by amorphous citrate route", *Mater. Lett.*, 57, 1604-1611, (2003).
39. Baik, N. S.; Sakai, N.; Miura, N.; Yamazoe, N., "Preparation of Stabilized Nanosized Tin Oxide Particles by Hydrothermal Treatment", *J. Am. Ceram. Soc.*, 83, 2983-2987, (2000).
40. Willard, H. H.; Tang, N. K. J., "A Study of the Precipitation of Aluminum Basic Sulfate by Urea", *Am. Chem. Soc.*, 59, 1190-1196, (1937).
41. Ozge Acarbas, Ender Suvac, Aydın Dogan, "Preparation of nanosized tin oxide (SnO₂) powder by homogeneous precipitation", *Ceramics International*, 33(4), 537-542, (2007).
42. Somiya, S.; Roy, R., "Hydrothermal synthesis of fine oxide powders", *Bull. Mater. Sci.*, 23, 453-460, (2000).
43. Wang, Y. D.; Ma, C. L.; Sun, X. D.; Li, H. D., "Preparation of nanocrystalline metal oxide powders with the surfactant-mediated method", *Inorg. Chem. Commun.*, 5, 751-755, (2002).
44. Guo, C., Cao, M., Hu, C., "A novel and low-temperature hydrothermal synthesis of SnO₂ nanorods", *Inorg. Chem. Commun.*, 7, 929-931, (2004).
45. G S Devi, H Z R Hamoon, A Nanaji, K R Reddy, B Sreedhar and J V Ramana Rao, "A Simple Sol-Gel Protocol Towards Synthesis of Semiconducting Oxide Nanomaterial", *J. Nano Electr. Phys.*, 3, 1-5, (2011).
46. S Gnanam and V Rajendran, "Luminescence properties of EG-assisted SnO₂ nanoparticles by sol-gel process", *Digest Journal of Nanomaterials and Biostructures*, 5(3), 699-704, (2010).
47. Y A O Minqi, W E I Yinghui, H U Lanqing and X U Bingshe, "Preparation and properties of nanosized SnO₂ powder", *Trans. Nonferrous Met Soc., China.*, 12(5), 833-836, (2006).
48. Francesca Di Lupo, Claudio Gerbaldi, Giuseppina Meligrana, Silvia Bodoardo, Nerino Penazzi, "Novel SnO₂ / mesoporous carbon spheres composite anode for li-ion batteries", *Int. J. Electrochem. Sci.*, 6, 3580-3593, (2011).